Cell-Fiber Interactions:
A New Route to Mechano-Biological Investigations in Developmental and Disease Biology

By
Kevin Sheets

Dissertation submitted to the faculty of the Virginia Polytechnic Institute and State University in partial fulfillment of the requirements for the degree of

Doctor of Philosophy
In
Biomedical Engineering and Sciences

Amrinder S. Nain, Chair
Bahareh Behkam
Rafael V. Davalos
Daniela Cimini
Yong W. Lee
Julie A. Phillippi

October 3, 2014
Blacksburg, Virginia

Keywords: Mechanobiology, Outside-In Force, Single Cell Force Microscopy, Aneurysm

Cell-Fiber Interactions:
A New Route to Mechano-Biological Investigations in Developmental and Disease Biology

Kevin T. Sheets

ABSTRACT

Cells in the body interact with a predominantly fibrous microenvironment and constantly adapt to changes in their neighboring physiochemical environment, which has implications in developmental and disease biology. A myriad of *in vitro* platforms including 2D flat and 3D gel substrates with and without anisotropy have demonstrated cellular alterations to subtle changes in topography. Recently, our work using suspended fibers as a new *in vitro* biological assay has revealed that cells are able to sense and respond to changes in fiber curvature and structural stiffness as evidenced by alterations to cytoskeleton arrangement, including focal adhesion cluster lengths and nucleus shape indices, leading to altered migration speeds. It is hypothesized that these behaviors occur due to modulation of cellular *inside-out* forces in response to changes in the external fibrous environment (*outside-in*). Thus, in this study, we investigate the role of fiber curvature and structural stiffness in force modulation of single cells attached to suspended fibers. Using our previously reported non-electrospinning Spinneret based Tunable Engineered Parameters (STEP) fiber manufacturing platform, we present our findings on single cell *inside-out* and *outside-in* forces using fibers of three diameters (250 nm, 400 nm and 800 nm) representing a wide range of structural stiffness (3-45 nN/μm). To investigate cellular adaptability to external perturbation, we present the development of a first-of-its-kind force measurement 'nanonet' platform capable of investigating cell adhesion forces in response to symmetric and non-symmetric (injury model) loading. Our combined findings are multi-fold: (i) Cells on suspended fibers are

able to form focal adhesion clusters approximately four times longer than those on flat substrates, which gives them potential to double their migration speeds, (ii) Nanonets as force probes show that the contractility-based *inside-out* forces are nearly equally distributed on both sides of the cell body, and that overall force magnitudes are dependent on fiber structural stiffness, and (iii) External perturbation can evenly (symmetric) or unevenly (non-symmetric) distribute forces within the cell, and the resulting bias causes diameter-dependent *outside-in* adhesion force response. Finally, we demonstrate the power of the developed force measurement platform by extending our studies to cell-cell junctional forces as well as single-cell disease models including cancer and aortic aneurysm.

Acknowledgements

As I close out my final chapter at Virginia Tech, I am struck by the sheer number of people who have played a direct role in teaching, mentoring, and guiding me through what has proven to be simultaneously the most rigorous and rewarding experience of my life. I would like to thank my advisor Dr. Nain for taking a chance on me as his first Biomedical Engineering PhD student in the STEP Lab back in 2010. Having such an integral role in the beginnings of the lab is something I will value as I look back on my time spent here. I would also like to thank Dr. Behkam, Dr. Cimini, Dr. Davalos, Dr. Lee, and Dr. Phillippi for being willing to serve as committee members and for their valuable input and availability. Having a group of mentors who are genuinely interested in my personal and professional success has made this project all the more fun to pursue. I am also grateful for SBES staff, including Tess and Pam, for gladly helping with administrative tasks and always having snacks on hand. I am also grateful for the many friendships I have formed with past and present labmates. Ji, Stephen, Colin, Puja, Sean, Tim, Amritpal, Brian, Tracee, Megan, Shikha, Ian, Carrie, Jack, and Brendon, you all made sure there was never a dull moment in the lab, no matter how late we ended up having to stay and work.

I am also incredibly thankful for family and friends who have constantly supported me throughout my time here. Mom and Dad: I can't put my gratitude for your support into words. To JD and his majestic seasonal beard: thanks for being awesome and for offering your guest room in my time of need. And finally, I absolutely could not and would not have done any of this without the constant love and support from my beautiful wife Cissy, who has reshaped my definition of what it means to be a true companion: I dedicate this and the rest of my life's work to you.

Table of Contents

List of Figures

List of Tables

List of Abbreviations

AFM	Atomic Force Microscope
ANOVA	Analysis of Variance
DAPI	4’,6-diamidino-2-phenylindole
DBTRG	Denver Brain Tumor Research Group
DI	Deionized
DMEM	Dulbecco’s Modified Eagle’s Medium
DMSO	Dimethyl Sulfoxide
ECM	Extracellular Matrix
ESEM	Environmental Scanning Electron Microscope
FBS	Fetal Bovine Serum
FESEM	Field-Emission Scanning Electron Microscope
GFP	Green Fluorescent Protein
HEPES	4-(2-hydroxyethyl)-1-piperazineethanesulfonic acid
MEM	Minimum Essential Media
MEMS	Microelectromechanical Systems
μN	micro-Newton
nN	nano-Newton
PBS	Phosphate Buffered Saline
pN	pico-Newton
PS	Polystyrene
SEM	Scanning Electron Microscope
STEP	Spinneret-based Tunable Engineered Parameters
TAA	Thoracic Aortic Aneurysm

1. OVERVIEW

1.1 Cell Mechanobiology

Research from the past several decades has demonstrated that cells are significantly affected by the physical environment that surrounds them. Cells form adhesive contacts with their fibrous extracellular matrix (ECM) and transmit forces through them that allow the cell to both investigate its surrounding structure and regulate behaviors such as adhesion and migration. The forces that are conducted through cell-ECM contacts are bi-directional, either originating from within the cell acting on the ECM ("inside-out", e.g. contractile forces generated during migration) or from outside the cell acting inward ("outside-in", e.g. adhesion forces). Capturing both modes through single-cell force measurement platforms allows one to distinguish the forces that cells apply from those that they can withstand, with implications to the study of disease states where progression from normal function to failure either occurs rapidly or with minimal warning or detection (bone fracture, muscle or ligament tears, blood vessel aneurysms). Although nanofibrous substrate topography is prevalent *in vivo*, to the best of our knowledge no fiber-based force measurement platform for measuring both inside-out and outside-in forces currently exists.

1.2 Project Aims

Nanofibers such as those found in ECM are known to elicit changes in cell adhesion, migration, cytoskeletal arrangement, and other phenomena such as reversible blebbing in cancer cells due to their unique topography and mechanics. Despite cell force measurement becoming a growing area of interest in the mechanobiology field, fiber-based ECM mimicking platforms for measuring single and multi-cell bidirectional forces do not currently exist. This is due in part to

the difficulty in arranging fibers with the degree of spatial control necessary for capturing cell forces. However, the Spinneret-based Tunable Engineered Parameters (STEP) technique offers improvements in spatial fiber deposition over traditional manufacturing platforms, thus enabling the design of nanofiber-based force measurement scaffolds. By spatially arranging suspended fibers in a grid-like 'nanonet' composed of deflectable fiber segments, *inside-out* cell forces such as those exerted during migration can be passively measured. Furthermore, by interfacing a robotically-manipulated probe-based perturbation system with the nanonet scaffolds, cell response to *outside-in* forces can also be measured.

The overarching goal of this work is to use STEP fiber manufacturing technology to develop and implement a nanofiber-based force measurement platform capable of characterizing forces at single-cell resolution. We will then use the newly-developed system to test the hypothesis that single aortic smooth muscle cell mechanics diminish as a result of aneurysmal disease states. This project will be conducted by investigating the following specific aims:

Specific Aim 1: Determine the role of STEP scaffold parameters on suspended cell-fiber interactions, including migration speed, focal adhesion behavior, and cytoskeletal organization/shape configuration.

Specific Aim 2: Integrate current STEP technology with an outside-in force platform capable of perturbing single and multi-cells in multiple modalities.

Specific Aim 3: Employing the outside-in platform, investigate single-cell biophysics of both normal and aneurysmal aortic smooth muscle cells.

1.3 Document Organization

This document details studies of single cell behavior on nanofibers fabricated using the STEP technique. Chapter 2 provides an introduction to cell-ECM interactions and the importance of measuring forces on fiber substrates. Chapter 3 details fundamental studies performed on single cell-fiber interactions. Chapter 4 highlights the development of the outside-in probe perturbation system, including demonstration of capabilities at single and two-cell resolution. Chapter 5 applies the system's capabilities towards understanding single cell disease models including aortic aneurysm and cancer cell blebbing. Chapter 6 concludes the dissertation, with Appendices that include mathematical derivations and Matlab codes following.

1.4 Attribution

Chapter 3: Elucidating Cell-Fiber Interactions

- Stephen Wunsch, BS (Biology): Stephen was a co-author of this material who contributed to data collection as an undergraduate researcher.
- Colin Ng, MS (Mechanical Engineering): Colin was a co-author of this material who contributed to data collection as an undergraduate researcher.
- Ji Wang, MS (Engineering Science & Mechanics): Ji is currently a PhD candidate in Biomedical Engineering & Mechanics at Virginia Tech. Ji was a co-author of this material who contributed to the development of the polystyrene spinning design space, modeling nanofiber mechanics with AFM/ESEM approaches, and customizing the beam equations used in later force measurement models.

Chapter 4: Development of the Outside-In Probe System

- Brendon Griffin (Mechanical Engineering): Brendon is currently an undergraduate student in Mechanical Engineering at Virginia Tech. He contributed to the development of the dual probe system.
- Tim O'Brien, BS (Mechanical Engineering): Tim is currently pursuing his PhD in Mechanical Engineering at Virginia Tech. Tim contributed to the Matlab code development for inverse force modeling.
- Sean Meehan, MS (Mechanical Engineering): Sean graduated from the STEP lab in 2013 and contributed to the work by initializing procurement and setup of the Sutter equipment used for the probe system.

Chapter 5: System Applications

- Puja Sharma, BS (Biology): Puja is currently a PhD candidate in Biomedical Engineering at Virginia Tech. She was a co-author of this material and contributed to experiments with blebbing DBTRG-05MG cells.
- Ah-Ram Kim, BS (Mechanical Engineering): Ah-Ram is currently pursuing her MS in Mechanical Engineering at Virginia Tech with Dr. Bahareh Behkam. She was a co-author of this material and contributed to cyclic and drug testing experiments and analysis.
- Jackson Cooper (Materials Science & Engineering): Jack is currently an undergraduate student at Virginia Tech. He contributed to the pilot study investigating aneurysmal cell mechanics.

- Brian Koons, BS (Mechanical Engineering): Brian is currently pursuing his PhD in Mechanical Engineering at Virginia Tech. Brian is a co-author who contributed helpful discussion.
- Amritpal Gill, BS (Mechanical Engineering): Amritpal is currently pursuing his MS in Mechanical Engineering at Virginia Tech. He is a co-author who contributed to the initial drug studies using the probe system.

2. INTRODUCTION

2.1 Cell-ECM Interactions and Forces

Canonical *in vitro* studies in cell mechanobiology have often been performed on flat substrates[1–3]. Seeding cells on glass coverslips or gels of tunable modulus have led to many critical and clinically-relevant discoveries of cell-substrate interactions. However, the substrates from these studies have limited discernible topographical relation to *in vivo* architecture. With advancements in the ability to manufacture circular cross-sectional, high aspect-ratio fibers on the micro/nanoscale, cellular investigations have revealed that key cell behaviors are significantly different on fiber structures[4,5]. Suspended fibers provide curvature constraints and gradients of structural stiffness that do not exist on flat surfaces. By probing their microenvironment with cytoskeletal protrusions, cells interacting with fibers are able to sense spacing and orientation between fibers as well as the hierarchical assembly of fibers in multiple layers. Compared to flat substrates, where the bulk modulus (N/m^2) plays a dominant role in cell behavior[6–14], suspended fibers with structural stiffness (N/m) gradients directly affect cell shape, focal adhesion arrangement and migration[15,16]. Suspended fiber networks are thus thought to elicit different cellular force responses due to focal adhesion clustering and curvature-induced wrapping.

In the body, cells receive physical and chemical cues from their surrounding microenvironment known as the extracellular matrix (ECM), a primarily fibrous network whose composition varies temporally and spatially in the body. The ECM is composed of protein fibrils ranging 30-70 nm in diameter that can bundle into 200 nm – 1 μm fibers[17]. Main constituents include collagen, elastin, fibronectin, laminin, and proteoglycans, but the exact composition and alignment varies among tissue microenvironments[18–20]. This network of micro/nanofibers serves as a scaffold that provides cells with mechanical and chemical cues which, along with external

stimuli, dictate individual cell behavior. The combination of these influences can cause significant changes in cell shape, spreading, migration, and differentiation, yet it remains unclear how biophysical cues alone affect ultimate cell function[21,22]. For this reason, *in vitro* culture conditions mimicking ECM and replete with native mechanics/topography have tremendous potential for studying single cell behavior for applications in tissue engineering-based therapies[23–25].

A cell receives physical cues from ECM through a phenomenon known as mechanotransduction – the conversion of a physical signal to a chemical alteration in the cell[26–28]. Understanding the factors and forces that affect mechanotransduction enables manipulation of individual and population-level cell behaviors to address clinical issues, such as speeding the wound healing process, causing apoptosis in cancer cells, or forcing stem cells to differentiate into specific lineages[29–34]. Cells can apply forces acting on their environment to investigate passive substrate mechanics and dynamics (inside-out) or respond to forces actively acting on them from an outside source, eliciting reactionary cellular response (outside-in)[35–37]. Both are physiologically relevant, as seen in the example case of bone tissue: osteoblasts generate inside-out forces to navigate through pores to deposit new mineral where needed, but outside-in forces from tissue loading (walking/running, or conversely bed rest/microgravity) determine new mineral location in a phenomenon described by Wolff's Law[38,39]. In a similar manner, rhythmic pulsatile blood flow and cyclic vessel dilations cause outside-in remodeling of F-actin in endothelial cells[40,41]. Capturing both inside-out and outside-in forces with single-cell force measurement platforms allows one to separate the forces that cells apply from those that they can withstand. This is relevant to the study of disease states where progression from normal function to failure either occurs rapidly or with minimal warning or detection, as in the case of aortic aneurysms.

2.2 Fibrous Scaffold Fabrication Methods

Key factors impacting fiber use in cell studies include the ability to precisely control fiber diameter and deposition (both orientation and spacing) in both single and multiple layers. Advancements in manufacturing processes have enabled creation of smaller diameter fibers with higher degrees of alignment, thus making fiber manufacturing a powerful tool for investigating cell-substrate interactions (**Table 1**). In this regard, electrospinning is perhaps the most widely known and thoroughly studied method of forming polymeric nanofibers. In this process, polymer solution is pumped through a syringe to a needle where an electrical charge extrudes polymer fibers onto a collecting target[42–46]. The principle underlying this process was first discovered in the 1890's by Rayleigh but was not patented until 1934 by Formhals[47–49]. Taylor's research on electrically-driven jets conducted in the late 1960's paved the way for modern refinements that allow electrospinning to generate micro/nanoscale fibers today[50]. With the realization that electrospinning could produce fibers with diameters on the order of those in native tissue, the bioengineering community has seen rapid growth in the use and improvement of the electrospinning technique to achieve higher degree of alignment and spatial organization[51,52].

Some of the more recent advancements in nanofiber fabrication include far-field electrospinning (FFES), near-field electrospinning (NFES) and non-electrospinning direct drawing methods. FFES is widely used to fabricate continuous fibers of various materials (including engineering plastics, biopolymers and ceramics)[53–57]. To create substrates with aligned fibers, a high speed rotating drum is commonly used as a collector in place of a stationary target[58]. Rotary jet spinning makes use of a rotating spinneret instead of a rotating target[59]. Aligned polymer/ceramic nanofibers can also be achieved using patterned electrodes[60] or a wheel-like bobbin collector[61,62]. Modifications to the electric source include using biased AC potentials, or

using an auxiliary counter electrode[63,64]. In these approaches, due to the inherent electric instabilities of the electrospinning process, a high degree of parallelism is difficult to achieve and the spacing between fibers is difficult to control in multiple layers. On the other hand, NFES has demonstrated improved fiber patterning through reduction of applied voltage and the source-to-target distance[59,65]. Since decreasing voltage enhances deposition capabilities, several approaches have removed the electric component entirely. For instance, airbrushed nanofibers eject polymer with compressed air instead of electric propulsion[66]. Direct drawing uses polymer wetted probe tips for precise fiber deposition[67,68]. Although some well-positioned fiber patterns have been demonstrated, this technique cannot operate continuously.

Table 2-1. Comparison of fiber manufacturing techniques and their biological applications, reproduced with permission[110].

Method	Diameter Range	Uniqueness and Applications	Disadvantages	Ref.
Electrospinning (FFES & NFES)	80-1000 nm	Mass production; wide range of polymers, tissue engineering	Comparably low fiber alignment & hierarchical control	43,44,51,69
Airbrushed	125-1950 nm	Target geometry variety, ease of use and low cost; tissue engineering	Comparably low fiber alignment & hierarchical control	66
Rotary Jet Spinning	425-1600 nm	Mass production of aligned fibers; tissue engineering	Comparably low fiber alignment & hierarchical control	59
STEP Technique	70-5000 nm	Diameter, orientation and spatial deposition control; single cell-fiber interactions, tissue engineering	Mass production	68,70–72

Suspended fibers which form a bridge across a gap can be created by either hollowing out or forming trenches in the target substrate[46,73]. While less widely-used, suspended air-gap nanofibers have been made with non-spinning techniques using micropillar arrays by brushing fibrinogen across thrombin-coated pillars or melting polystyrene films over them[74,75]. Micropipette

probes have also been used to directly draw fibers from solution droplets[67,76], or push and pull droplets across unique geometries[77].

STEP is a pseudo-dry spinning nanofiber fabrication technique which does not rely on an electric field to stretch the solution filament. This method is fundamentally different from electrospinning in that the absence of an electric field eliminates random fiber deposition associated with a charged Taylor cone and distant target, allowing arrays of highly aligned fibers to be created. The STEP fiber manufacturing platform has demonstrated the ability to deposit suspended fibers of a variety of polymers with control on fiber dimensions (diameter: sub-50 nm to microns, length: ~ cm's), and orientation (≤ 2.5°, sub-micron fiber-spacing deposition resolution in single and multiple layers) (**Figure 2-1**).

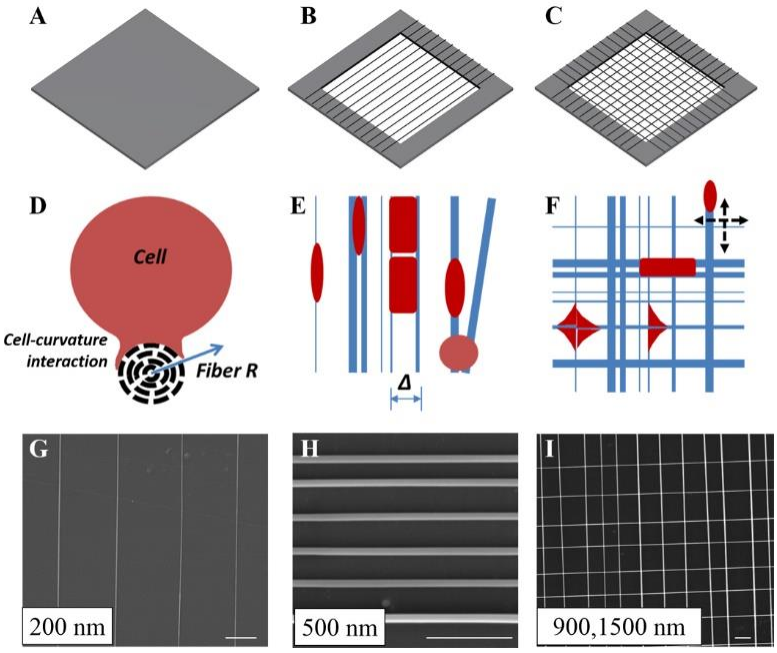

Figure 2-1. (A-C) Substrate designs used in STEP manufacturing include flat PS, suspended single layered fibers (SS) and suspended double layered, intersecting fibers (SD). (D) Cross-section view of a typical cell interacting with a suspended fiber. Of particular interest is how a cell's migration dynamics change when attached to fibrous substrates of varying sub-cellular radii (shown underneath the cell cartoon). (E) Typical cell shapes (red) when attached to SS fibers (blue). (F) Typical cell shapes when attached to SD fibers. (G-H) STEP capabilities demonstrating control of fiber diameter and spacing, and (I) deposition in multiple layers with ordered spacing and alignment. Scale bar 5 μm. Reproduced with permission[5].

The STEP technique is advantageous in cell studies as well because it can be used to position cells in repeatable configurations on the precisely deposited fibers. However, in order to accomplish this, scaffold throughput is necessarily diminished compared to electrospinning technologies. Scaffold geometrical parameters such as fiber diameter, spacing, and orientation can be varied to present cells with suspended fiber topographies which restrict focal adhesion complex (FAC) formation to the fiber axes. As cells attach to the fibers and take on these repeatable shapes, changes in migration speed can be observed and linked to FAC development.

2.3 Importance of Fiber Topography and Mechanics on Cell Behaviors

Fibers possessing diameters closely resembling those of the assembled fibrous ECM proteins provide a curved surface for cell attachment and have mechanistic properties that can be tuned to investigate biophysical influence on cell behaviors. The suspended nanofibers cause cells to react to surface curvature and dimensionality that flat substrates inherently mask, thus providing a unique platform for investigating cell-fiber interactions. Cells on fibers sense and respond to changes in curvature (or diameter), form spindle or parallel shapes due to differences in fiber spacing, spread and attach differently on oriented fibers, and finally form kite-like polygonal shapes on hierarchical assemblies (**Figure 2-2**).

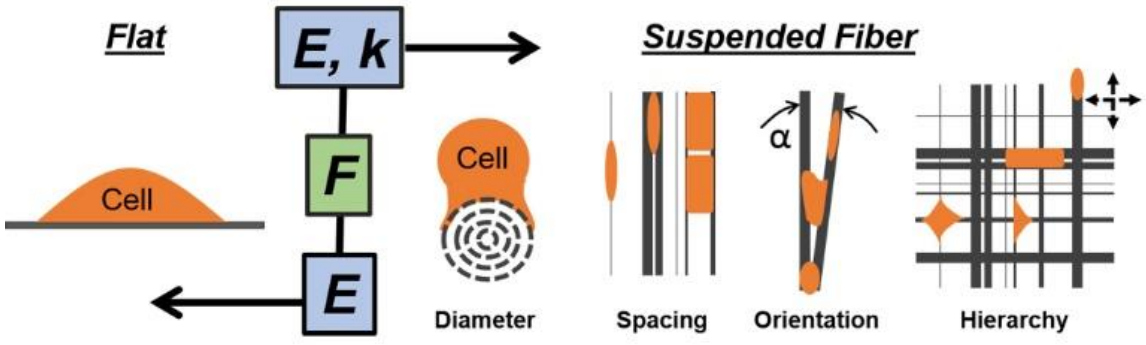

Figure 2-2. Suspended fiber design space, which accounts for the substrate's elastic modulus (E) as well as structural stiffness (k), compared to the traditionally-studied flat substrates. Reproduced with permission[110].

We speculate that these parameters, combined with material and structural stiffness in suspended fiber configurations, lead to differences in force generation (F) compared to flat substrates, which elicits diverse behavior as measured by a large number of metrics including cytoskeletal arrangement, nuclear shape index, FAC cluster length and distribution, migration speed, proliferation, and differentiation. Due to these differences, it is of interest to develop a fiber-based force measurement platform which can account for ECM-like topographical interactions.

2.4 Current Methods of Characterizing Cell Forces

2.4.1 Inside-Out Platforms

The prevailing approach for measuring inside-out forces involves the use of substrates that contain deformable objects which deflect when loaded. As long as the degree of bending or deflection can be reliably measured, forces can be calculated by making appropriate assumptions about the strength and shape of the material being deflected. This approach has taken on different forms in recent years, including traction force gels (embedded particle tracking), micropillar arrays, and other microelectromechanical systems (MEMS)[78–83].

The earliest example of an inside-out force measurement technique is the traction force gel which was demonstrated in 1980 by Harris et al[1]. The underlying concept of this approach relied upon the wrinkling of thin silicone rubber sheets, caused by the forces exerted by cultured cells during migration. Resolution has since been improved by embedding fluorescently-traceable microparticles into the gels which are displaced when the cell deforms the substrate surface[84]. An advantage of traction force gels is that a single cell can interact with tens to hundreds of microparticles, meaning the magnitudes and vectors of forces that cells apply can be mapped to localized regions of the cell[80]. Inside-out forces have been reported to be on the order of 100 nano-

Newton (nN) with this technique, although calculations require complex modeling that can be quite time consuming, limiting its effectiveness for multi-cell applications[85]. Outside-in perturbations have been applied to these gels *via* external stretch[86].

Since its introduction to the field made possible by soft lithography techniques, micropillar arrays have become a widely-used method of measuring cell contraction forces[87,88]. Cells seeded on these substrates form adhesions at the tops of multiple pillars and deflect them inwards as they pull on them to generate migration/contraction forces. Cardiac myocytes which twitch and relax have been reported to exert between 140 – 400 nN with this method[89]. Pillar height and diameter can be adjusted to alter the bending stiffness of each post. This technique demonstrated that cells modulate their forces by exerting increased contraction on pillars of higher stiffness, reporting forces up to 800 nN on the stiffest pillars tested[90]. The micropillar array system offers several advantages. Force vectors are easily observed based on the direction of deflection. The cell spread area and surface area of adhesion can also be controlled by adjusting either the pillar surface area, density, and/or spacing. Systematic adjustments have been made to these parameters to evaluate the relative contributions of stiffness, cell spread area, and ligand density on cell forces[90]. Micropillar arrays are typically used as passive inside-out measurement systems, but the underlying film can also be stretched to create outside-in perturbations[91]. Biologically, micropillar arrays have helped confirm the significance of structural stiffness and the relative unimportance of cell spread area on cell force modulation. Unfortunately, these structures lack topographical semblance to *in vivo* topography. Furthermore, force calculations are complicated by cell adherence down the length of the pillar (forces are not necessarily restricted to the x-y plane).

MEMS device designs vary immensely, but some strategies utilize the same deflection-based principle for measuring cell forces. For instance, Ferrell et al. have shown a device which

consists of four oppositely-oriented cantilever-based adhesion pads which met in the center of a ring[92]. Cells adhered to the center of the ring apply forces to and deflect any one of the four cantilevers. Peak forces were reported in the 600 nN range with this method. MEMS can also be used to actuate passive structures to provide outside-in perturbations as well[93].

2.4.2 Outside-In Platforms

Outside-in forces (the cell's ability to withstand external loads) can be measured either by using passive substrates which interact with an active component (traction force gels or micropillar arrays whose underlying film is stretched) or by actively manipulating the cell with AFM cantilevers, fluid shear, optical traps, magnetic cytometry, or MEMS devices[88,94–97]. One of the most widely-used outside-in force measurement systems, perhaps due to its versatility, is the atomic force microscope (AFM)[98]. The AFM consists of a cantilever which bends in response to applied forces. Using a protein-coated AFM tip, this instrument can form a stronger 'engineered' adhesion to the cell than the cell naturally has with the substrate, so that as the tip is drawn away, the cell is pulled from the substrate while remaining bound to the cantilever. As the cell resists this motion, the resulting beam deflection is tracked with a laser and photodiode. Thus, the AFM can provide real-time measurements of the forces required to detach the cell either from a substrate or from another cell. After lifting a cell off the substrate, it can be reattached to a second cell or a population of cells so that cell-cell adhesion forces can be measured[99]. Keeping in mind that maximum cell adhesion strength is known to be conditional on cell type, ligand presence, strain rates, time allotted for adhesion maturation, as well as other parameters, cells have displayed a maximum adhesion force from about 100 – 600 nN using AFM-based methods[100]. Advantages of the AFM include force resolution and real-time monitoring throughout the pull, but it is a

predominately single-cell based technique and is not considered high-throughput. Additionally, inside-out forces cannot be measured using AFM alone.

Fluid shear approaches have also been used to peel cells off of their substrate. Garcia et al. developed a disk submerged in fluid which, when rotated, caused cells to detach due to fluid shear forces[101]. Cells that were closer to the center of the disk experienced less force than those toward the edges. This technique allows a multitude of cells to be tested simultaneously, and it was found that 50% of the rat osteosarcoma cells would detach from the disk after reaching 5 $nN/\mu m^2$ shear stress. To test single cells, microfluidics offer scale-down advantages that simplify force calculations and ensure higher resolution. Interestingly, tests with microfluidics report adhesion strengths at about 0.1– 0.3 $nN/\mu m^2$, significantly smaller than those achieved with the spinning disk[96,102].

Smaller yet are forces that can be applied *via* optical traps/tweezers and magnetic cytometry which have pico-Newton (pN) resolution. Optical traps apply beams of focused light from oppositely-oriented directions to contain microscopic objects within them. Two traps can be used to each hold a microscopic bead which in turn are attached to opposite ends of the cell. As one bead is pulled away from the other, the cell resists deformation, and the force applied to the bead can be measured[103]. The high resolution offered by optical traps comes at the cost of limited force magnitudes as they have difficulty applying nN-scale loads[104,105]. Magnetic cytometry uses a similar approach, but instead of encasing a bead within an optical trap, magnetic particles embedded in the cell are excited with an external magnetic force[106].

Lastly, MEMS devices have also been used to measure outside-in forces. AFM-like nano-pickers and micro-putters have been used to selectively remove cells from a substrate by directly-applied brute force, with each method reporting ~25 nN required to do so[81,107]. Microplate

stretchers developed by Thoumine et al. in 1999 demonstrated that a cell could be adhered between two parallel plates, and as one plate is moved relative to the other, the deflection of the second plate could be monitored and the corresponding force could be calculated[108]. The authors found that maximum cell adhesion force was between 5 nN and 100 nN, and that unperturbed cells would exhibit an inside-out force of approximately 40 nN. In all, the mechano-biological community has developed multiple methods of measuring cell forces each with its own set of advantages and disadvantages.

2.4.3 Nanofiber-based Platforms

Prior to the introduction of STEP force measurement scaffolds, fiber-based ECM mimicking platforms for measuring single and multi-cell forces had not been developed due to the difficulty in fabrication of fibrous substrates with tunable mechanical properties capable of capturing cell-scale force magnitudes. Fibers are known to elicit changes in cell adhesion, migration, cytoskeletal arrangement, and other phenomena such as reversible blebbing in cancer cells[15,109]. It is therefore of interest to develop a fiber-based platform capable of both inside-out and outside-in force measurement. Recently, we have demonstrated the ability to produce hierarchical assemblies of aligned nanofibers *via* the non-electrospinning STEP technique, which can be used to calculate single cell forces[110]. The force scaffolds are fabricated with fibers of controlled diameters in dual layers that are fused at fiber intersections. The result is a suspended force measurement system of tunable structural stiffness (N/m) which allows real-time passive inside-out cellular forces to be captured. A major focus of this work is therefore to couple the fiber-based STEP force scaffolds with an external perturbation system so that additional mechanical characteristics of the cell such as adhesion force can be measured. The STEP probe perturbation system offers the ability to examine mechanical interactions between cells and nanofibers,

including contributions of parameters such as structural stiffness and substrate curvature effects. A summary of force measurement approaches and their capabilities and strengths are provided in the table below.

Table 2-2. Comparison of cellular force measurement techniques and their capabilities (blue), limitations, (red) strengths (green), and unknown areas (gray).

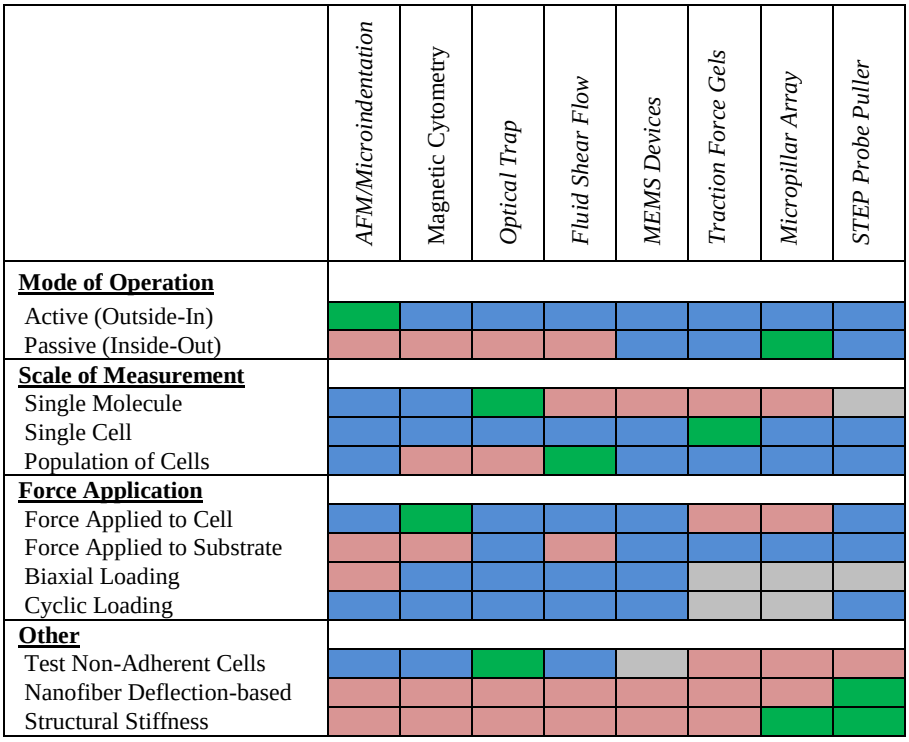

2.5 Summary and Specific Aims

A cell's behavior is dependent on the physiochemical environment it interacts with, and in the body this environment is predominately fibrous. Evaluation of single cell-fiber interactions which ultimately drive such behaviors has proven difficult due to challenges in depositing nanofibers with control of diameter and spacing in single and multiple layers. The STEP technique addresses these challenges without the use of an electric source and provides a robust and repeatable nanofiber deposition platform for investigating cell-fiber interactions critical for

advancement of fiber networks as assays for tissue engineering-based therapies. The work detailed herein uses this technology to investigate fundamental cell-suspended fiber-interactions (Chapter 3), implements these findings to develop force-measuring scaffolds that demonstrate both inside-out and outside-in directional force measurement capabilities (Chapter 4), and uses the resulting framework to advance our understanding of diseased cell behavior at the single-cell level (Chapter 5). Compared to state-of-the-art flat substrate or cantilever-based force measurement platforms, findings from this work will allow biophysical interpretation of force modulation on substrates mimicking the ECM.

3. ELUCIDATING CELL-FIBER INTERACTIONS

3.1 Materials and Methods

3.1.1 STEP Scaffold Manufacturing Parameters

In this work, the STEP technique was used to spin suspended nanofibers across hollowed-out square plastic sheets. STEP is a pseudo dry spinning process based on polymer molecular chain entanglement density. Polystyrene (PS) (M_W: $2e6$ g/mol dissolved in xylene to various wt.% to achieve 300, 500, and 800nm diameters) scaffolds were created using the previously-reported STEP platform, which deposits high-aspect ratio micro/nanofibers in highly-aligned arrays[68,70]. Briefly, polymer solution was pumped through a spinneret and collected as aligned fiber arrays of varying fiber length, diameter, spacing, and orientation/hierarchy. Fiber length can be adjusted by altering the length of the hollowed-out portion, but was kept constant here at 4mm. Fiber diameter was adjusted based on molecular chain entanglements, wherein larger diameter fibers can be created using polymer solutions which have either higher molecular weight or are used in higher concentrations. Spacing was adjusted by changing the rotational speed of the substrate holder or the translational speed of the stage during spinning. Hierarchical assemblies (including criss-cross intersecting fibers) were assembled one layer at a time, and the angle between adjacent layers was controllable.

3.1.2 Cell Culture

After fabrication, STEP scaffolds were tacked down to glass-bottom 6-well plates (MatTek Corp., Ashland, MA). Fibers and flat PS control surfaces were sterilized by adding 2 ml 70% ethanol for 10 minutes, then coated in 2 μg/ml fibronectin (Invitrogen, Carlsbad, CA), a commonly-used ECM protein known to aid in cellular attachment[111,112]. C2C12 mouse myoblasts

(ATCC, Manassas, VA) were cultured in DMEM cell culture media supplemented with 10% fetal bovine serum and 1% penicillin/streptomycin (HyClone Laboratories, Logan, UT). Cells were seeded onto the scaffolds *via* 35 µl droplets of cells at a concentration of 100,000 cells/ml. Cells were then given 4-6 hours to attach, and then an additional 2 ml media was added.

To further probe the effects of the cytoskeleton on attachment and migration on STEP fibers, cells were treated with cytoskeletal protein-altering drugs blebbistatin (Sigma Aldrich, St. Louis, MO), nocodazole (Sigma), and cytochalasin-D (Enzo Life Sciences, Farmingdale, NY) diluted in dimethyl sulfoxide (Thermo Fisher Scientific, Waltham, MA). Drugs were administered as single doses at commonly-used concentrations of 20 µM, 10 µM, and 5 µM, respectively, and incubated one hour prior to analysis to ensure inhibition[113–117].

3.1.3 Time-lapse, Fluorescence, and SEM Imaging

STEP scaffolds containing attached cells in 6-well plates were placed in an incubating microscope with a digitally-controlled X-Y-Z stage (Zeiss AxioObserver Z1). Images were taken at 20x and 40x magnification (0.8 and 0.75 NA, respectively) using a Zeiss AxioCam MRm camera. Time-lapse movies were created by capturing still images at marked locations every 10 minutes for 12 hours. Cell displacements were measured by tracking the location of the nucleus over time. Individual maximum cell velocities were calculated by determining the maximum displacement over any one-hour time interval from all overlapping time intervals thoughout the timelapse and dividing that maximum displacement by one hour. Strict definitions of cells shapes were adhered to: ‘spindles’ formed two points of contact along a single fiber axis, ‘parallels’ spread the gap between parallel fibers, and ‘polygonals’ formed four or more points of contact in each cardinal direction on intersecting fibers. Since cells would encounter various fiber configurations and change their shapes while migrating on the scaffolds, migration was only tracked during the

time a single shape was maintained. Cells which did not persist in a single direction of movement, travelled slower than 5 μm/hr, or which contacted other cells were not considered for migration speed measurements.

Fluorescent images were taken of the cells configured on various substrate types with the Axio Observer Z1 scope. Cells were fixed in 4% paraformaldehyde, permeabilized in a 0.1% Triton X100 solution, and blocked in 10% goat serum. Primary goat anti-paxillin antibodies (Invitrogen) were diluted 1:250 and incubated at 4°C for 1 hr. Secondary goat anti-rabbit antibodies conjugated to Alexa Fluor 488 (Invitrogen) were then added with a 1:100 dilution of rhodamine phalloidin (Santa Cruz Biotechnology, Santa Cruz, CA) and placed at room temperature for 45 minutes protected from light. DAPI counterstaining was performed by adding 300 nM DAPI (Invitrogen) for 5 minutes. Scaffolds were kept hydrated in 1 ml phosphate buffered saline (PBS) during imaging. Planar FAC length measurements were made using built-in AxioVision software. Due to difficulties in resolving individual FACs on curved fibers, the term 'FAC cluster' is adopted to signify the apparent length of adhesions emitted by fluorescence.

Scanning Electron Microscopy (SEM) images were taken using the FEI Quanta 600 FEG Environmental SEM (ESEM), operated at 10 kV beam voltage. Samples were coated in gold-palladium before imaging to enhance signal quality.

3.1.4 Statistical Analysis

Sample populations were tested for statistical significance using Tukey's HSD test. Calculations were carried out in JMP10 software. Significant differences were considered to have a p-value ≤ 0.05 unless otherwise noted. Error bars in images depict one standard deviation unless otherwise noted. Significant differences between populations are marked with an asterisk (*). Migration speeds are reported as average ± one standard deviation.

3.2 Results

3.2.1 Scaffold Design Promotes Three Cell Shapes

On flat substrates, cells exhibit a spread morphology and do not preferentially migrate in any direction, forming adhesions in random locations and orientations relative to one another. On STEP scaffolds, however, substrate attributes such as surface topography necessarily force cells to attach differently than they would when unrestricted on flat PS. Instead of being able to probe multiple migration directions, cells on STEP scaffolds are forced to travel along fiber axes, causing them to take on different morphologies and migratory tendencies (**Figure 3-1**). On scaffolds in which fibers were spun in a single layer and at relatively large inter-fiber lateral separation distances (>20 μm), cells attached to and spread along a single fiber axis, taking on a spindle-like morphology. These cells primarily formed two clusters of FACs, one at each end of the cell body, although trace amounts of adhesions were located closer to the nucleus as well. As the gap between parallel fibers was decreased (<20 μm), cells were able to attach between them, spreading into a stable configuration in which it attached to two parallel fibers. These 'parallel' cells again formed adhesions predominately at the cell periphery, but did so along both fibers for a total of four primary clusters. Lastly, fibers were spun in double layer criss-cross fashion, yielding intersecting fibers. Cells that attached to these intersections formed stable polygonal morphologies in which a FAC cluster was formed in each direction on the two intersecting fibers for a total of four or more clusters.

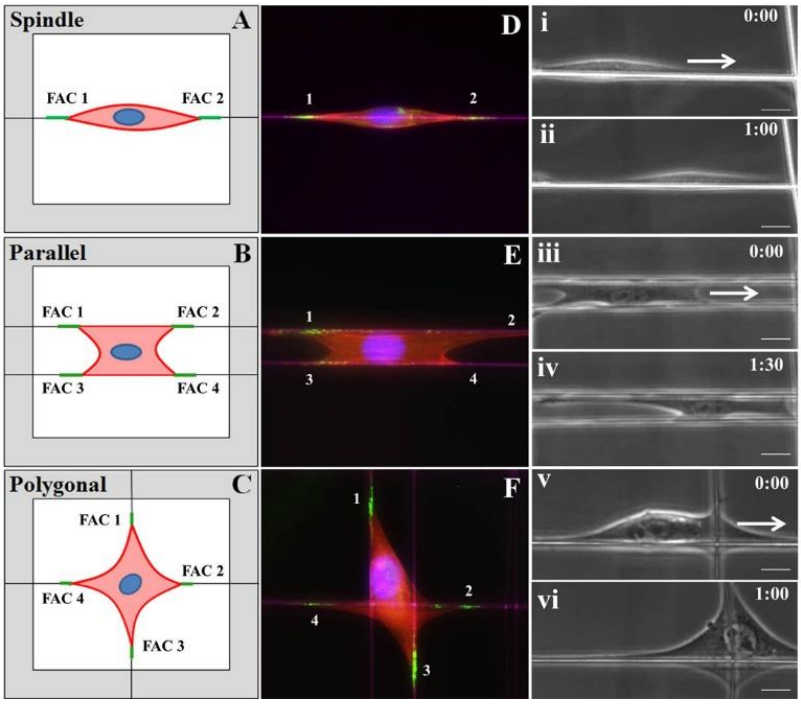

Figure 3-1. (A,B,C) STEP scaffold geometries yield specific cell shapes during attachment and migration. Fiber layouts used to get cells to attach in spindle (D, i-ii), parallel (E, iii-iv), and polygonal (F, v-vi) shapes, with roman numerals showing time-lapse phase images of the mode of migration for each cell shape. Red = F-actin, green = paxillin, and blue = nucleus. Scale bar 20 μm. Reproduced with permission[5].

Cell Spreading and Nucleus Shape Affected by Fiber Diameter

On SS substrates, which are devoid of intersecting fibers, cells had a high tendency to elongate along a single fiber and take on the spindle morphology. Since these cells only form two adhesion sites and can only migrate along a single fiber axis, they present the simplest case for studying the role of fiber diameter in cell attachment and migration. Fibers of 300, 500, and 800 nm diameter were spun to the same lengths and cells were seeded on them. Changes caused by increasing the fiber diameter were noted by staining the cells, taking fluorescence images, and measuring cytoskeletal dimensions. Three specific cytoskeletal lengths were measured to characterize cell attachment profile: the cell stretch length from the nucleus to the end of the focal adhesion (X1), the cell width at the center of the nucleus (X2), and the length of the focal adhesion

itself (X3). These three measurements characterize the amount of cell spreading and the extent of FAC growth (**Figure 3-2**).

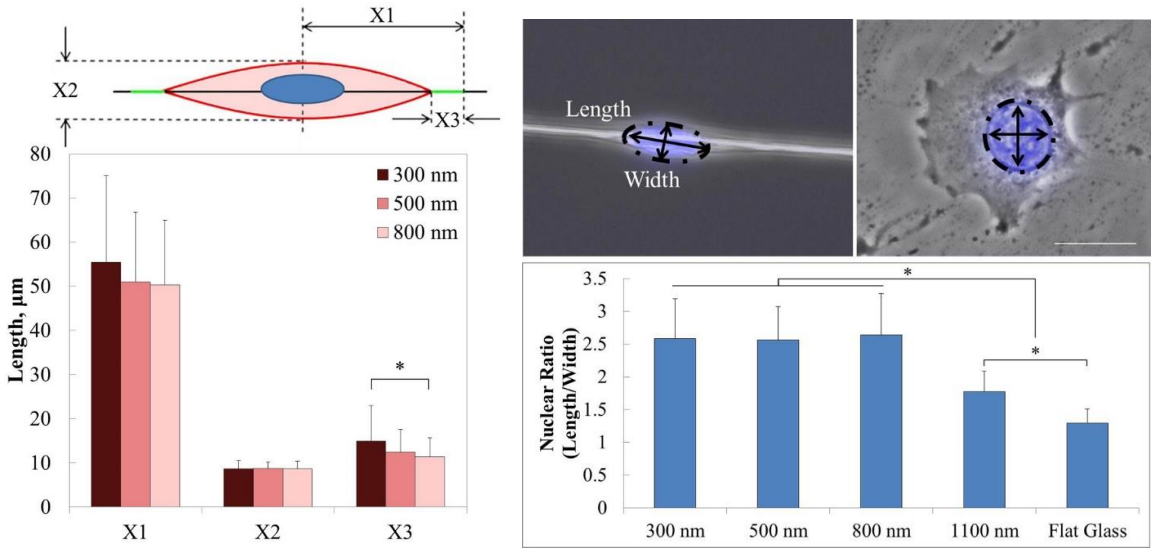

Figure 3-2. Left: Measurements of physical subcellular organelle positioning as a function of varying fiber diameter from 300 – 800 nm. * = indicates statistical significance ($p<0.01$, N = 200). Right: Nuclear ratio (length/width) of cells on flat compared to STEP fibers. * = indicates statistical significance ($p<0.05$, N = 50). Scale bar 20 µm. Reproduced with permission[5].

Data demonstrates that the spindle-shaped cells form statistically longer FAC clusters (X3) on smaller diameter fibers. Interestingly, the peak cell width (X2) remains relatively constant at each fiber diameter. Nucleus shape measurements revealed that spindle cells on 300 – 800 nm diameter fibers had an aspect-ratio approximately double that of flat cells, a value which only changed when fiber diameter was increased to over 1000 nm while maintaining the same fiber length. Recent studies have suggested that the nuclear envelope is much stiffer than the cell's membrane structure, making it more resistant to shape change compared to the rest of the cell body[118]. On STEP scaffolds, the nucleus maintains a similar width as the cell stretches to greater extents on the smaller fibers. Additional elongation of the cell body is prevented by the cell's inability to generate forces needed to tear the nucleus or nuclear lamina[119]. Alterations to this nuclear aspect ratio have been directly related to changes in gene expression in past studies,

suggesting that controllable geometrical parameters such as fiber diameter affect cell function through their interaction with fiber curvature and topography[120].

3.2.2 Adhesion Formation and Clustering

On a rigid or stiff flat surface void of topographical features, cell attachment is initialized when the dimer transmembrane protein integrin is activated upon binding of a suitable substrate ligand such as collagen or fibronectin[111,121]. Intracellular scaffolding proteins talin and paxillin are quickly recruited with focal adhesion kinase (FAK) to the site of activated integrin and link to cytoskeletal filamentous actin (F-actin), forming a nascent adhesion capable of sensing the mechanical state of the substrate. As myosin-II applies tensile load to F-actin filaments, the nascent adhesion tugs against the substrate and develops into a focal adhesion marked by the presence of α-actinin-bundled F-actin stress fibers[114]. By gradually pulling harder and harder, the focal adhesion subsequently matures into a focal adhesion complex (FAC) after the recruitment of additional late-stage proteins like vinculin and zyxin which serve to further stabilize and strengthen the adhesion, allowing it to tug even harder against the substrate[122,123]. Microtubules, kinesin-1, dynamin and phosphatases facilitate the disassembly of FACs from the rear end of the cell which are believed to be recycled to the leading edge of the cell[124]. Since the degree of maturation depends on the substrate's ability to withstand forces applied by the cell in this handshake process, the size and orientation of FACs reveal not only the contractile state of the cell but also the rigidity of the substrate. Imaging these structures allows one to visualize locations where cells are physically forming contacts, identify load-bearing structures of the substrate, as well as define force vectors along which cells apply contractile loads required to migrate. Therefore, FACs are commonly used as indicators of both substrate stiffness and migration speed on flat surfaces[125,126].

While these developmental mechanisms likely remain unchanged, suspended fibers topographically force cells to make spatial adaptations which challenge simple FAC size-migration speed correlations. Instead of having a limitless surface area to form adhesions, cells on fibers are forced to attach within a spatially limited, curved substrate. Surface area limitations cause the cell to probe for additional space to form adhesions by elongating down the transverse axis of the fiber[127,128]. In the elongated state, the cell arranges itself by partially wrapping around the fiber's curved surface. The end result is that the cell forms morphologies with adhesions circumferentially clustered at the poles as opposed to the spread shapes with diffused adhesions throughout seen on flat surfaces[129,130]. To further investigate this behavior, cells were treated with cytoskeleton-altering drugs in aforementioned concentrations and then observed for changes to migration behavior and cytoskeleton arrangement compared to control non-drugged cells. Blebbistatin, a myosin II inhibitor, is known to cause reduced actin-based cellular contraction and disrupt the rigidity-based sensing mechanism that allows for FAC growth on flat geometries[114,131,132]. Similarly, the microtubule interfering drug nocodazole was used to disrupt microtubule-induced cell polarization and limit cell division[133,134]. Cytochalasin-D is a known inhibitor of F-actin polymerization and has been shown to eliminate cell migration on flat surfaces[135,136].

Flat control, spindle, parallel, and polygonal cells are shown in different imaging modalities to demonstrate morphological differences of stress fibers and FAC clusters as a function of fiber geometry for both non-drugged and drugged cases (**Figure 3-3**).

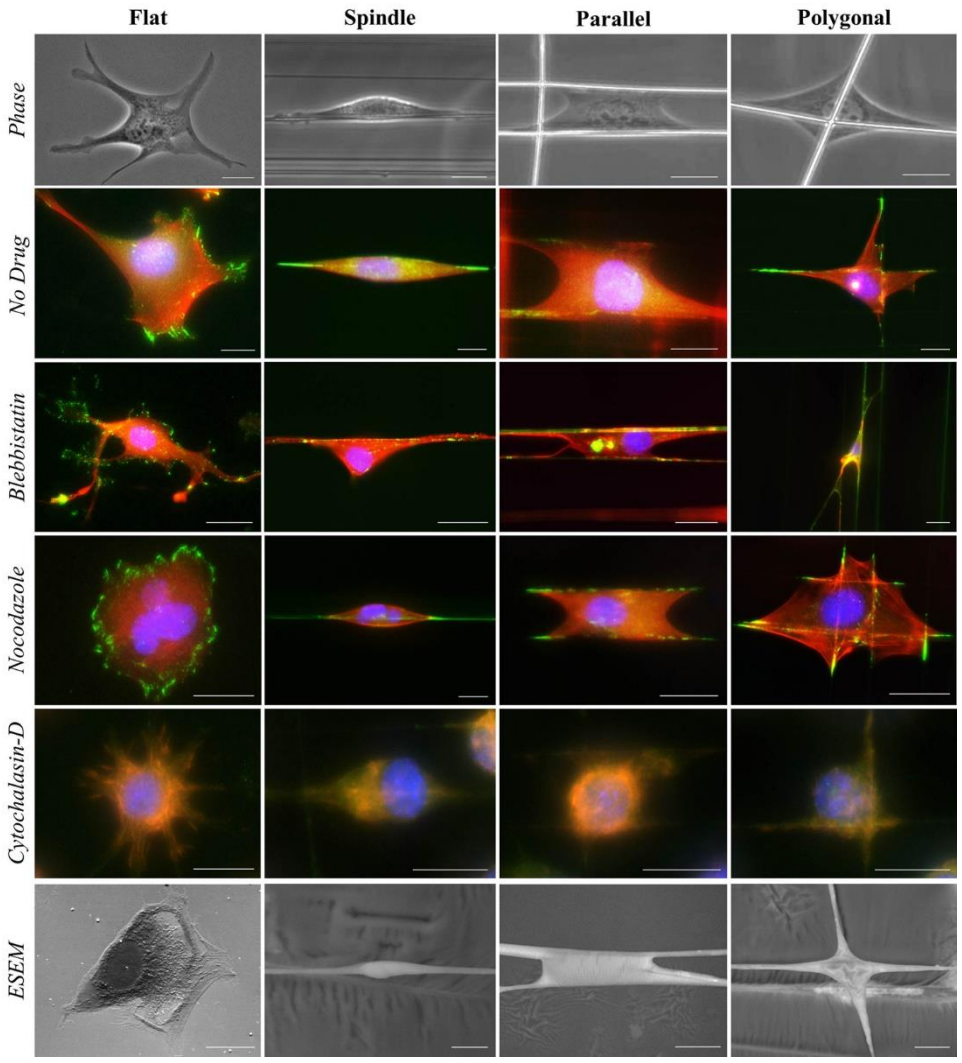

Figure 3-3. FAC cluster morphologies on different STEP fiber geometries and as a result of administered drug. From left to right: flat, spindle, parallel, and polygonal-shaped cells. Red = F-actin, green = paxillin, blue = nucleus. Flat pictures shown here were taken on flat glass substrates to reduce PS auto-fluorescence artifacts since physical appearances of the cells are similar on both. Scale bar 20 μm. Reproduced with permission[5].

Phase microscopy shows that on the flat PS sheets, cells spread in random directions since the underlying geometry does not provide any directionality or polarity to the cell. Fluorescence imaging shows the formation of prominent stress fibers and numerous FACs on flat PS. In addition, multiple adhesion clusters form throughout the cell periphery and do not appear geometrically confined in any direction. On STEP fibers, the topography of the fibers limits the possible cellular attachment sites and causes the cell to spread into a repeatable shape. Spindle shaped cells, for

example, only form two attachment clusters, one on each end. In the parallel configuration, the cell is able to form more attachments along the fibers, but these remain localized towards the cell periphery. The same is true for the polygonal cells, whose migratory stability may partly be attributed to the formation of four or more oppositely directed adhesions, thus allowing the cell to contract inward from each direction.

Cytoskeleton-altering drugs induced changes to FAC formation in cells both on flat and fiber substrates. Cells dosed with blebbistatin demonstrated reduced FAC growth, a phenomenon attributable to the knockdown of the cell's myosin-driven rigidity sensing mechanism. On the other hand, nocodazole induced alterations to normal mitosis without dramatically altering FACs. These cells experience alterations to the normal cell cycle and often fail to split properly, leading to multinucleated cells which remain confined to their shape-driven attachment configuration. The most dramatic change to cytoskeletal elements were caused by administration of cytochalasin-D, which prevents F-actin from polymerizing. These cells were unable to stretch or form significant FACs on substrates, and instead exhibited a rounded morphology and remained stationary.

FACs were further probed on STEP fibers for each shape-drug combination. Fluorescence microscopy was used to measure the distance FACs were located away from the center of the nucleus (**Figure 3-4**). In the parallel and spindle shapes, FACs were located slightly further away from the cell center when treated with blebbistatin. Cytochalasin-D prevented cells from spreading as seen by the 18-20 μm length for all shapes. FACs from nocodazole-treated cells were found at a similar distance to control cells. In addition to examining their locations, the FAC cluster lengths (autologous to previously-measured X3), were measured. FAC length data for each drug was then normalized to the no drug flat PS condition to determine changes seen in FAC maturation when attaching to suspended fibrous surfaces. With the exception of cytochalasin-D, which prevented

FAC formation, each cell shape-drug combination formed longer, more concentrated adhesions compared to its flat PS counterpart. In both blebbistatin and nocodazole treated cells, each shape displayed a nearly fourfold increase in FAC length on fibers compared to flat PS.

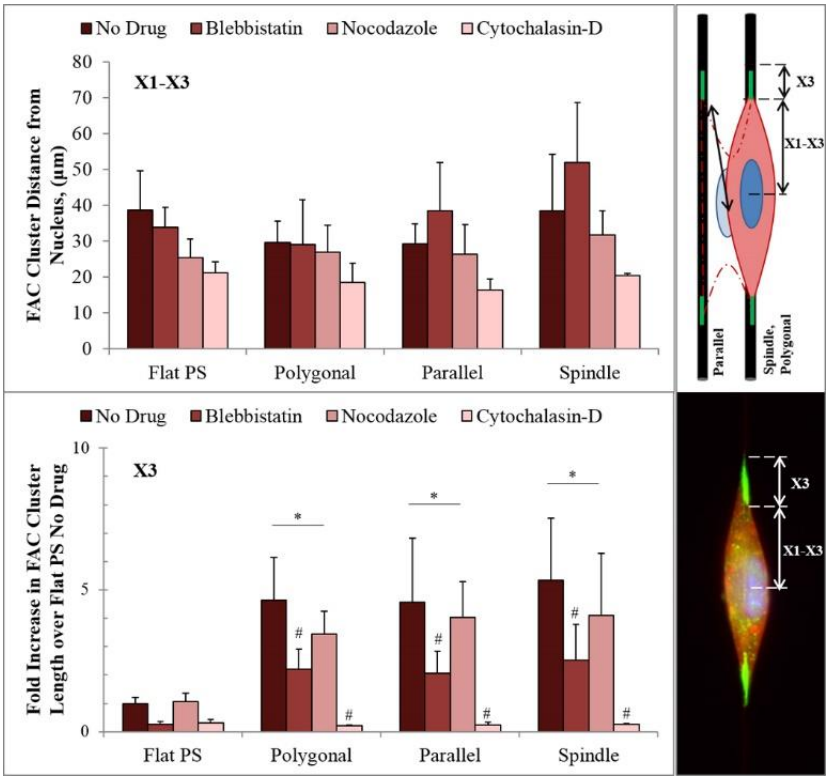

Figure 3-4. Increases in apparent FAC cluster distance away from nucleus (X1-X3) as a function of cell shape and administered drug, and FAC length (X3) comparisons for each drug-shape combination. The schematic and image to the right define how lengths were measured, with distance from nucleus taken as 'X1-X3' and FAC length taken as 'X3'. * indicates statistical significance compared to 'Flat PS' of same drug, # indicates statistical significance compared to 'no drug' of same shape ($p<0.01$, N=150). Reproduced with permission[5].

While other studies have measured similar FAC lengths on flat substrates (2-6 µm), this data for the first time demonstrates the primary differences between FAC organization in cells attached to flat, featureless substrates and suspended, aligned STEP fibers, which produce FAC clusters up to 12 µm in length[130,137].

3.2.3 Migration - Adhesion Relationship

Cell migration is relevant to a myriad of physiological phenomenon including developmental processes and diseased conditions. The transition from cell attachment to cell migration is facilitated by cell polarization that forms distinct leading and trailing edges and propels the cell forward *via* actin-myosin machinery-based traction forces. It would appear by looking only at their increased FAC size that that cells on fibers would be more temporally stable and less migratory than on flat surfaces, yet due to enhanced FAC alignment and polarization of contractile forces, cells have the capacity to nearly double their migration speed on such structures. Unlike migration on flat substrates, cells can only migrate along fibers when they are interacting with suspended fiber-based scaffolds.

Noting that FAC positioning and length changed according to cell shape and administered drug, migration speeds were then measured for spindle, parallel, and polygonal cells to determine if FAC formation was related to migration dynamics (**Figure 3-5**).

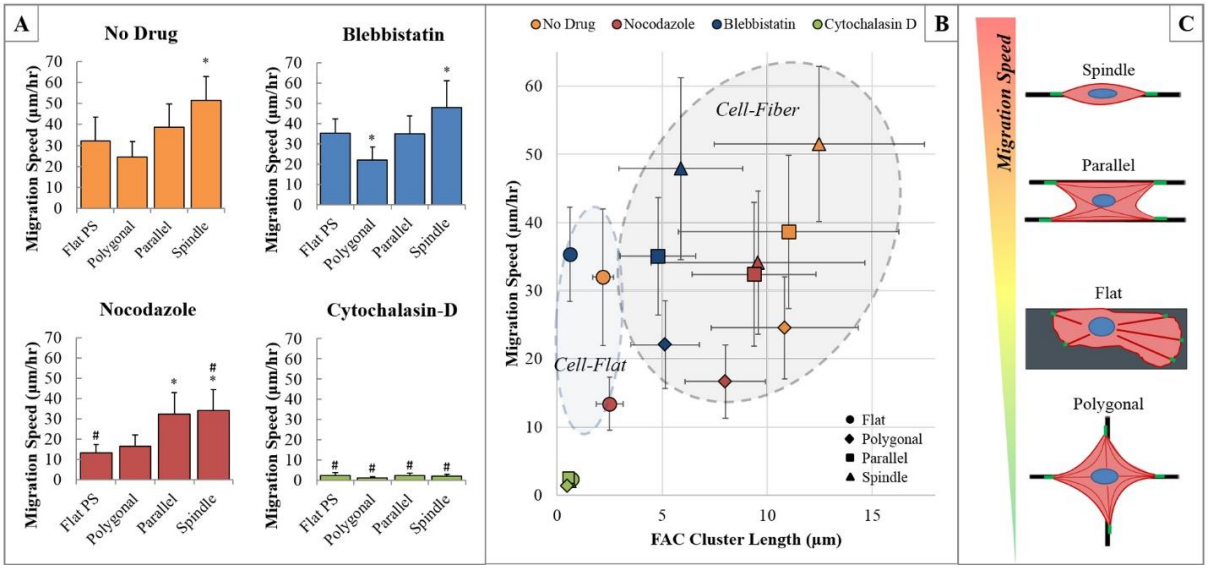

Figure 3-5. C2C12 migration speed as a function of cell shape and administered drug. * indicates statistical significance compared to 'Flat PS' of same drug, # indicates statistical significance compared to 'no drug' of same shape ($p<0.01$,N=200). Reproduced with permission[5].

In the absence of drugs, spindles were found to migrate the fastest of each shape at approximately 52 ± 11 μm/hr. These cells are attached to a single fiber and therefore elongate to form two stable adhesion clusters to remain attached to the fiber. Due to high topographic restriction, spindles inherently exhibit biophysically-induced stretch along the fiber axis, forcing the cell into a more polarized state with aligned traction forces. F-actin polymerization, which causes membrane protrusion at the leading edge, can only occur forward or backward along the fiber axis in this shape, preventing cell probing in multiple directions and perhaps contributing to increased migration speed. Cells attached in the parallel configuration displayed slightly slower migration speeds (39 ± 11 μm/hr). In this shape, cells form additional adhesion clusters and are allowed comparatively more directional freedom as they are attached to two fibers instead of one. The migration speed decrease is attributed to the ability of the cell to contract in more than one direction. These effects are more pronounced in the polygonal cells, whose 25 ± 7 μm/hr average migration speed is due to the geometrically imposed development of often observed orthogonally-oriented FACs and stress fibers.

Upon blebbistatin administration, cells migrated at a similar speed to control cells (flat substrates) despite their inability to develop mature adhesions. These cells were found to migrate at different speeds while in different shapes, indicating that substrate topography affected cell migration. Spindle cells, with the greatest geometrical restriction, traveled at 48 ± 13 μm/hr. As cells spread across two fibers in the parallel configuration, migration dropped slightly to 35 ± 9 μm/hr, and polygonal shaped cells slowed to 22 ± 6 μm/hr. Flat cells traveled at 35 ± 7, slightly faster than the no drug control cells on flat PS. This observation builds upon previous studies which showed that blebbistatin-treated cells travel more quickly than control cells on flat surfaces despite a reduction in overall traction force[138]. Disruption of non-muscle myosin II is thought to cause

cells to spontaneously cluster F-actin on flat substrates, thereby self-imposing a polarized phenotype even in the absence of directional cues, a phenomenon quantifiable by significantly reduced cellular circularity compared to control cells which were not under drug culture conditions[113,139].

Nocodazole treatment slowed migration speeds compared to normal cells in all shapes. Cell cycle progression was dramatically slowed and cells were observed to spend a significantly longer period of time attempting to divide. Upon failing to split, these cells would often merge with one another and become multinucleated. Despite these alterations to normal cell behavior, the cells still demonstrated topography-induced alterations to migration speed, with spindles and parallels traveling fastest (34 ± 10 μm/hr and 32 ± 11 μm/hr, respectively) followed by polygonals (17 ± 5 μm/hr) and flats (13 ± 3 μm/hr). Cytochalasin-D prevented F-actin from polymerizing, resulting in a complete loss of migration. Unable to protrude their membranes, these cells balled up both on flat substrates and on fibers, and no significant difference in migration between shapes was observed. Taken together, data indicates that migration-adhesion relationships occur within entirely separate zones on flat substrates and suspended nanofibers, and that these zones remain separate even when cytoskeletal drugs are introduced to each shape configuration (Figure 7).

3.3 Summary and Conclusions

Cells on fiber-based scaffolds exhibit different morphologies and cytoskeletal arrangements than those on flat surfaces. While distinct sheet-like lamelliopodia and finger-like filopodia actin structures are observed on flat substrates, cells observed to wrap around the fibers, extend minor finger-like projections, and do not typically display distinct sheet-like lamelliopodia structures. Furthermore, focal adhesion patterns are clustered at the poles of the cells and are rarely found towards the interior. Since the cell is confined to a single fiber, it is forced to migrate along

a single axis. When a second fiber is placed parallel to the first fiber at a relatively close spacing (<20μm), the cell is able to bridge the gap between them and take on a spread morphology. At higher gap spacing, the cell cannot interact with the second structure and remains confined to the single fiber. Lastly, when an intersecting, perpendicular fiber is placed, the cell will form a stable configuration at the intersection.

Fiber curvature and topography cause cells to form FACs in a limited space at the cell periphery, allowing them to inherently concentrate and align to the fiber direction. While traditionally considered a hallmark of a slowly-migrating cell, this data suggests that concentrated focal adhesions carry greater potential to generate migration-inducing forces, and that the alignment and polarization of these adhesions as a result of surface topography ultimately determines resultant migration speed. To the best of our knowledge, this is the first study demonstrating a marked four-fold FAC length increase on suspended fiber topography. In contrast to studies using patterned flat substrates, this work shows the importance of suspended fiber dimensionality and fiber curvature on FAC organization and related cellular migration.

4. DEVELOPMENT OF THE OUTSIDE-IN PROBE SYSTEM

4.1 Materials and Methods

4.1.1 Nanofiber Structural Stiffness vs. Substrate Elastic Modulus

The ability of a material to resist deformation under a given load is referred to as its elasticity. Young's modulus of elasticity (E, units: N/m^2) is an *intrinsic* descriptor of such material-dependent behavior, yet does not fully describe an object's response to loading. For instance, metallic materials generally have a much higher Young's modulus than polymers, but depending on the object's cross-sectional size and shape, a polymer-based column can be formed to hold more weight than one composed of metal. In other words, an *extrinsic* shape-dependent descriptor is also required when investigating the mechanics of a material to be used as a deflection-based force sensor. This extrinsic parameter is known as stiffness (k, units: N/m) and varies according to the specific object under question.

In this work, nanonets are used to measure cell forces based on the deflection of suspended nanofiber beam segments. Similar to a tightrope, the stiffness of a suspended nanofiber of constant diameter and length changes depending on the position along the length of the fiber (**Figure 4-1**). According to beam theory, stiffness is highest at the fiber's edges and lowest at its center. Objects that interact with the fiber along its axis are subject to a stiffness gradient. Cells that pull on these fibers do so within an attachment range, so any single number value that is selected to represent the apparent stiffness that the cell sees cannot fully capture such interactions. However, it is important to note that while stiffness theoretically approaches infinity at the fiber-fiber intersection, it maintains a relatively stable value in the middle 60% of its length. As long as the cell is relatively centered on the fiber, the gradient can be negligible. Nonetheless, a single structural stiffness value must still be presented as it is one of the primary driving forces behind

cytoskeletal development and force generation, so we assume that the nominal or 'apparent' stiffness of a cell-fiber interaction to be the stiffness at the geometrical center of the cell.

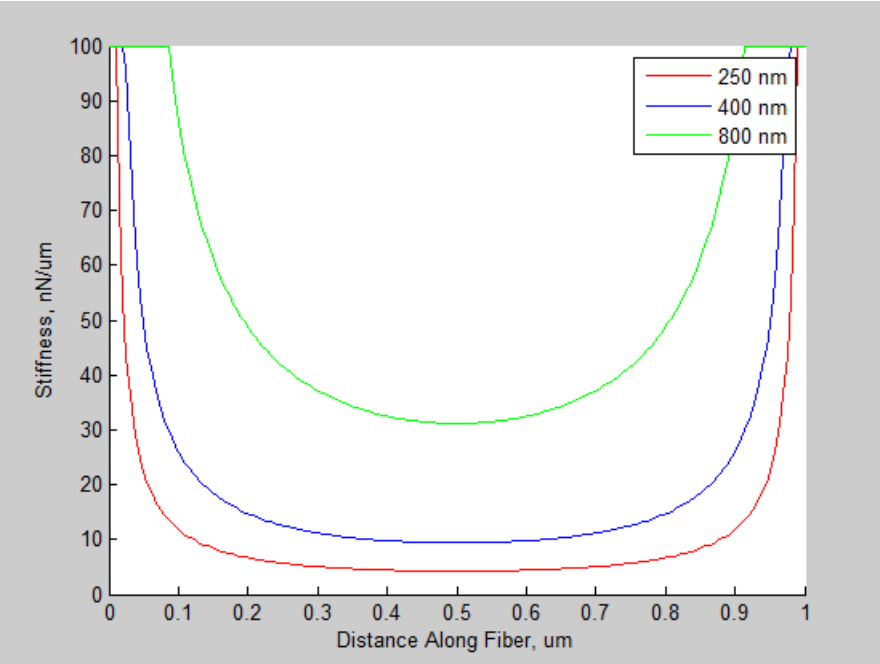

Figure 4-1. Structural stiffness profile of nanonet fiber segment for each fiber diameter tested.

Contributions of nanofiber structural stiffness originate from both the cross-sectional shape and size of the fiber as well as from tensional axial stresses as a result of the STEP fiber formation process. The rotating substrate initially comes into contact with a solution droplet, which contains enough molecular chain entanglements to draw out a filament. We speculate that as the filament is stretched from substrate rotation, solvent molecules continue to evaporate, forming and solidifying the fiber but incurring shrinkage and tensional stresses as a result. The magnitude of the contribution of axial tension is such that it dominates the structural stiffness profile of STEP fibers. Without this term (quantified by Ji Wang, see Appendix), theoretical models severely underestimate actual fiber stiffnesses measured with AFM-based approaches.

4.1.2 AFM Testing for Confirmation of Single Fiber Mechanics

Fiber length, diameter, and residual pre-tension from the spinning process described above all contribute to the fiber's inherent structural stiffness which varies according to position along the length of the fiber. Since they are extrinsic properties, we can obtain theoretical estimations for stiffnesses of a given nanofiber but wanted to measure using AFM ramp tests for confirmation of our modeling approach.

To measure structural stiffnesses, ramp plots were created at the center of individual fiber span lengths using tipless AFM cantilevers of low stiffness (~0.2 N/m) (**Figure 4-2**). In the ramp plot test, the cantilever pushes the fiber downward several hundred nanometers using a piezo actuator. The AFM records and plots the amount that the cantilever bends (deflection measured by laser movement) as a function of how far the cantilever was lowered ('Z' height). The stiffness of the fiber affects the amount that the cantilever deflects for a given change in its height. Fiber deflection can be obtained by recognizing that system deflection is conserved, i.e. $\delta_{fiber} = \delta_{piezo} - \delta_{cantilever}$. Similarly, force is obtained by multiplying the cantilever deflection by its stiffness, i.e. $F = k_{cantilever}\delta_{cantilever}$. Fiber stiffness is obtained by calculating the slope of the linear region of the force vs. fiber deflection plot. A custom Matlab routine was developed to process raw AFM output to achieve stiffness values (Appendix).

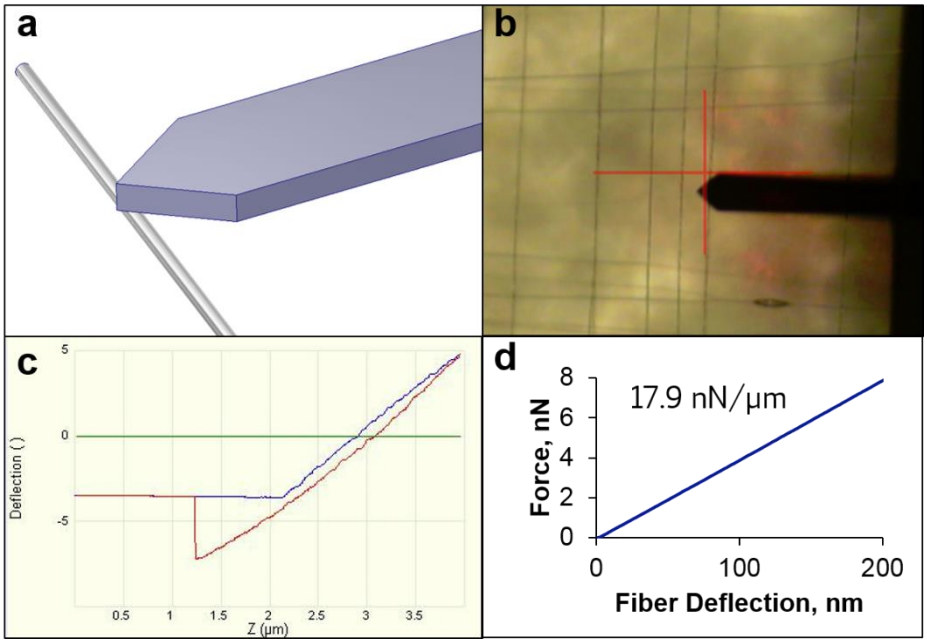

Figure 4-2. AFM-based approach for measuring nanofiber structural stiffness. (*a*) Schematic of a tipless AFM cantilever contacting a suspended nanofiber. (*b*) Optical image of the AFM cantilever in position on a nanofiber. (*c*) Sample raw data resulting from a ramp plot. (*d*) Ramp plot data is converted to force-deflection curves, the slope of which is taken to be the effective stiffness of the fiber.

Fiber stiffness at any point along its length can be theoretically estimated using modeling approaches, but it is impractical to measure each fiber's length and diameter for every nanonet developed. We therefore wanted to ensure that our theoretical approach accounted for what was being physically measured. To do this, a grid of fibers had stiffness measurements taken at the AFM, and then the same sample was brought to the ESEM for fiber diameter and length measurements. Theoretical calculations were performed using the ESEM-measured diameters and lengths and compared to the AFM-measured values (**Figure 4-3**). It can be seen that leaving the contribution of fiber tension out of the equation severely decreases estimated fiber stiffness. Fibers under tension require more force to reach the same deflection of a fiber that is not under tension.

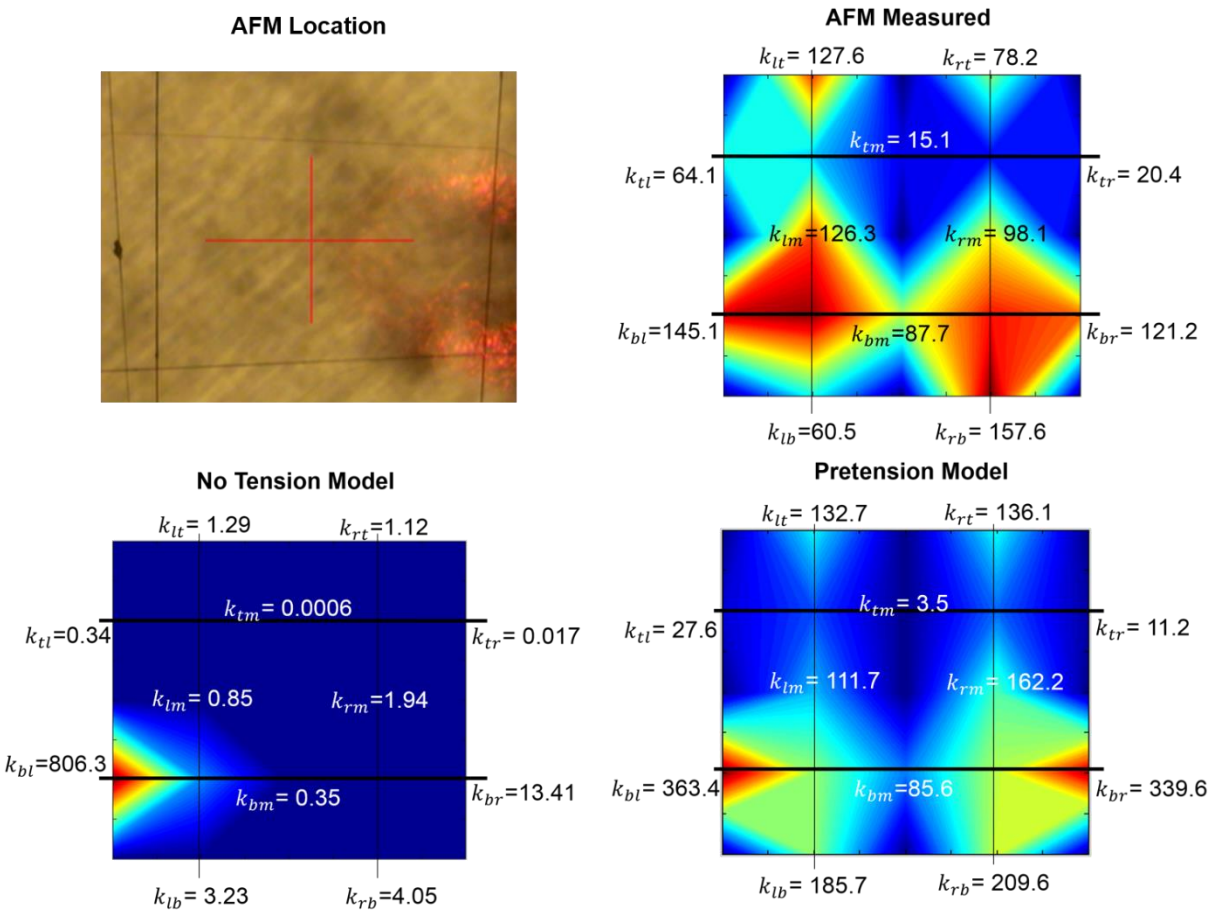

Figure 4-3. Fiber stiffness validation experiments using combined AFM and ESEM measurements.

In this particular sample, however, considerable discrepancies between AFM and theoretically modeled stiffness values exist despite the inclusion of tension. This may partially arise from the wide range of diameters and lengths examined in this sample. We therefore tested samples more closely resembling the types of fibers that would be present in nanonets, namely having a span length between 100-300 μm and diameters less than 500 nm. In this subset of data (n = 23 fibers), average error between AFM and theory was 12.6%, with both over and underestimations present. However, by assuming a constant fiber diameter (closest to either 250 nm or 400 nm), error was reduced to 10.6%. In other words, the same amount of accuracy is achieved either by directly measuring fiber diameter or by assuming it falls within a categorical

context (i.e., both 391 and 419 nm fibers are assumed to be 400 nm). Therefore, assuming fiber diameters are known beforehand based on solution behavior, individual nanonets do not require AFM- or ESEM-based confirmation of stiffnesses, reducing time required to perform experiments and measure forces.

From a design standpoint, the fibers should have structural stiffnesses that are soft enough to permit appreciable deformation under single cell-scale loads that can be accurately measured optically (~1 μm resolution accuracy) while simultaneously remaining stiff enough to prevent non-elastic deformations (< 5% of the span length[140,141]). For example, for a fiber span length of 200 μm, an appropriate fiber deflection would have to be kept under 10 μm. If it is assumed based on findings from other techniques that a given cell applies 100 nN, we can then find that the fibers would have to have stiffnesses that fall on the order of 10 nN/μm to meet these requirements. Using AFM with tipless cantilevers, parametric evaluation of fiber properties on structural stiffness and associated modeling were carried out and it was found that fiber structural stiffnesses acceptably ranged from ~5-20 nN/μm at the center of the fibers (**Figure 4-4**). Due to the competing contributions of fiber length and diameter, it is possible to arrive at the same structural stiffness with a short, thin diameter fiber and a long, large diameter fiber, as shown by the overlapping red and blue lines in Figure 4-4A. We also see, however, that when confined to a fiber span length within the range of 130 – 335 μm (such as those used in nanonet design), there is not much overlap in stiffnesses among different diameters (blue lines only have similar slopes to red lines in single location). This makes the study of the effect of fiber diameter at constant structural stiffness difficult unless the nanonet is specifically created beforehand with this intent.

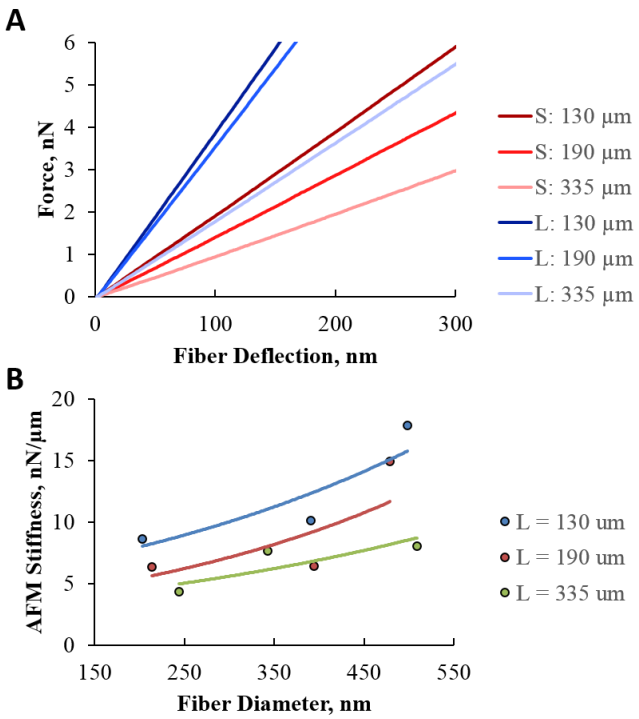

Figure 4-4. Parametric (length, diameter) AFM study of fiber structural stiffness (nN/µm). A) The slope of the AFM force-deflection curves are converted to stiffness values. The effect of fiber diameter (S: small (~250 nm, red), L: large (~500 nm, blue)) as well as fiber length (dark shading: ~130 µm, medium shading: ~190 µm, and light shading: ~335 µm) are seen by differences in slope. A short, small diameter fiber can have a similar stiffness to a long, large diameter fiber. B) Effects of fiber diameter and length on measured AFM stiffness values show that increasing diameter and decreasing length both increase stiffness.

4.1.3 Fused Scaffold Development for Inside-Out Force Measurements

Using the non-electrospinning STEP technique, suspended PS nanofibers are fabricated in a manner which causes cells to attach into repeatable configurations between two parallel fibers. Cells on suspended nanofibers tend to spread between two parallel fibers if the distance between the two fibers is less than approximately 20 µm (**Figure 4-5**).

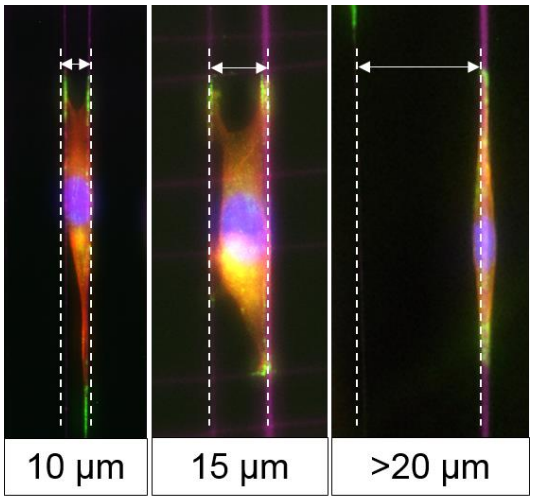

Figure 4-5. Effect of inter-fiber spacing on cell spreading. Distances less than approximately 20 µm result in parallel cell shapes which are desirable for force measurement.

This parallel cell shape is desirable since it represents the simplest case of cell-fiber interactions which result in fiber deflection. To increase the likelihood of such a cell shape occurring, ~400 nm diameter fibers were spun at spacing of ~15 µm and ~1500 nm diameter fibers were fabricated on top of and orthogonal to the previous layer with larger spacing (~200 µm). Fiber intersections were then fused together to create force scaffolds with pinned boundary conditions that allow the fibers to bend when cells apply forces on them. The fusion process was carried out by briefly re-introducing the fiber scaffolds to the vapors of their native solvent. Scaffolds were lowered into a jar containing p-xylene and held stable for two seconds, then rotated onto their other side and held stable for another two seconds. Fiber fusion is a volatile process: if the scaffolds are exposed to vapors for too long, they can dissolve to the point where their diameters narrow or they can dissolve completely. However, if exposure time is too short, fibers can experience incomplete fusion and will separate from one another with minimal force. We therefore optimized this process by establishing visual cues associated with a well-fused scaffold (**Figure 4-6**).

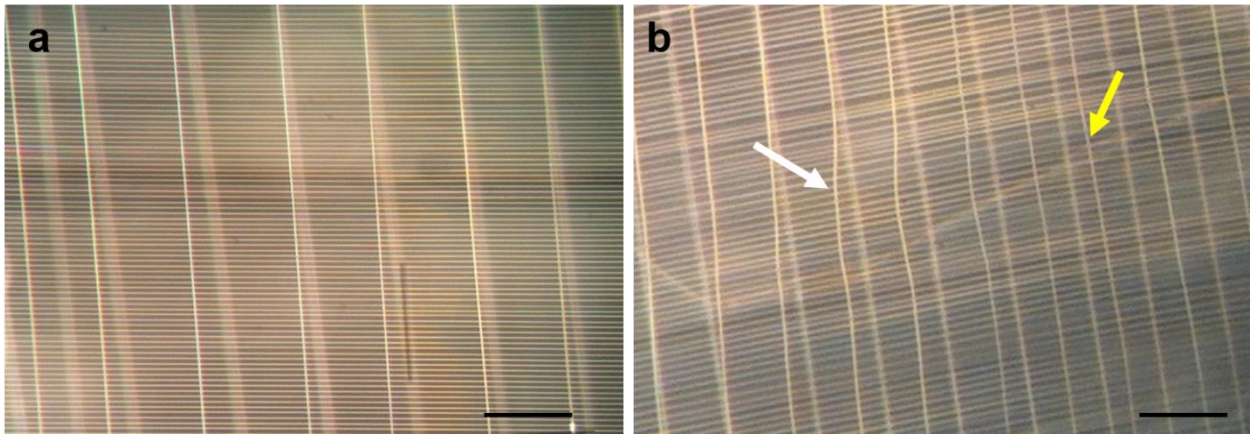

Figure 4-6. (*a*) Nanonet scaffold prior to fusing, compared to (*b*) another scaffold that has been fused. Fusion is evident by long bending arcs in the vertically-spanning fibers that are a series of straight lines connecting each fiber intersection (*white arrow*), as well as the characteristic "Y" shape of multiple fibers that have joined together at the center of the span length but are unable to do so near the intersection (*yellow arrow*).

Fibers that begin to fuse into one another leave behind a characteristic 'Y' shape when fibers are very close together. These will appear because the main body of two nearby horizontal fibers join together, but due to their simultaneous fusion at the intersection with the vertical fiber, they leave behind a 'Y' shape at the boundary (*shown in yellow arrow*). If fiber spacing is larger and the 'Y' shape cannot be seen, the vertically spanning fibers will often display a series of angled segments between each horizontal fiber which, over a larger distance, appear to take on an arc-like shape. When either of these cues can be spotted, fiber fusion can be confirmed and cell experiments can be performed.

4.1.4 Force Modeling

Prior to evaluating cell forces, the mechanics of the fibers themselves must be modeled. Similar to previously reported force measurement strategies involving inverse methods, we model the fibers as prismatic beams under uniform tension with pinned boundary conditions. We assume that a cell applies two point loads on the beam, one on each end of the cell-fiber interface (where the focal adhesions cluster). Therefore, by modifying Timoshenko's single point load model to

incorporate both point loads, the observable deflections δ_a and δ_b are related to their associated loads P_a and P_b through the following system of equations (derivation in Appendix):[142]

$$\delta_a = -\frac{P_a sinh[\lambda(L-a)]}{S\lambda sinh[\lambda L]} sinh[\lambda L] + \frac{P_a(L-a)}{SL} a - \frac{P_b sinh[\lambda(L-b)]}{S\lambda sinh[\lambda L]} sinh[\lambda a] + \frac{P_b(L-b)}{SL} a \quad \text{(Eq. 1)}$$

$$\delta_b = -\frac{P_a sinh[\lambda a]}{S\lambda sinh[\lambda L]} sinh[\lambda(L-b)] + \frac{P_a(L-b)}{SL} a - \frac{P_b sinh[\lambda(L-b)]}{S\lambda sinh[\lambda L]} sinh[\lambda b] + \frac{P_b(L-b)}{SL} b \quad \text{(Eq. 2)}$$

Where variables are defined as follows:

Table 4-1. STEP Nanonet force model parameters.

Variable	Significance	Value
L	Segmental length of the fiber (distance between adjacent pinned ends)	Variable; 100-500 μm
a	Location of point load nearest fiber-fiber intersection	$0 < a < L$
b	Location of other point load	$0 < a < b < L$
δ_a	Fiber deflection at a	Variable, 1 – 15 μm
δ_b	Fiber deflection at b	Variable, 1 – 15 μm
λ	Shape-dependent mechanics parameter	$\sqrt{S/EI}$
S	Uniform pre-tensional load	$S = \pi(d^2/4) * T$, μN
T	Uniform pre-tensional stress, calculated from AFM residual stress measurements (Supporting Information)	4.108 MPa
d	Fiber cross-sectional diameter	Variable, 250 nm – 800 nm
E	Elastic modulus of the polymer (polystyrene)	$E = 0.97$ GPa
I	Area moment of inertia	$I = \frac{\pi d^4}{64}$

4.1.5 Probe System Overview

The outside-in probe perturbation system consists of either one (single) or two (dual) glass micropipettes attached to and controlled by a three-axis precision micromanipulator (Sutter MP-285, Novato, CA). Micropipette probes were pulled from 1.0 mm diameter glass rod blanks using the P-1000 Flaming/Brown micropipette puller (Sutter) with a custom program to provide steep

gradients that promote probe durability. Precise control over probe placement, motion, and strain rate enables manipulation of individual cells at desired locations and attached in desired configurations.

Force scaffolds were placed in the incubating microscope in larger 35mm glass bottom dishes (Mattek) which enabled greater probe range-of-motion compared to 6-well plates. Lids were removed from the dishes to allow the probe to interface with the scaffolds, but doing so interfered with CO_2 incubation. To compensate, DMEM media was replaced with HEPES-buffered RPMI 1640 media during experimentation, enabling longer duration experiments to be conducted without significant changes in pH[99]. Probes were slowly lowered toward the top layer of fibers until they could be seen in the microscope camera. The probe was then positioned near cells that fit the parallel configuration and then pre-programmed for a) end-state position, b) strain rate, and c) looping (cyclic) status. To prevent buckling which would otherwise occur prior to reaching end-state position, the probe was first used to break the fusion nodes of the leading fiber (which the probe touches and pushes) as well as those of several fibers above the leading fiber prior to experimentation. Destroying these nodes permits greater deflection distances prior to inducing buckling while leaving the applied force unaffected. Time-lapse videos were captured at maximal speed (~600 ms) due to the shorter experimental timeframe and later analyzed using built-in AxioVision software (Zeiss).

4.1.6 Dual Probe System for Even Force Distribution

The dual probe was initially conceptualized such that micromanipulation would result in even strain on both sides of the cell. Initial attempts to use ultra-thin diameter copper wire (25 µm) as probes failed due to their large diameter and susceptibility to plastic deformation. Gaps in the nanonets were designed to be < 15 µm, such that the 25 µm diameter wire used (half the diameter

of human hair) would not fit between the two parallel fibers to initiate actuation. Additionally, the ease of plastically deforming the high aspect-ratio wires prevented accurate placement within<200 µm distance from one another. For these reasons, it was determined that using glass rod blanks pulled to 1 µm tips in a quick gradient could out-perform metal as a probe material.

Ideally, dual probe actuation would result in scaffold deflection in only the x-y plane, with as limited motion in the z-direction as possible to maintain focus on the sample and limit out-of-plane force vectors. To accomplish this, an annulus which would allow vertical glass probe tip placement was fabricated in CAD and 3D printed (**Figure 4-7**). Improvements over the initial design are shown in text overlaying the images.

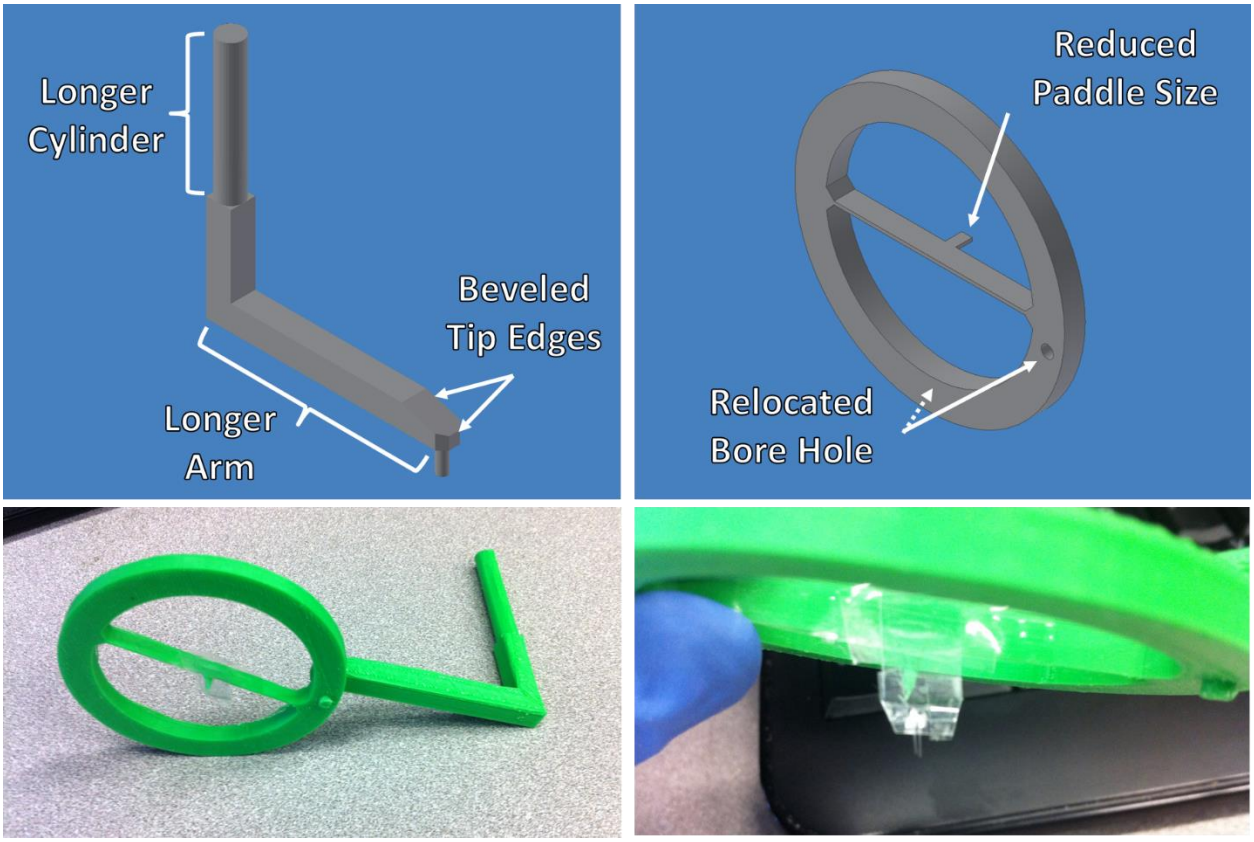

Figure 4-7. Initial design and design improvements for the annulus-style dual probe holder.

In this design, the annulus contained a paddle at the center to which the glass tips were taped. This design allowed for vertically-aligned glass probe tips which would prevent z-plane sample movement. The annulus was designed to have a diameter large enough to surround the condensing lens to minimize light path interference. Despite this design, there remained enough material in the light path to interfere with image quality (**Figure 4-8**).

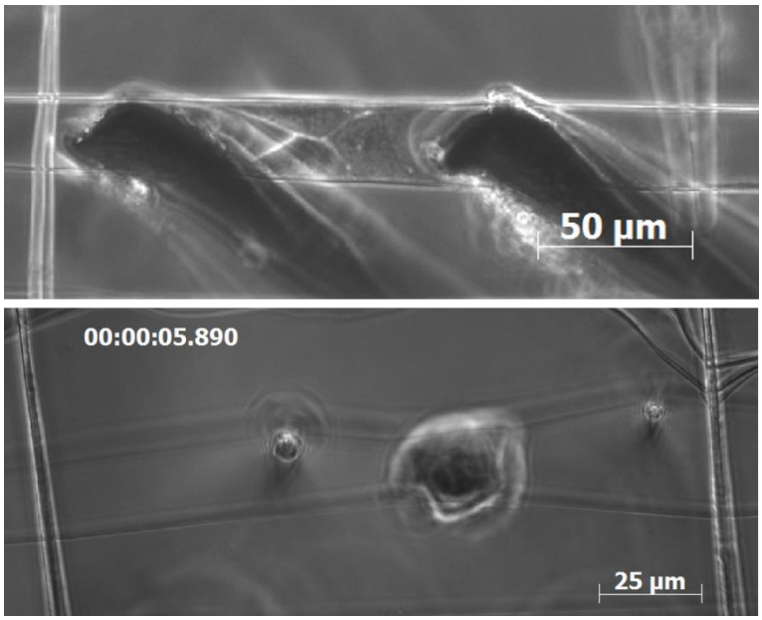

Figure 4-8. Early iterations of the dual probe design which were untenable. Top: wires were both too large to fit between fibers and too easily deformed. Bottom: Annulus design with completely vertical glass probes interfered with light path.

To improve the dual probe system and obtain higher quality images, two micropipette probe tips 1 µm in diameter at the tip were spaced 175 µm apart using an angle design as opposed to the annulus approach. The dual probe holder was designed to permit both glass probes access to the scaffold (while fitting between the microscope condensing lens and the glass dish wall) without interfering with the light path. This required that the holder contain two parts: an 'L' bracket which interfaced directly with the micromanipulator, and an angled connector to which the dual glass probes were attached (**Figure 4-9**). Multiple locations within this system provide degrees of freedom necessary to precisely position the probes: the manipulator itself which enables

25.4 mm of travel along each principle axis with 20 nm pulse resolution, the ‘L’ bracket connection to the manipulator which can be rotated into position before tightening, and the angled connector interface with the ‘L’ bracket which can also be rotated into position.

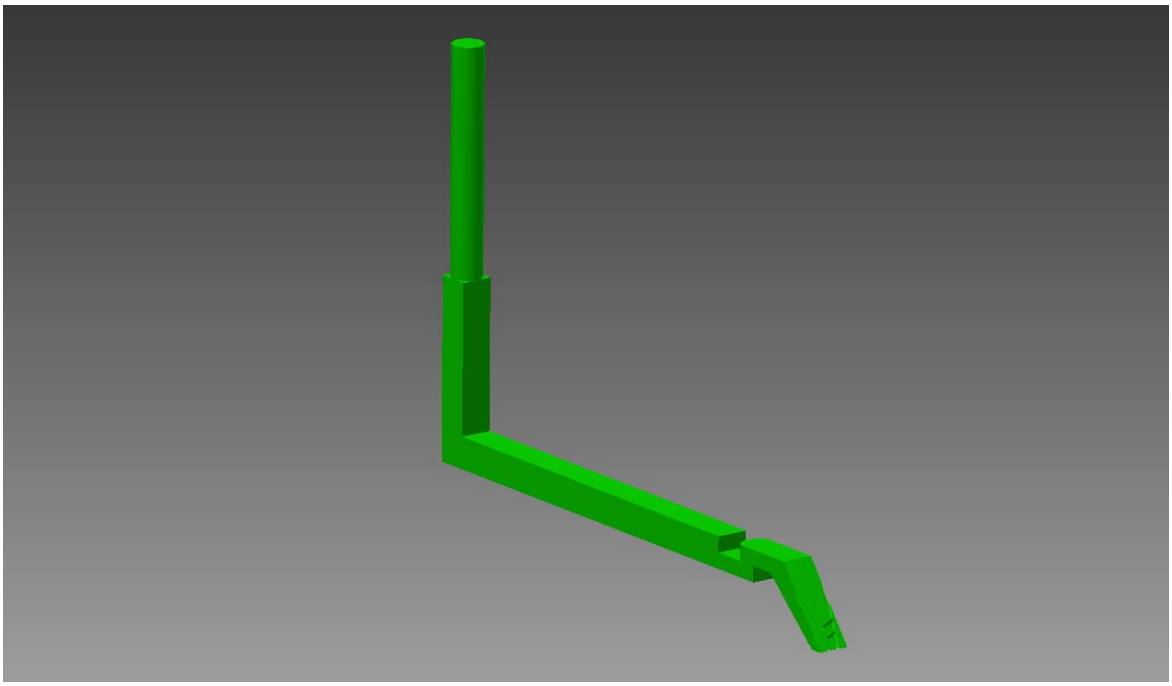

Figure 4-9. CAD drawing of custom-built, 3D printed dual probe holder.

4.1.7 Single Probe System for Biased Force Distribution

The single probe system uses the manufacturer-provided probe holder from Sutter (**Figure 4-10**). There are slots for two glass probes to be held using this system, but they are set parallel to one another and therefore do not come close enough together (< 200 µm) to actuate both sides of a cell on the nanonets.

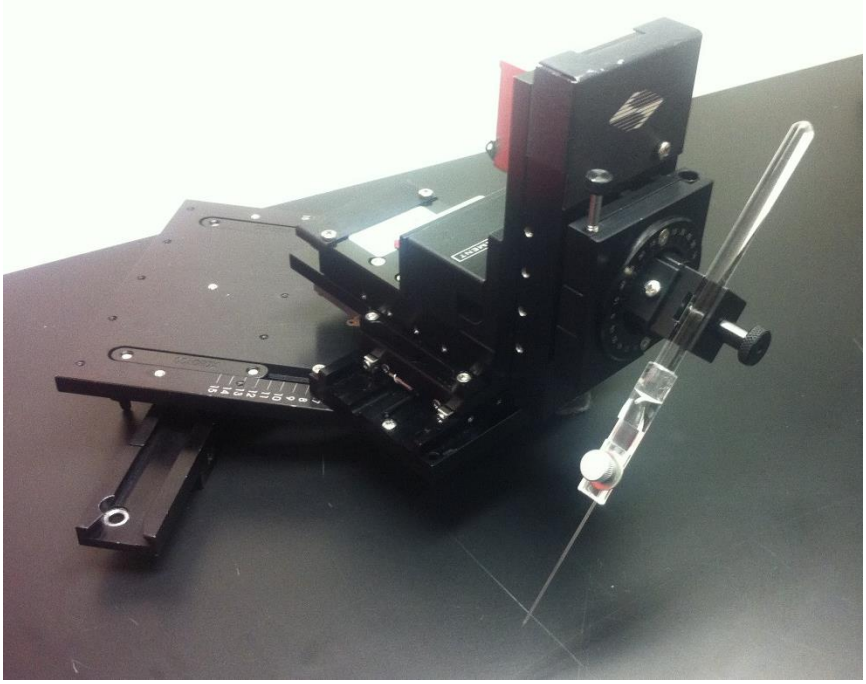

Figure 4-10. Single probe holder from Sutter loaded into the micromanipulator.

4.1.8 Special Cell Culture Considerations

The STEP nanonet system was calibrated around C2C12 mouse pre-myoblast cells as a model cell line, chosen for several reasons. Previous studies from our group demonstrated that C2C12s exhibited good attachment and appreciable migration on the fibers, suggesting that the cells were exerting forces quantifiable by nanonet deflection[5,110]. We also hypothesized that these cells would exert appreciable forces since they are precursors to contractile myotubes. Additionally, C2C12's can differentiate into both myogenic and osteogenic lineages, making them of interest for the lab's future projects[143].

Once seeded, cells attach to the scaffolds in essentially random locations and configurations. Testing must be performed within 24 hours after seeding, however. Over time, stiffness effects cause cells to migrate towards fiber-fiber intersections and change into polygonal morphologies where forces cannot be measured (**Figure 4-11**).

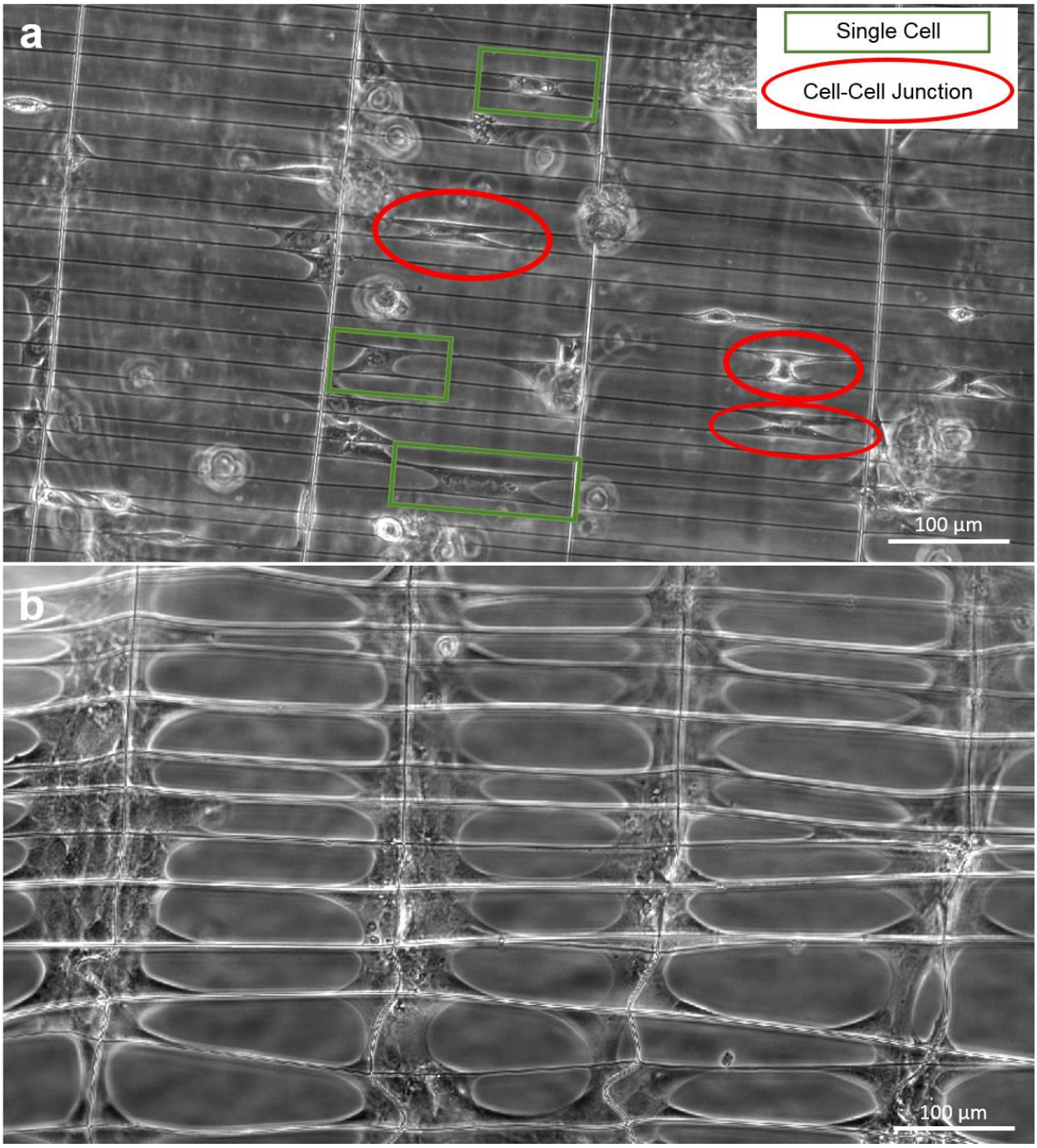

Figure 4-11. Cells seeded onto nanonet scaffolds. (*a*) Initially, cells occupy essentially random locations and form parallel shapes in both single and cell-cell configurations. (*b*) Over time, cells migrate towards regions of higher stiffness (fiber edges) and are not often found at the softer regions (center of the fiber).

4.2 Results

4.2.1 Scaffold Design

Fused scaffold design results in a fibrous scaffold which simultaneously encourages parallel cell configuration and allows for both inside-out observation and outside-in manipulation (**Figure 4-12**). By intentionally creating scaffolds which encourage parallel cell configurations, multiple probe-based perturbations could be carried out on the same scaffold, increasing experimental efficiency.

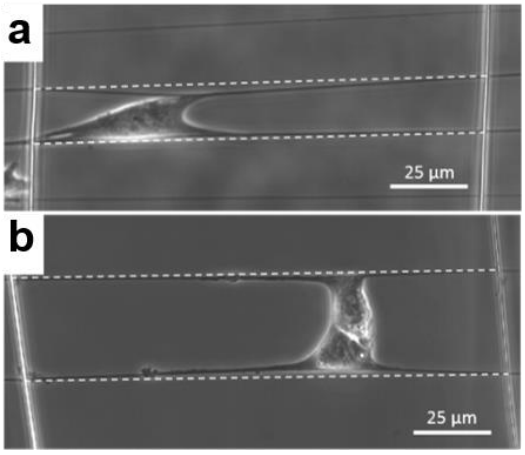

Figure 4-12. (*a*) Fiber suspension causes cells to form parallel shapes between the thin fibers. Forces are exerted during migration and cause fiber deflection (deviation from white dashed line). The force observed at the leading fiber is 57 nN. (*b*) Cell-cell junctions will also form between these fibers (force shown on trailing fiber is 34 nN).

Resolution in the force measurement system is dependent on several parameters, including fiber diameter and length as well as the quality of the images that deflections are measured from. Longer fibers with lower diameters provide greater sensitivity to loads due to decreased structural stiffness. Improvements in resolution are achieved by making a given fiber longer or smaller in diameter, but this is not practical in many applications due to the tendency of cells to plastically deform fibers that are not stiff enough. Resolution can also be improved by acquiring higher-resolution images of fiber deflection during testing. This can be achieved by using higher

magnification objectives (>40x), but this simultaneously requires that the left and right fiber intersections (boundary conditions) are also in view, necessitating shorter fibers which hampers resolution. With these considerations, at 40x magnification the probe is able to comfortably resolve 1 μm deflection distances, and for a structural stiffness at the lower end of fabrication (5 nN/μm), the probe pull system can reasonably be expected to resolve 5 nN forces.

4.2.2 Inside-Out Fiber Deflections Measure Migration Forces

As cells attach, spread, and begin migrating between two parallel nanonet segments, individual fibers deflect (**Figure 4-13** *D(i)*). Deflection can be converted into applied force by assuming the nanofibers behave as beams. Previous work from our lab has demonstrated that cell-fiber adhesions in parallel-shaped cells primarily cluster into two separate locations at the periphery of the cell[5]. Because of this observation, we assume that cells in such a configuration apply a point load at both cell peripheries on the trailing fiber (locations *a* and *b* with associated loads P_a and P_b, assigned such that *a* and its associated load P_a are located nearest to the pinned fiber intersection) (**Figure 4-13** *D(iii)*). We recorded over 50 unperturbed C2C12 cells and their associated IO fiber deflections at *a* and *b* and recorded forces of $P_a = 18.9 \pm 3.1$ nN and $P_b = 20.2 \pm 2.4$ nN (**Figure 4-13** *D(ii)*). By further assuming that these two point loads at their prescribed locations are equivalent to a single point load at an intermediate location, we find that the overall IO cell force equals $P_a + P_b$, or 39.5 ± 4.5 nN. Force distribution within the cell can be described by the ratio P_a/P_b wherein any value over or under 1.0 represents biased distribution. This ratio is found to be 0.94 for the IO case, showing that the forces are essentially equally distributed across the cell, with the slight deviation from 1.0 likely caused by uneven forces required for the cell to migrate in a given direction. Forces were also found to weakly correlate with structural stiffness

(*k*, units: N/m), a trend similar to both micropillars of varying pillar stiffness and flat substrates with tunable modulus of elasticity (*E*, units: N/m^2) [90,144].

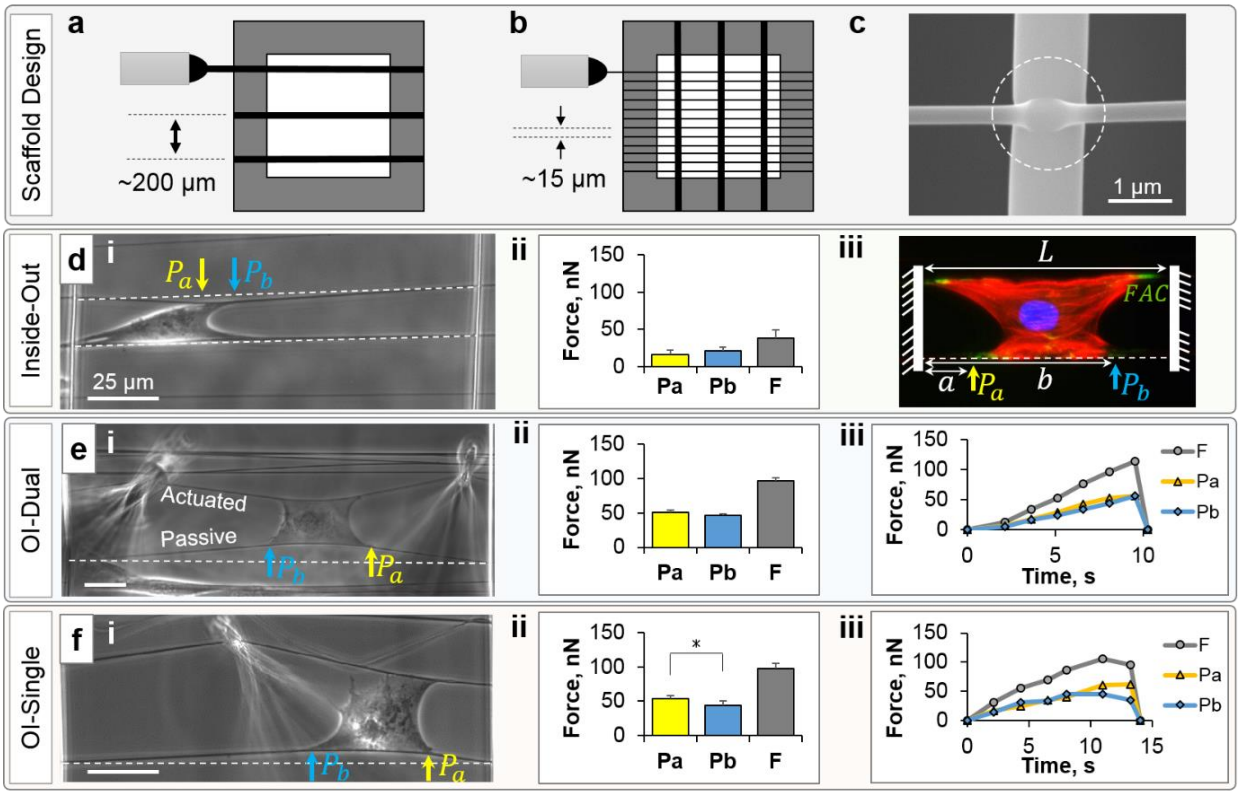

Figure 4-13. Nanonet and probe system use for measuring cell forces. Schematic of thick diameter fibers (~1200 nm) spun with large inter-fiber spacing over a hollowed-out substrate, resulting in suspended fibers. (b) Schematic of thin diameter fibers (~400 nm) spun with smaller spacing perpendicular to the first layer. (c) Fiber intersections are fused together, resulting in clamped boundary conditions, (d) IO force measurement, showing i) representative parallel cell, ii) force distribution (Pa+Pb = F), and iii) schematic of a cell. (e) OI-Dual platform, with i) representative optical image, ii) force distribution, and iii) representative force-time plot. (f) OI-Single platform, with i) representative optical image, ii) force distribution, and iii) representative force-time plot. (Student's t-test, $p<0.05$, N = 242).

4.2.3 Outside-In Perturbation Measures Cell Adhesion Strength

To measure OI cell adhesion forces, a glass micropipette probe system was designed to perturb single parallel-shaped cells via programmable micromanipulated motions. Two different modes of operation were designed to determine the effect of biased loading on cell adhesion: dual probes (*OI-Dual*) positioned on either side of a parallel-shaped cell, actuating the cell evenly (**Figure 4-13** *E(i)*), and a single probe (*OI-Single*) only actuating one side of the cell to induce bias

(**Figure 4-13** *F(i)*). For the dual probe system, two micropipette probe tips 1 μm in diameter at the tip are spaced 175 μm apart and loaded into a 3-axis micromanipulator via a custom-built 3D-printed probe holder. The single probe system requires only one micropipette tip and is loaded into the manipulator via a standard probe holder (Sutter). To determine cell adhesion strength, the cell is stretched to failure by actuating the top fiber (actuated fiber) using pre-programmed manipulator motions and observing the bottom fiber's (passive fiber's) deflection. The cytoskeletal network experiences increasing force as the probe pushes the fiber to greater strains. Eventually, the cell detaches and the passive fiber returns to its original non-deflected state. The maximum force value reached during this test is taken to be the adhesion force of the cell.

At each fiber diameter tested (250, 400, and 800 nm), OI-Dual manipulation results in even force distribution within the cell, with averages of P_a = 54.2 $\pm$ 4.0 nN and P_b = 51.8 $\pm$ 3.7 nN (P_a/P_b = 1.05), giving a total force of 106.1 $\pm$ 7.3 nN that compares favorably to forces obtained through other OI approaches (**Figure 4-13** *E(ii)*)[92,98]. These forces correspond to fiber deflections averaging 3.2% of their span length, falling within the suggested elastic limit for polystyrene nanofibers[140,141]. The force-time plot from a dual probe perturbation typically shows a steady rise in force through time as the cell is stretched while maintaining adhesion integrity followed by a sharp drop as the cell-fiber adhesion fails, representative of the abrupt breaking failure typically observed (**Figure 4-13** *E(iii)*). Although it is not clear at which precise location failure occurs throughout the adhesion's structure (at the integrin-substrate bond, at the integrin-actin bond, etc.), failure was observed to initiate evenly at each side of the cell (*a*: 29%, *b*: 29%, *both simultaneously*: 42% of the time), further suggesting even distribution of forces within the cell

On the other hand, OI-Single manipulation biases forces towards *b* (the probe side of the cell), with averages of P_a = 50.7 $\pm$ 3.5 nN and P_b = 52.9 $\pm$ 4.2 nN (P_a/P_b = 0.95) (**Figure 4-13**

F(ii)). This effect is pronounced on the 800 nm fibers, in which P_a = 80.6 ± 7.2 nN and P_b = 100.6 ± 8.4 nN (P_a/P_b = 0.80). Since the single probe actuates from *b*, that side of the cell experiences greater relative strain compared to the opposite side. The end result is that failure initiation shifts towards *b* as well (*a*: 17%, *b*: 58%, *both simultaneously*: 25% of the time). Force-time plots from OI-Single tests also steadily rise over time, but instead of dropping sharply as seen in cells pulled with dual probes, a peeling-type failure mechanism is seen wherein forces level off before failing (**Figure 4-13** *F(iii)*). Bias appeared to affect forces differently on different diameter fibers. Although not statistically significant, bias slightly *increased* forces on small fibers (250 nm), *did not affect* forces on medium fibers (400 nm), and slightly *decreased* forces on large fibers (800 nm). However, the average total force of 103.6 ± 7.1 nN remained similar to the dual probe system. In other words, instead of affecting the total adhesion strength of the cells, single probe bias allows control over distribution of forces within the cell that ultimately dictate location of the initiation of failure. The ability to control single cell force distribution and detachment location may prove valuable in understanding certain cell events dominated by these behaviors, such as leader cell formation and metastasis from primary tumors or single cell injury models.

4.2.4 Effects of Nanofiber Curvature and Mechanics

We next wanted to determine if substrate curvature and fiber mechanics could explain diameter-dependent bias effects. Substrate curvature is thought to be one of the driving forces behind observed behavioral differences between cells on flat and non-flat substrates. In addition to helping confine and cluster adhesions, substrate curvature is known to align contractile forces[32,145]. Cells which maintain constant surface area of adhesion have been shown to exhibit increased adhesion force when adhesions are clustered via substrate topography[146]. Smaller diameter nanofibers require the cell to spread further and cluster adhesions less densely if they are

to maintain adhesion area, a phenomenon which may cause different adhesion forces on different diameter fibers[147] (

Figure 4-14). We have previously attempted to quantify the degree of focal adhesion wrapping around fibers of different diameter without much experimental success. We first used confocal microscopy (Figure 4-14 *C*) to attempt to visualize the extent of wrapping but quickly found that while the nucleus (*diamond arrow*) and actin (*circle arrow*) positions could be detected, polystyrene fibers (*pointed arrow*) exhibited auto-fluorescence which overpowered the signal emanating from the focal adhesions. Additionally, even without auto-fluorescence, this approach could not achieve z-stack slices thin enough to resolve FAC wrapping. We then decided to pursue transmission electron microscopy (TEM), which necessitated embedding the nanonet construct in epoxy resin and using a microtome to create thin cross-sectional samples (Figure 4-14 *D*). However, even after optimizing the embedding process, it was difficult to locate the nanofibers from the cross-sectional view. We believe that ultimately this technique will allow us to quantify wrapping, but doing so will require fibers that are more closely-spaced and cells that are more confluent to increase likelihood of locating a cell-fiber adhesion interface. This would also shed light on the positioning of the adhesion relative to the z-plane of the cell since it is possible that actin experiences out-of-plane bending around the smaller diameter fibers.

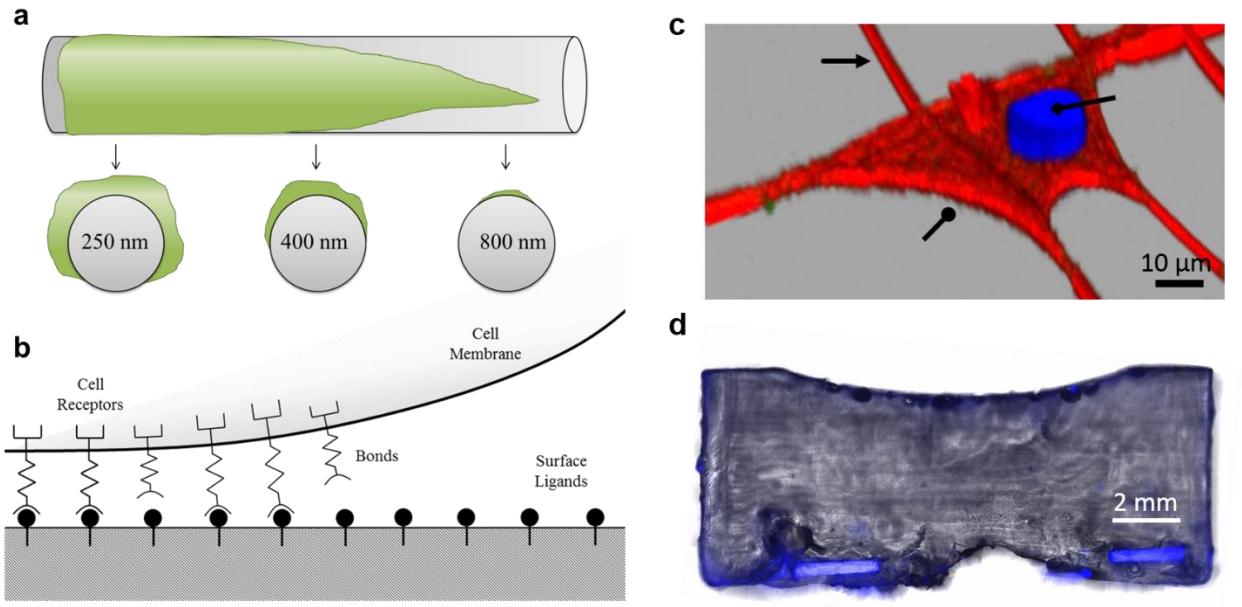

Figure 4-14. Focal adhesion formation on different diameter fibers, potentially contributing to (*a*) different extents of wrapping around the fiber, and (*b*) peeling vs. breaking failure modes, represented here by severance of individual adhesions (which can be modeled as springs) from surface ligands. (*c*) Confocal attempts to resolve FAC wrapping were unsuccessful, as were (*d*) TEM-based approaches, with cross-sectional

Having previously observed cells on smaller diameter fibers to cluster adhesions over a larger distance (presumably due to the reduced available adhesion area per unit fiber length), we hypothesized that curvature-induced adhesion orientation was at least partially responsible for diameter-dependent bias effects[147]. Furthermore, as evidenced by the breaking vs. peeling-type of failure observed, bias may perturb focal adhesions differently on different fiber diameters due to spatial orientation, polarization, and/or structural stiffness effects.

Suspended fibers of a constant diameter and length inherently contain gradients of *structural stiffness* whose value changes depending on the position along the length of the fiber. Since a cell spread on a nanonet segment interacts with a small range of stiffnesses throughout its area of contact with the passive fiber, we took the stiffness of the geometrical center of the cell to be the nominal stiffness value. Because fiber lengths varied little in nanonet manufacturing, fiber diameter heavily influenced stiffness, which ranged from 3 – 45 nN/µm.

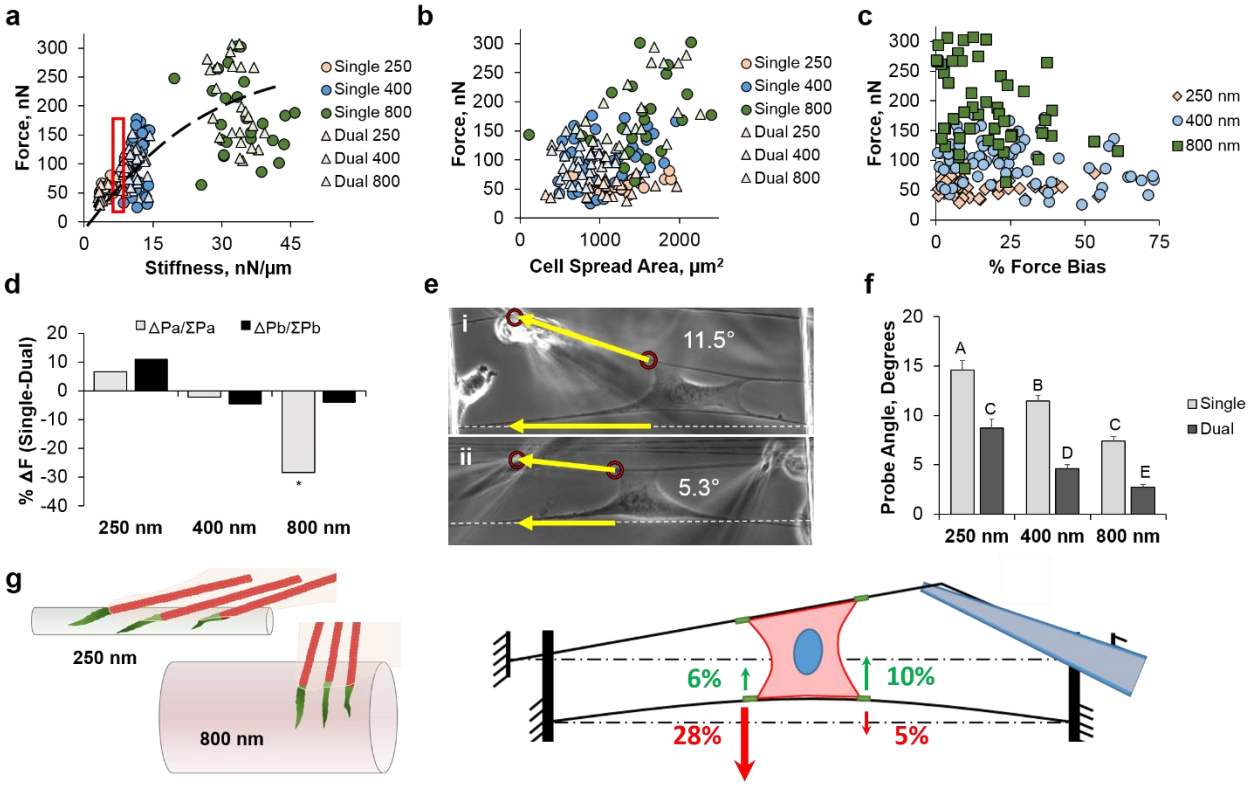

Figure 4-15. Forces for different diameters and probe bias. (*a*) Force as a function of stiffness, with the region of overlapping stiffnesses for different diameters (250 and 400 nm) highlighted (*red box*). (*b*) Force as a function of cell spread area. (*c*) Diameter-dependent force response as a function of amount of bias within the cell. (*d*) Single probe bias (*i*) creates an average probe angle of 11.5° compared to dual probe bias (*ii*) of 5.3°. (*e*) Probe angle as a function of diameter and actuation type. (*f*) Changes in forces at *a* and *b* as a result of using the single probe instead of the dual probe. (*g*) Proposed mechanism for diameter-dependent changes in force distribution, wherein curvature effects of the 250 nm fibers (*green fiber and percentage force increases*) induce axial orientation of individual adhesions compared to vertical orientation on 800 nm fibers (*red fiber and percentage force decreases*). Orientation effects are believed to transition near the 400 nm diameter fibers since no significant changes in force distribution was observed. Despite this observed phenomenon of local changes in force, no significant changes in total adhesion force were observed between the single and dual probe systems ($p<0.05$, $n = 190$).

We found that increasing fiber structural stiffness '*k*' values were associated with increased adhesion forces, where a linear trend was seen for lower stiffnesses that saturated after approximately 35 nN/μm (**Figure 4-15** *A*) [90]. Substrate stiffness is known to affect the exertion of contractile forces by fostering F-actin stress fiber development and focal adhesion growth. However, we believe this effect saturates on nanonets for two reasons: 1) forces eventually become limited by the inability of the cytoskeleton to further develop physically, and 2) higher stiffnesses

inherently deflect to smaller extents, eventually reaching a point where the substrate exhibits no observable deflection despite the cell exerting force. A subset of the force data with common structural stiffness between two fiber diameter groups (250 and 400 nm, **Figure 4-15** *A, red box*) showed statistically insignificant differences in force, confirming a strong correlation between these two parameters (n = 17, data not shown). Cell spread area was also measured at the time of failure and found to be only weakly correlated with total force, in good agreement with findings from other approaches (**Figure 4-15** *B*) [90].

Force distribution within the cell at failure was quantified by differences between P_a and P_b relative to the overall magnitude of the total force $F = P_a + P_b$, such that a percentage force bias may be defined as:

$$\%F_{Bias} = \left(\frac{|P_a - P_b|}{P_a + P_b}\right) * 100 \qquad \text{(Eq. 3)}$$

Plotting percentage force bias against overall adhesion force further suggested that uneven distribution of forces within the cell did not significantly affect overall adhesion force (**Figure 4-15** *C*). Instead, relative to the dual probe, single probe actuation re-distributed forces within the cell, with insignificant increases in force on the 250 nm fibers, no change on the 400 nm fibers, and a significant decrease in force at P_a on the 800 nm fibers (**Figure 4-15** *D*). Probe perturbation also created an angle between the actuated and passive fiber. To quantify this angle, a line was drawn between the probe and outermost adhesion on the actuated fiber (*yellow arrow connecting red circles*) and compared to the original position of the trailing fiber (*yellow arrow overlaying white dashed lines*) using AxioVision software (**Figure 4-15** *E*). OI-dual manipulation resulted in an average angle of 5.3°, whereas the single probe created an average angle of 11.5° between the actuated and passive fibers prior to cell failure (**Figure 4-15** *F*). This angle was largest for the 250 nm diameter fibers and smallest for the 800 nm fibers. For each diameter, the single probe created

a larger angle than the dual probe. The net result is that, when biased, failure initiates more often towards the probe (at 'B'), and is associated with decreased forces on large fibers (**Figure 4-16**).

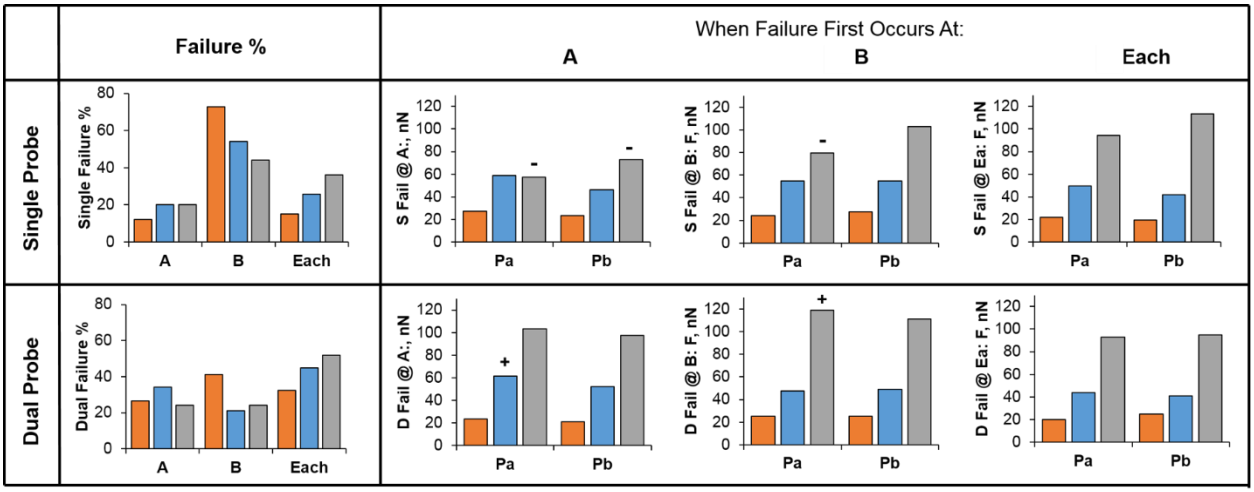

Figure 4-16. Failure occurrence at position A, B, or Each simultaneously, and corresponding force distribution within the cell when it fails at that location for both single and dual probe systems (orange = 250 nm, blue = 400 nm, gray = 800 nm). Plus and minus signs denote statistically significant increases/decreases from the failure 'at Each' case within groups (far right) ($p<0.05$, $n = 190$).

Single probe bias (top row of **Figure 4-16**) is associated with increased failure at location 'B', or nearest the probe. This effect is more dramatic on 250 nm fibers, where failure occurs at 'B' about 75% of the time compared to just over 40% for 800 nm fibers. Furthermore, compared to the simultaneous failure at 'Each', bias causes forces *Pa* and *Pb* to significantly decrease on 800 nm fibers when failure occurs at 'A' and causes *Pa* to decrease when failure occurs at 'B' (as denoted by minus signs over bar chart). On the other hand, dual probe manipulation significantly increases forces in several cases compared to the failure at 'Each' condition, namely *Pa* on 400nm fibers when failure occurs at 'A' and on 800 nm when failure occurs at 'B'. Since the majority of datasets do not result in significant changes from the 'Each' failure cases, we believe there may be some threshold force value that a cell fails at upon reaching.

Interestingly, the percentage of the time that failure occurs at both locations at once ('Each') is highest for 800 nm diameter fibers and lowest for 250 nm fibers. This may provide

support for our proposed model of focal adhesion clustering and orientation driven by curvature effects: if we look specifically at the region of the cell *between the two focal adhesion cluster sites*, 800nm fibers (which have the least curvature) allow some smaller focal adhesions to form along the fiber axis. On the other hand, 250nm fibers have occasionally shown almost exclusive focal adhesion presence at the poles, with few intermediate groups such as those seen on 800 nm fibers (**Figure 4-17**). Since this pattern appears both for the single and dual probe systems, we can infer that it occurs as a result of the fiber's curvature and not due to probe-based actuation.

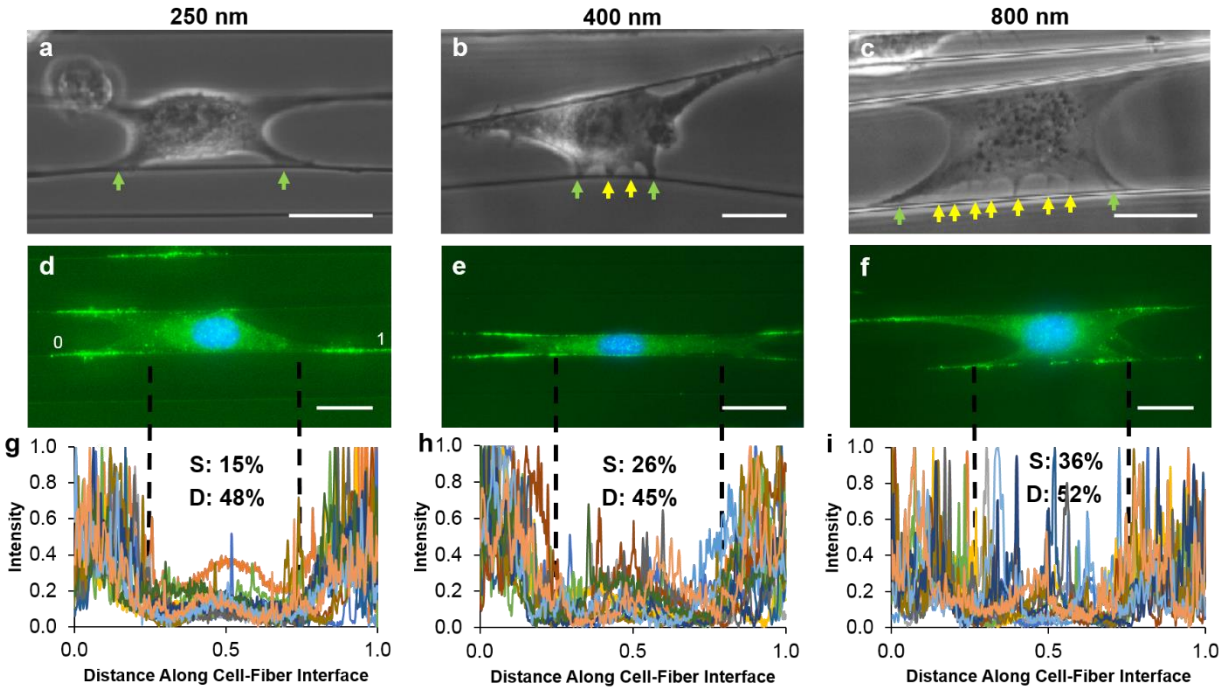

Figure 4-17. Adhesion distribution along the cell-fiber interface as a function of selected diameters. (*a-c*) Optical images cells being pulled on 250, 400, and 800 nm diameter fibers, respectively, with the two primary peripheral clusters (*green arrows*) shown distinctly from intermediary groups (*yellow arrows*), which increase with increasing diameter. (*d-f*) Fluorescence images showing paxillin signal presence along the cell-fiber axis. (*g-i*) Corresponding intensity of the paxillin signal with primary cluster zones separated from intermediary zones by black dashed lines. As fiber diameter increases, signal intensity within this region increases as well (N = 30). The percentage of the time in which probe-induced failure occurs simultaneously at *a* and *b* for single (S) and dual (D) probes is also shown. Scale bar is 25 µm.

Collectively, this data shows that 1) structural stiffness is the primary predictor of force (in the linear region <30 nN/µm), 2) cell spread area is a weak indicator of adhesion force, 3) probe bias externally creates an angle between the actuated and passive fiber in a diameter-dependent

manner, and 4) bias shifts forces within the cell in a diameter-dependent manner without affecting total adhesion force significantly. We propose that curvature effects of the 250 nm fibers induce axial orientation of individual adhesions compared to vertical orientation on 800 nm fibers as evidenced by intermediate adhesions along the fiber (**Figure 4-15** *G*). When biased, axially-oriented adhesions feel force vectors along their orientation (slightly increasing adhesion force), whereas vertically-aligned adhesions become sheared (slightly reducing their adhesion force). Orientation effects are believed to transition near the 400 nm diameter fibers since no significant changes in force distribution were observed at this diameter.

4.2.5 Diameter Mismatch

Nanonets were also constructed with alternating large (L, 800 nm) and small (S, 400 nm) fibers so that cells would attach to mismatched diameters. Cells could arrange themselves in a manner such that the passive fiber was either smaller (PS) or larger (PL), and in each instance the cell could detach from either the small or large fiber when actuated (**Figure 4-18**). Both the OI-Dual and OI-Single modes were used to determine if diameter-dependent bias effects observed previously on constant diameter fibers would be conserved when the cell attached to mismatched diameters.

Cells failed more often on the smaller diameter fiber independent of its positioning relative to the large diameter fiber (**Figure 4-19** *A(i)*). This was true for both OI-Dual (*light shading*) and OI-Single (*dark shading*); however, a slight increase in failure occurrence on the larger diameter fiber was seen when the single probe was used compared to the dual probe (DL = 20%, SL = 29%). Increased tendency to fail on the larger diameter fiber suggests that bias associated with the use of the single probe system either enhanced adhesion force on the smaller diameter fiber, reduced adhesion force on the larger diameter fiber, or provided a combination of both phenomena.

Examination of the forces observed just prior to failure provide support for this to potentially be the case (**Figure 4-19** *A(ii)*).

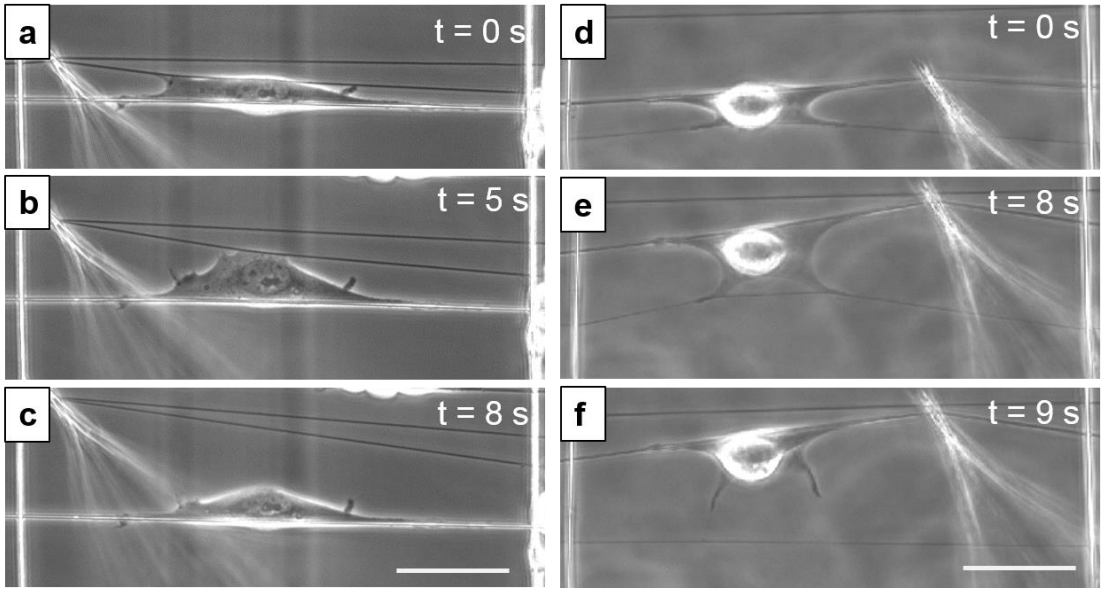

Figure 4-18. Diameter mismatch tests showing (*a-c*) a cell with the trailing fiber being larger, where failure occurs on the small diameter fiber, and (*d-f*) a cell with the trailing fiber being smaller, with failure again occurring on the small diameter fiber. Scale bar 50 µm.

4.2.6 Cell-Cell Junctions

In their native niche, cells form adhesions to an underlying substrate such as the ECM, to other cells which are in close contact in tissue, or to both. Cell-cell junctions allow cells to adhere to one another to maintain proper tissue functionality. The mechanisms behind these types of adhesions are similar but involve different molecules: cell-ECM contacts occur through integrins while cell-cell junctions are associated with cadherins[148]. Physical cues which drive cell-ECM adhesion growth are typically reported to be similar for cell-cell contacts; for instance, enhanced contractility driven by increased substrate stiffness causes stronger cell-cell adhesion[149,150]. In the case of muscle tissue, to which the C2C12s used as a model cell line for the STEP probe system belong, cell-cell junctions allow faster passage of calcium waves which are used to time

contraction, and are precursors to cell-cell fusion and differentiation into myotubes[151,152]. The STEP probe system offers a unique platform to isolate two cells attached to each other and a fiber, meaning that cell-cell junctions and cell-ECM contacts can be evaluated in the same test.

Cell-cell pairs formed spread morphologies similar to those of single cells except with a fusion plane running parallel to the fiber axis. When actuated with the OI-Dual system, cells were pulled evenly on both sides. This was confirmed by circularity analysis of the curvatures between the cell-cell junction and the cell-fiber adhesions located at the top left (TL), top right (TR), bottom left (BL), and bottom right (BR) of the cell-cell pair (**Figure 4-19** *B (i)*). Cell configuration was initially slightly elongated (low circularity) but became more circular throughout the stretch, and did so evenly on each side (**Figure 4-19** *B (iii)*). On the other hand, OI-Single actuation (**Figure 4-19** *B (ii)*) induces uneven cell stretching as evidenced by saturation and eventual decrease in the top right circularity (closest to the probe) (**Figure 4-19** *B (iv)*).

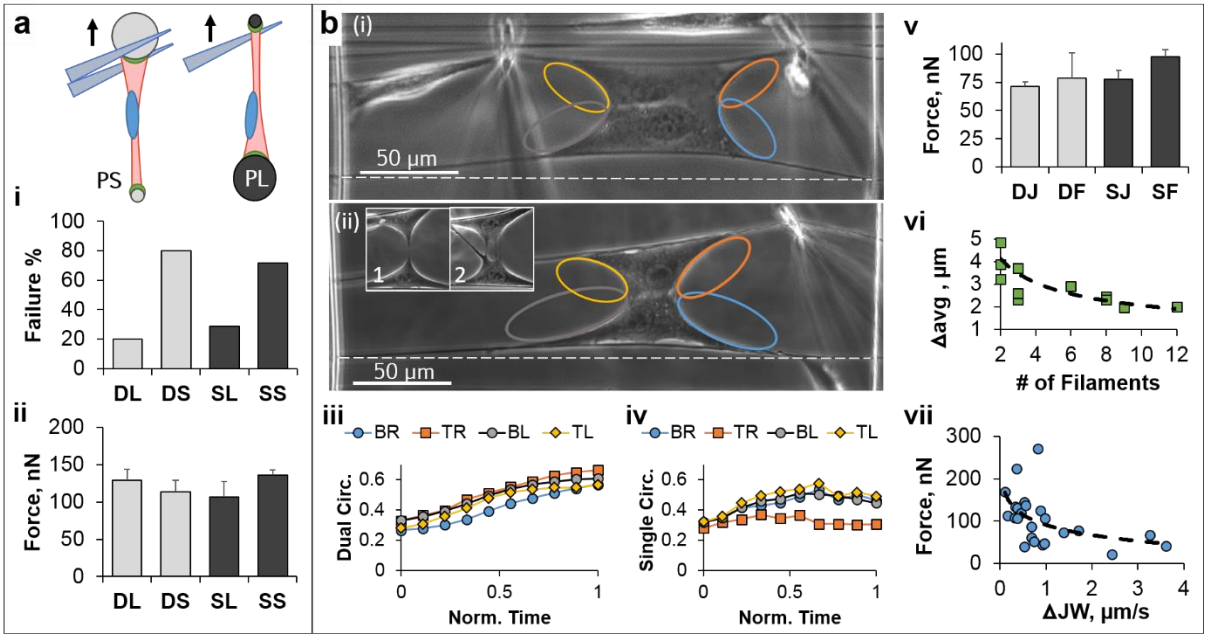

Figure 4-19. (*A*) Mismatched diameter data shows that (i) failure will occur more often on the small fiber for both OI systems, but the single probe slightly increases failure occurrence on the larger diameter fiber, and (ii) forces at failure support previous findings that the single probe results in decreased adhesion strength on large diameters and increased adhesion strength on small diameters (DL = dual large; DS = dual small; SL = single large; SS = single small) (n = 46). (*B*) Cell-cell junction tests are performed with (i) the dual probe and (ii) the single probe and show the effect of bias via circularity measurements, wherein (iii) dual probe causes steady increase in circularity on all four edges of the cell (top left (TL), top right (TR), bottom left (BL), bottom right (BR)), while (iv) single probe causes circularity reduction at the edge closest to the probe (*orange oval*) (n = 37). Forces (v) are higher when failing on fibers (F) compared to cell-cell junctions (J) for both systems (n = 52). (vi) Spacing of the filaments spanning the cell-cell junction (*inset 1 and 2 of (ii)*) correlates with number of filaments seen (n = 11). (vii) Forces decrease when the junction width decreases more rapidly (n = 24). Error bars represent standard error ($p<0.05$).

While failure occurred more often at the junction for both actuation modes (in agreement with other recent studies[149,153]), bias again did not significantly affect total force at detachment (**Figure 4-19** *B (v)*). During failure, long filamentous structures were seen spanning the gap of the junction as it failed. Several groups have shown the formation of these structures, which are composed primarily of actin surrounded by the plasma membrane, during junction formation but have not described its behavior during junction failure[150,154,155]. We noted that as the number of filaments spanning the gap between the two cells increased, the average distance between each filament decreased. A single filament could often be seen holding the entire cell-cell junction together before failure (n = 10). We speculate that this behavior arises from the distribution and

clustering of cadherin throughout the junction[156,157]. Lastly, the junction width often narrowed during the pull (initial width = 18.2 $\pm$ 6.2 μm, width immediately before failure = 7.6 $\pm$ 5.6 μm). The rate at which this process occurred appears to correlate with the force required to break the junction, with faster decreases in cell-cell junction width (ΔJW) associating with reduced forces (**Figure 4-19** *B (vii)*).

4.2.7 Cyclic Data

Bone tissue remodeling (Wolff's Law) and F-actin remodeling in endothelial cytoskeletons from rhythmic pulsatile blood flow demonstrate that inside-out and outside-in forces are both are physiologically relevant[38–40]. Cyclic perturbations simulate these rhythmic pulsatile forces and allow cytoskeletal dynamics to be observed as the cell remodels stress fibers to accommodate loading. A common approach in this regard is to seed cells on large, thin elastic films and apply uniaxial or biaxial stretch on the order of 10-15% amplitude at 0.1 – 1 Hz to the entire film[158,159]. With this technique, it has been found that stress fibers realign perpendicular to the stretch vector, suggesting that the cell rearranges to experience as little strain as possible, and that the degree of reorientation is amplitude and frequency-dependent[41,160]. One proposed mechanism for remodeling is a slip-catch system in which localized bonds between actin bundles and the substrate fail in stages, allowing the filament to reorient[161,162]. At low frequencies/amplitudes, individual actin-substrate bonds become activated, but at high frequencies/amplitudes, the entire stress fiber is stretched, activating all bonds simultaneously. Interestingly, this proposed mechanism depends entirely on interaction of the stress fiber bundles with the substrate – a phenomenon which physically cannot occur in parallel shaped cells on suspended STEP fibers, providing a unique

opportunity to test this proposed mechanism and determine whether remodeling occurs using the probe system.

The cyclic test on STEP fibers is performed by pushing the leading fiber up to a preset sub-failure point, then returning to its original position and repeating this motion continuously. Due to hardware limitations, the maximum programmable frequency is 0.5 Hz, but this lies within the suggested range of remodeling seen on thin films[160]. However, parallel fiber orientation on STEP scaffolds allows very large strain amplitudes to be achieved which might otherwise destroy thin films. For example, a cell was subjected to a 5 μm/s, 0.1 Hz cyclic load of 50% strain amplitude (unstretched = 17 μm, stretched = 26 μm) for 30 minutes, resulting in 150 total cycles applied to the cell. The cell was found to migrate towards the probe location as well as develop more mature adhesions at the periphery of the cell. In addition to observing the cytoskeletal remodeling and slight migration, the total displacement of the probe and trailing fiber were tracked, and it was found that cells remodeled within 10 minutes of cycling and experienced less force as a result (**Figure 4-20**).

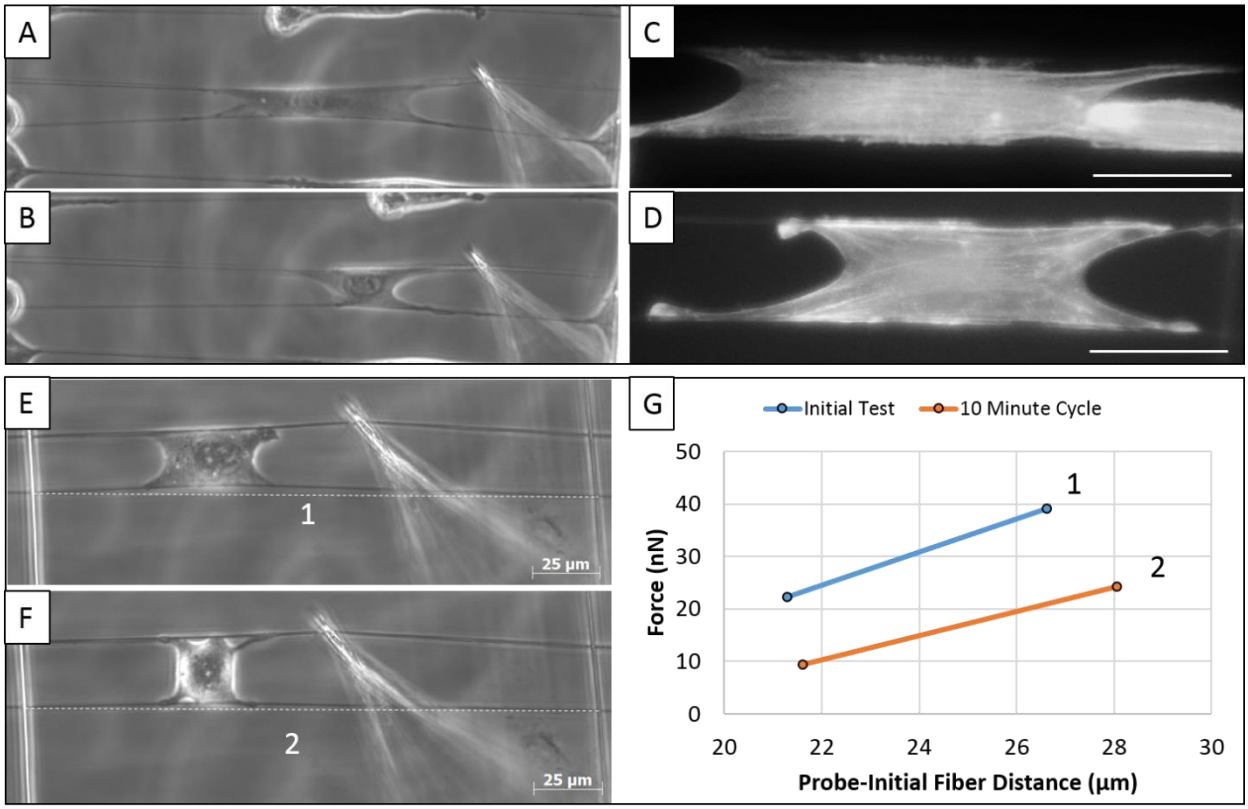

Figure 4-20. Cyclic loading and resulting cytoskeletal rearrangement and force reduction. A) Cell arrangement during initial cycle. B) Cell after 150 cycles has migrated and rearranged its cytoskeleton. C) Different cell without cyclic stretch showing predominately horizontal actin stress fibers. D) Different cell after 13 compressive cycles showing diagonally oriented actin stress fibers. E-G) Different experiment showing cell response to step strains before (E) and after (F) 10 minutes of cycling. G) At both step strains (22 and 27 µm), the initial force is greater than the force after cycling.

To evaluate the STEP probe system for efficacy as a cell remodeling and drug testing platform, we subjected cells to varying degrees of cyclic impulse (at 2 µm/s strain rate) and concentrations of the rho kinase (ROCK)-inhibitor Y27632 as a test case. In uninhibited cells, ROCK pathway activation leads to increased cytoskeletal tension through f-actin stress fiber formation and focal adhesion development, thereby allowing cells to generate contractile forces [30,163]. Y27632 competes with ATP for binding sites on ROCK, preventing this pathway's initiation and resulting in decreased cytoskeletal tension[164,165]. This platform provides an opportunity to evaluate the relative importance of drugs versus cycling strain on cell remodeling. In the 30-minute excitation experiment, cells were stretched either continuously or every two minutes (with 1 or 4

cyclic stretches per two minute period). In addition to control cells (no drug, but all cases of excitation), Y27632 was added at either normal (10 µM)[3,88] or oversaturated (100 µM) [166] concentrations at the start of experimentation to compare the effects of cycling frequency to ROCK-inhibited force evolution (**Figure 4-21**). We found that when the cell was stretched a single time (1x) and then allowed to rest the remainder of the two minutes, force was not significantly reduced (decrease of 7%). However, if the cell was either cycled four times (4x) in that same two minute window (1 minute of perturbation (once every 15 seconds), 1 minute of rest) or continuously perturbed, force significantly decreased (4x = 37% reduction, continuous = 41%). The decreased force reported here due to remodeling occurred in a much quicker timeframe (<30 minutes) than those reported elsewhere (2-4 hours), perhaps due to the larger strain amplitudes used here [160]. Cells treated with 10 µM Y27632 cycled at 1x (38% reduction) followed similar trends to the cyclically-perturbed control cells, and cells treated with 100 µM Y27632 experienced a further reduction in force (57%). However, despite showing relatively similar reductions in force, cyclically-perturbed cells appeared to reach a steady-state force value whereas ROCK-inhibited cells did not. Taken together, this data indicates that although force values are similar, the route (biophysical cytoskeletal remodeling vs. biochemical inhibition of contractility) of achieving force reduction can be different within the cell, and the ability to distinguish between both modes is critical for single cell disease detection.

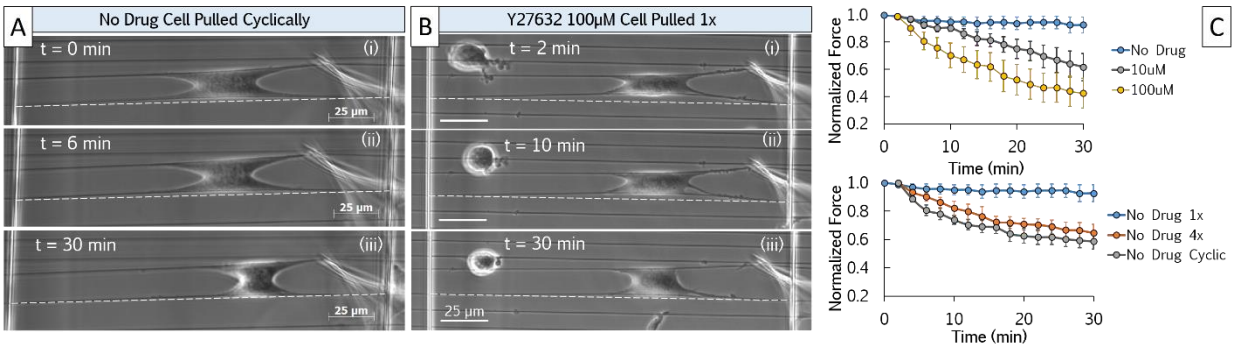

Figure 4-21. Drug testing and cyclic remodeling experimentation on STEP nanonets.

Cytoskeletal remodeling on STEP fibers demonstrates that cells remain able to respond to cyclic perturbations despite lacking underlying substrate to form bonds with actin bundles. Preliminary data indicates that F-actin stress fibers may remodel diagonally as opposed to remaining horizontal (perpendicular), although additional testing is needed to confirm this observation. Some recent work confining cells to different aspect ratios on flat gels (which resemble parallel configurations on STEP fibers) have suggested that initial cytoskeleton configuration (initial fiber separation distance) affects the ability of the stress fibers to perceive directional loading and remodel accordingly, warranting further investigation using the STEP system[167].

4.2.8 Viscoelastic Behavior

As cells experience forces, interactions between cytosol and cytoskeletal structures within their semi-permeable membrane elicit strain-rate dependent reactions[168,169]. Since viscous response can alter apparent forces measured using the STEP probe approach, it is an important parameter to qualitatively describe.

The first test to determine the extent of viscoelasticity on STEP fibers was to perform a phase evaluation at various strain rates. Cells were cyclically stretched and both fiber and probe displacement were tracked for strain rates ranging from 1 – 30 μm/s. Plotting the displacements together reveals that viscoelastic effects appear at low strain rates (**Figure 4-22**).

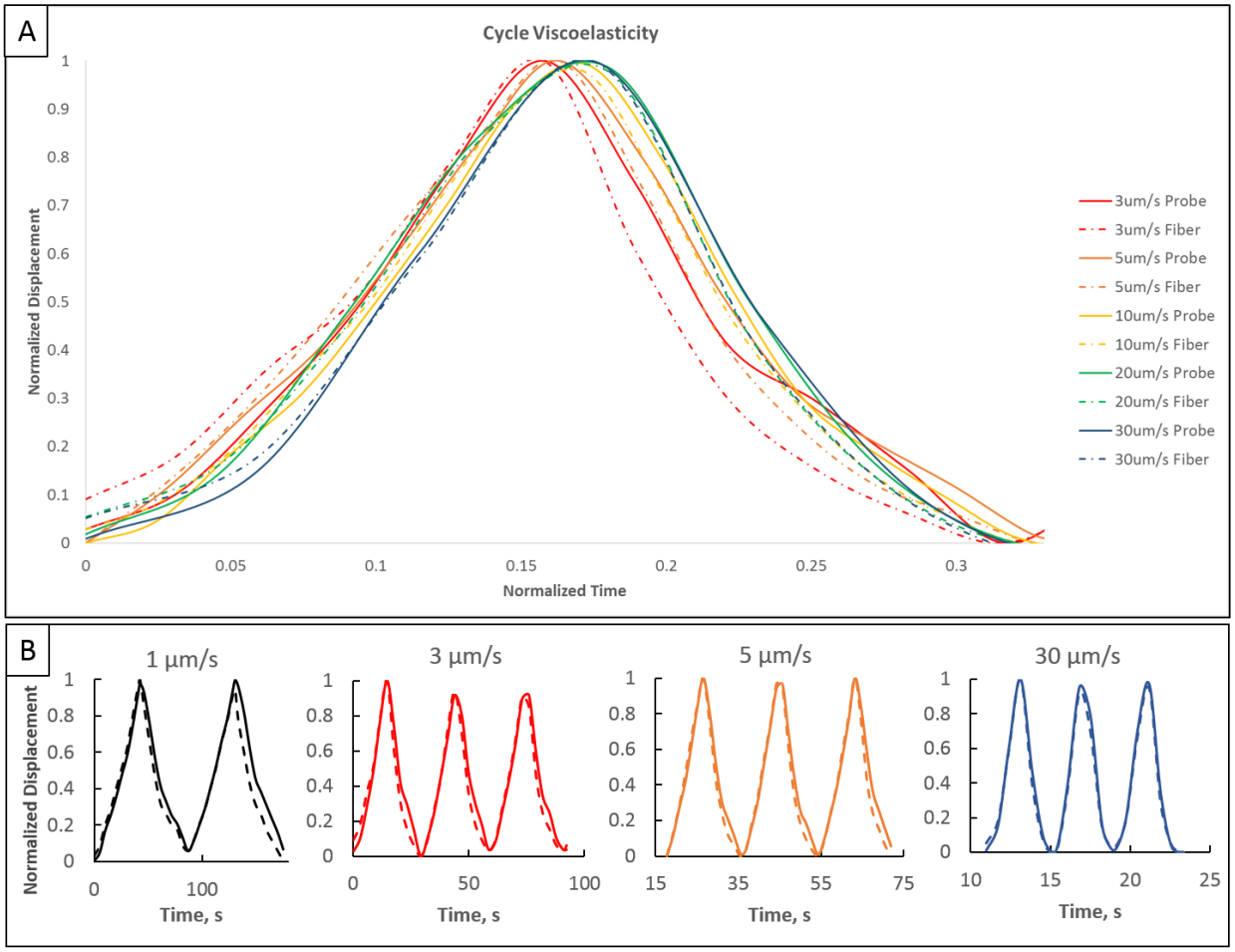

Figure 4-22. Cycle viscoelasticity as a function of strain rate. Data shows that probe lag effects are dramatic at low strain rates compared to high strain rates.

The probe and trailing fiber are in-phase during active pull (positive slope). Probe lag, as demonstrated by the solid lines following after the dashed lines, is only observed when the probe returns to zero deflection (negative slope) for low strain rate cases. This is indicative of viscoelastic behavior: a purely elastic interaction would yield in-phase displacements throughout testing, yet instead an out-of-phase phenomenon is observed during relaxation. The cell loses elasticity (becomes softer) when the active component is removed during relaxation, allowing the fiber to more quickly return to zero than the probe. Probe lag effects are significantly diminished upon

reaching the 3-5 μm/s strain rate threshold, and are not detectable at rates over 30 μm/s. This suggests that cells pulled near the threshold strain rate behave purely elastically on STEP fibers.

Additional experimental evidence to support this transitional strain rate arrives through stress relaxation tests. A viscoelastic body subject to an instantaneous and constant step displacement/strain relaxes in force/stress over time. Details about the relaxation curve can provide insights into the relaxation time of the viscous body. Often, data from these tests are fitted into viscoelastic models which help predict the behavior of future specimens if structural modifications are made. Whether Maxwell or Voigt elements are used in such models, stress relaxation tests allow one to generate the three descriptive constants k_1, k_2, and η (two springs and one dashpot) which comprise the models. As displacement is held constant, the force relaxation is described by[170]:

$$F = \left(\frac{F_0}{k_1+k_2}\right) k_2 + k_1 e^{-\frac{k_1 t}{\eta}} \qquad \text{(Eq. 4)}$$

Where F_0 is the initial force and t is time. The advantage of fitting data to such models is that one can distinguish rate-dependent mechanical response of the cell from rate-independent ones, yet the difficulty has historically emanated from drawing biological significance from these three parameters. Recently, Moreo et al used a Maxwell element in parallel with a substrate elasticity spring to describe mechanosensory response to varying substrate stiffnesses[171]. In this model, three cytoskeletal elements were assumed to play a significant role in cell mechanics: microtubules, actin, and acto-myosin contractions. Stemming from Ingber's concept of tensegrity, microtubules are assumed to be compressional elements with actin primarily the tensile element[172]. Microtubule-based disruptions would therefore be rate-independent and suitable for the k_1 assignment. Likewise, since actin is bundled to the acto-myosin contractile unit it is assignmed to k_2 (which is

in series with η). Lastly, having acto-myosin contraction represent the cell viscosity parameter captures active cell adjustments to external forces. Here, stress relaxation tests were performed and fitted to the standard linear solid (SLS) model (**Figure 4-23**).

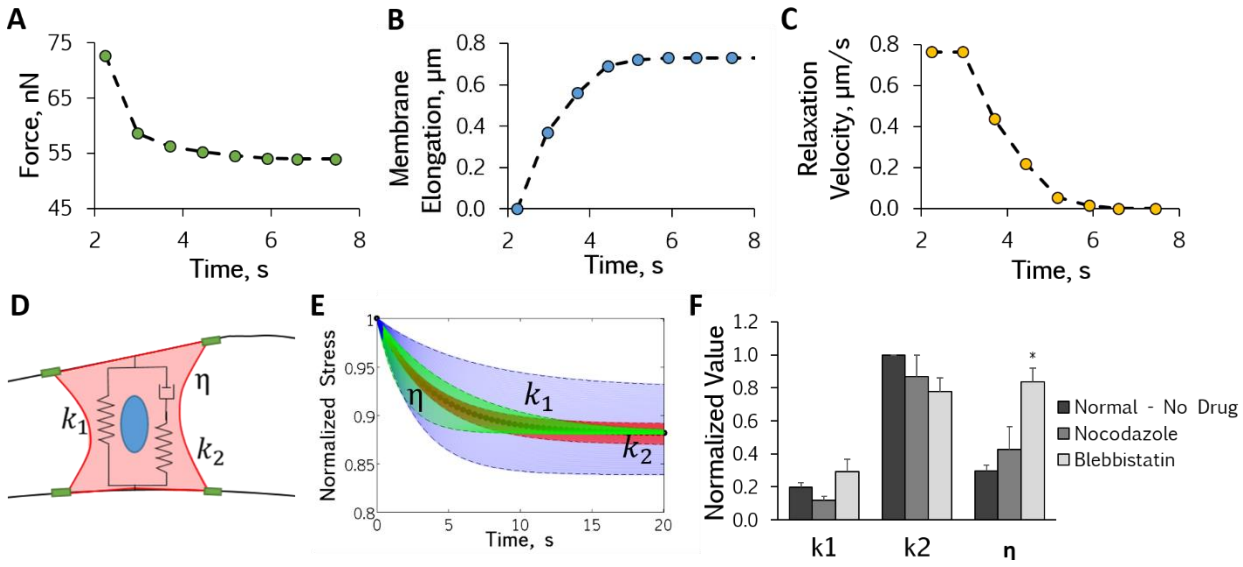

Figure 4-23. Stress relaxation test and associated SLS modeling. Cell elongation after step-strain is applied and held constant. B) Membrane velocity during the test. C) Schematic of the 3-element SLS model. D) Force reduction over time with a fit line resulting from SLS modeling. E) SLS parametric modeling showing dependence on k_1 (blue), k_2 (red), and η (green) with shaded regions representing standard deviation. F) Load shifting as a result of cytoskeleton knockdown drugs nocodazole (microtubules) and blebbistatin (myosin) ($p<0.05$, N = 26).

As demonstrated in **Figure 4-23** *A*, cells that experience a step strain exhibit viscoelasticity and require several seconds (>5) to fully relax. **Figure 4-23** *B* shows that peak membrane velocities during these tests were found to be on the order of 1 µm/s, which partially explains probe lag observed near this strain rate. The three-element SLS model shown schematically in **Figure 4-23** *C* was used to fit force/stress relaxation data as shown by the dashed line in **Figure 4-23** *D*. Modeling results showed that the cell could be expected to relax anywhere from 85 – 95% of its original force/stress value, with the major contribution stemming from k_1 (shown in blue in **Figure 4-23** *E*). The predicted assignment of microtubules, actin, and acto-myosin contractility to the three elements in the SLS model by Moreo et al. presents a testable case with the use of selective

knockout agents. Microtubules can be depolymerized with 10 μM nocodazole administration[173]. The acto-myosin contractile element of the cell is disrupted with 50 μM blebbistatin, which interferes with myosin-II[174]. Lastly, actin can be depolymerized with cytochalasin D, but doing so would interfere with the acto-myosin component as well so this agent was not used[115]. Normalized values for k_1, k_2, and η plotted in **Figure 4-23** *F* show that load shifting from k_2 to η is seen for both drugs, meaning the 1:1 correlation of these parameters to biological components is likely an oversimplification. Collectively, data from these two sets of experiments demonstrate that cells pulled at or higher than 3 μm/s will not have major viscous contribution, and the SLS model is unable to infer the biological implications of these findings.

4.3 Summary and Conclusions

In this work we have developed a nanofiber-based force measurement system capable of capturing single-cell IO migration forces and OI adhesion forces in the absence and presence of bias. We also report the effect of bias on force modulation at different fiber diameters and confirm with diameter mismatch studies. Cyclic loading, cell-cell adhesion, and viscoelastic phenomenon are also explored. Nanonet force scaffolds use suspended and aligned nanofibers to investigate single-cell mechanics on ECM-like substrates and represent the first fiber-based substrate able to capture both IO and OI modes. These new tools in understanding mechanical interactions between cells and nanofibers will allow us to postulate questions regarding onset, progression, and eventual treatment of disease at the single-cell level. Knowledge gained from these experiments will enable implementation of substrate design considerations for finer control over physiological processes that are driven by mechanical cell-fiber interactions. In the future we anticipate combining these tools with chemical stimuli to develop *in vitro* platforms that measure cell response to comprehensive physiochemical cues.

5. SYSTEM APPLICATION: AORTIC ANEURYSM

5.1 Introduction

5.1.1 Introduction to Aortic Aneurysm

Aortic aneurysm is defined as gradual atypical swelling of the aorta which increases risk of sudden tissue dissection[175]. The aorta is the primary blood vessel exiting the heart which carries oxygenated arterial blood to meet systemic metabolic demands. Upon leaving the heart, the ascending aorta branches into several vessels which supply the heart tissue, head, and arms. The aorta then descends into the abdominal cavity, branching off to supply the internal organs and legs. Aneurysm results from progressive swelling of the walls of the aorta, particularly due to weakening of the elastic fibers and de-cellularization of the tunica media (**Figure 5-1**). Risk factors known to influence disease progression share commonalities with other cardiovascular diseases, specifically including hypertension and genetic predisposition[176].

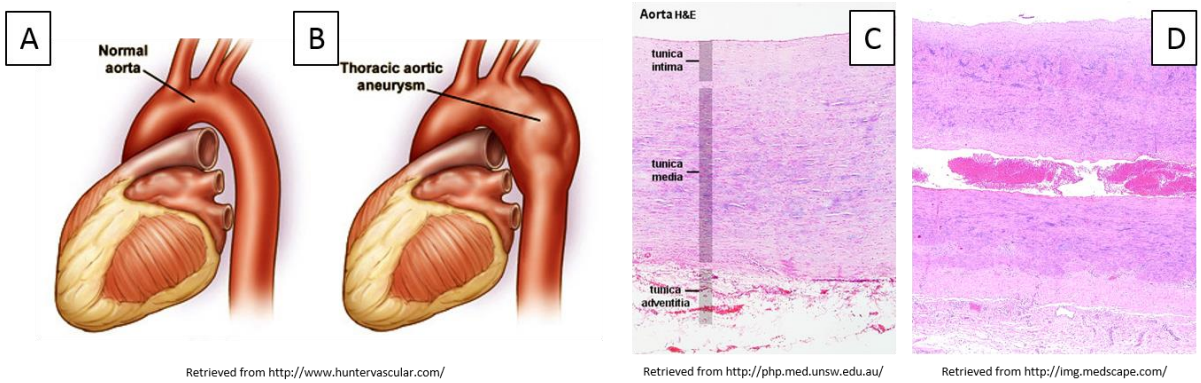

Figure 5-1. Aorta anatomy and thoracic aneurysm presentation. A) Normal aorta. B) Aorta showing thoracic aortic aneurysm (TAA). C) Normal histology with no gaps between layers. D) Histology of aneurysm showing large separation in tunica media.

The blood vessel is built to accommodate highly variable fluid dynamics associated with a spectrum of cardiac output. There are three layers visible by histology: the tunica intima (internal wall), the tunica media (middle), and the tunica adventitia (external wall). As aneurysm

progression weakens the vessel walls, the risk of dissection, or splitting of the vessel into two separate structures, significantly increases. As can be seen in histology images, dissection results from small intimal tears which allow blood to flow into the weaker tunica media and split it more and more with each heartbeat. The vessel then propagates along this axis until the vessel bursts, leaking blood into the thoracic cavity and causing pain which radiates in the chest and back[177]. Prognosis of patients with dissection involves very low survival rate (~10%)[178]. Clinical diagnoses consist of measuring the maximum diameter of the aorta with CT and recommending intervention upon reaching 50-55mm, yet due to the asymptomatic nature of the disease prior to rupture, many at-risk individuals are not screened[179,180].

5.1.2 Current Research Thrusts

Although vascular repair remains the only surgical intervention available to patients, advances in the development of platforms capable of unveiling tissue-level, cell-level, and molecular-level mechanisms behind aortic aneurysms may improve outlook of the disease and options for treatment in the future[181,182]. To this end, research efforts have focused on understanding the changes in mechanical properties of non-healthy tissue. Vorp et al. have shown through tissue tensile tests that aneurysm causes tissue to become less elastic and fail at lower tensile strengths[183]. Computational models have been created which suggest through fluid dynamics simulations that wall stress is a more accurate predictor of dissection risk than vessel diameter[178,184]. Premature degradation of the ECM has also been a target of several investigations: doxycycline has been used as an inhibitor of matrix degradation to prevent aneurysm formation in rats[185]. Lastly, genetic evaluations have supposed that aberrations in the contractile mechanics of smooth muscle cells contribute to the progression of the disease[186]. It is within this arena that the STEP probe platform is well-suited to investigate single aortic smooth muscle cell biophysics.

Our overarching goal with this part of the work, therefore, is to measure strength of cells from patients with varying stages of the disease to determine if mechanical differences exist and can be detected at the single-cell level. To the best of our knowledge, no fiber-based force measurement platform has been used to quantify aortic smooth muscle cell forces from patients with varying disease states. It is possible that disease progression alters matrix composition and/or alignment *in vivo*, factors that the nanonet system can isolate in the future as well. These studies represent some of the first investigations into cell-matrix interactions in aneurysmal mechanobiology and will allow us to examine how physical factors drive aneurysm initiation and progression at the single-cell level.

5.2 Materials and Methods

5.2.1 Primary Cell Culture

The cells used in this study were obtained and gifted from a collaboration with the Phillippi lab at the University of Pittsburgh Medical Center (UPMC). Primary aortic smooth muscle cells were harvested from patients with varying stages of aortic aneurysm progression as defined by clinically-diagnosed aorta diameter ($\leq$ 42 mm = non-aneurysmal, > 42 mm = aneurysmal). In addition, cells from patients with congenital bicuspid aortic valve (BAV) were examined to determine if such cells' forces were significantly different from patients with tricuspid valve. These BAV cells could also come from source tissue that is either aneurysmal or non-aneurysmal based on aorta diameter. Altogether, four classifications of cells were investigated and grouped by number: 1) non-aneurysmal, 2) non-aneurysmal BAV, 2A) aneurysmal BAV, and 3) aneurysmal.

Cells were seeded onto STEP force scaffolds in the same manner as before. Culture media used was smooth muscle cell growth medium (Cell Applications), which included 10% FBS and

1% penicillin/streptomycin supplementation. Standard tensile perturbations were carried out to determine cell adhesion force, strain, and elongation at failure. Experimentation and data analysis was carried out in the same manner as detailed before.

5.2.2 α-Actinin Transfection

Contribution of cell adhesion strength from α-actinin, an actin bundling protein, was examined via transfection studies. Two conditions were examined: a GFP-reporter used to allow green fluorescence of normal α-actinin presence and location when attached to fibers, and a dominant negative mutant GFP-reporter used to replace functioning α-actinin proteins with non-functioning substitutes. Transfections were carried out by seeding cells on plastic-bottom 6-well dishes in antibiotic-free DMEM medium overnight. Cells were then washed in Opti-Mem medium and then incubated at 37°C in 1 mL Opti-Mem per well while transfection reagents were prepared. Two DNA constructs were used: α-actinin-GFP (wild-type) and ROD-α-actinin-GFP (dominant negative mutant). For each well used, 250 µL Opti-Mem was mixed with 5 µL DNA construct in micro-centrifuge tubes by flicking (solution A). Separately, 250 µL Opti-Mem was mixed with 10 µL Lipofectamine transfection reagent by flicking (solution B). The two solutions were then combined and mixed by inversion/flicking and incubated at room temperature for one hour to create the transfection solution. The solution was then added to the well plates dropwise and incubated for 4 hours at 37°C. Afterwards, medium was replenished (2x serum and antibiotics) and incubated overnight. Transfection was confirmed by GFP presence.

5.2.3 Scaffold Design and Probe Use

Outside-in probe experiments were performed primarily with the dual probe system. Having established the role that bias plays in cell forces from the C2C12 study, it was decided to reduce bias effects by keeping fiber diameter constant at 400 nm.

5.3 Results and Discussion

5.3.1 Inside-Out Forces

Single cell inside-out force generation was evaluated by observing fiber deflection as cells migrated along the nanofiber segments (**Figure 5-2**). Patients exhibited different forces on the scaffolds (range from 30-80 nN), and these differences were not due to fiber effects as diameter and stiffness were kept within a narrow range (400nm, 9-13 nN/μm) among all patients tested.

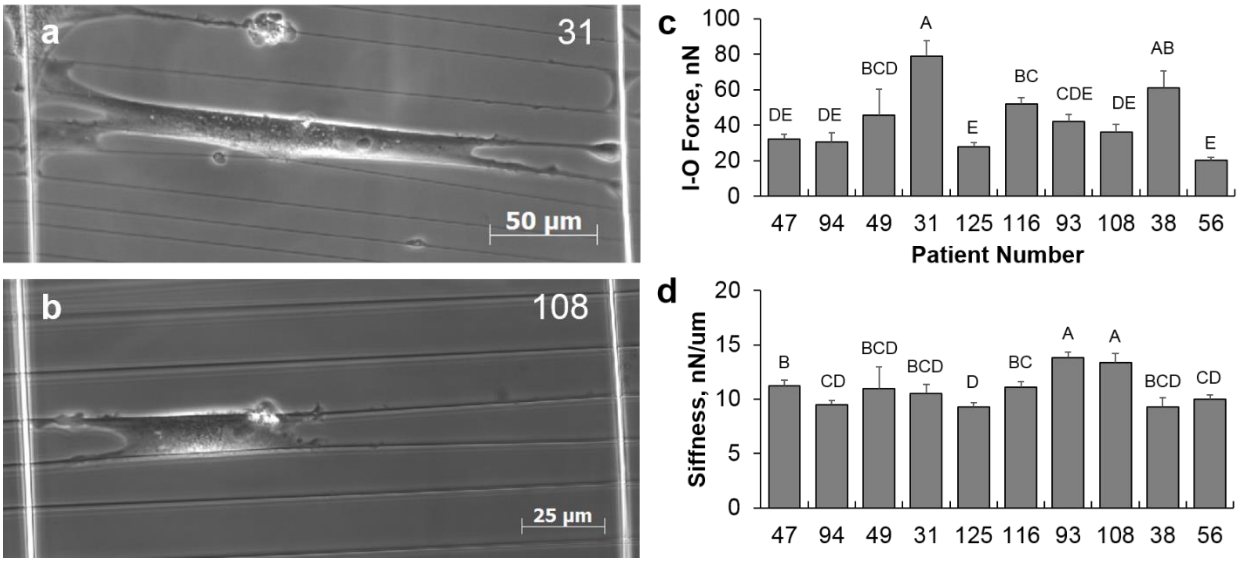

Figure 5-2. Aortic smooth muscle cell inside-out forces on nanonets. (*a*) Representative optical image from patient #31. (*b*) Representative optical image from patient #108. (*c*) Summary of inside out force data for each patient tested, showing a range of forces from 30-80 nN. (*d*) Fiber stiffnesses of the scaffolds for each patient. Values not connected by same letter are statistically different (student's t-test, $p<0.05$, $n = 132$).

One difference in this study compared to the C2C12 study is variation among different patient's cells. Patients varied in age (range 39 – 61 years) and gender, and presumably height and weight (information not provided). We noticed differences in cell size upon testing: for example, patient #31 had an average cell spread area of over 4,004 μm^2 compared patient #34 which spread

to 1,395 μm^2. Testing multiple patients per disease state helps account for patient-to-patient variability such as this. When grouped by disease condition, non-aneurysmal cells exert the highest inside-out force compared to the other disease states (**Figure 5-3**). Interestingly, aneurysmal cells exerted lower forces than non-aneurysmal cells, but this pattern was reversed in BAV patients' cells.

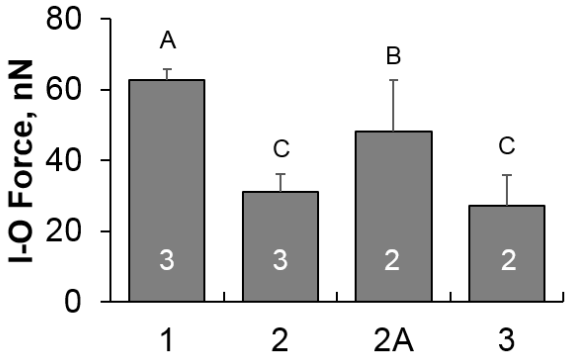

Figure 5-3. Inside-out forces grouped by disease state. Number of patients tested per group is overlaid in white. ($p<0.05$, N = 132).

5.3.2 Outside-In Forces

In the early stages of the single probe system development, we observed changes in cell behavior among non-aneurysmal and aneurysmal aortic smooth muscle cells. Non-aneurysmal cells displayed higher force, strain, and elongation at failure than the aneurysmal cells, demonstrating an immense capability of accommodating external stretch. We observed an average adhesion force of 91 nN and a strain of 350% (75 μm elongation) upon failure (**Figure 5-4**). Aneurysmal cells reduced adhesion force by 5%, but displayed a 60% decrease in strain and 75% decrease in elongation compared to non-aneurysmal cells. Maintenance of adhesion force with reduced stretch during perturbation is indicative of increased elastic modulus (or altered viscoelastic behavior) in the aneurysmal cell population. This corroborates tissue-level data gathered by Vorp et al. who showed that aneurysmal aortic tissue had a 30% decrease in tensile

strength and a 60% increase in tissue stiffness over healthy tissue[183]. BAV cells were not investigated in this early study.

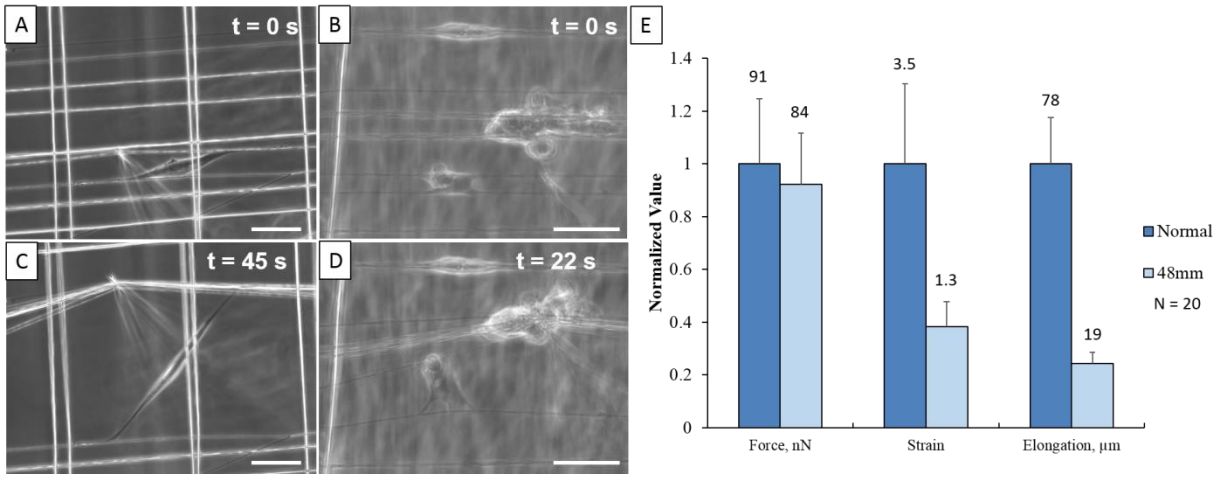

Figure 5-4. Outside-in perturbations of aortic smooth muscle cells from a non-aneurysmal patient compared to an aneurysmal patient show a decrease in mechanical performance in the aneurysmal cells. A) Normal cell prior to stretch. B) 48mm cell prior to stretch. C) Normal cell just prior to failure. D) 48mm just prior to failure. E) Comparison of adhesion force, strain, and elongation between the cell types. N = 20. Scale bar 25 µm.

We first wanted determine if these findings were conserved with the dual probe system. Since 400 nm fibers were used in the single probe study, we expected similar behaviors when using the dual probe system given that no significant changes in total adhesion force were observed in the C2C12 study. In addition, the dual probe study was expanded to incorporate BAV cells of both aneurysmal and non-aneurysmal diameter. The four groups examined were therefore non-aneurysmal cells harvested either from organ donors or heart transplant patients (group 1), cells from patients with BAV of non-aneurysmal aorta diameters (group 2), cells from patients with BAV and associated aneurysmal aorta diameters (group 2A), and cells from patients without BAV but with aneurysmal aorta diameters (group 3). Cells from each group were seeded on scaffolds and pulled with the dual probe system, then analyzed for force, strain, and elongation.

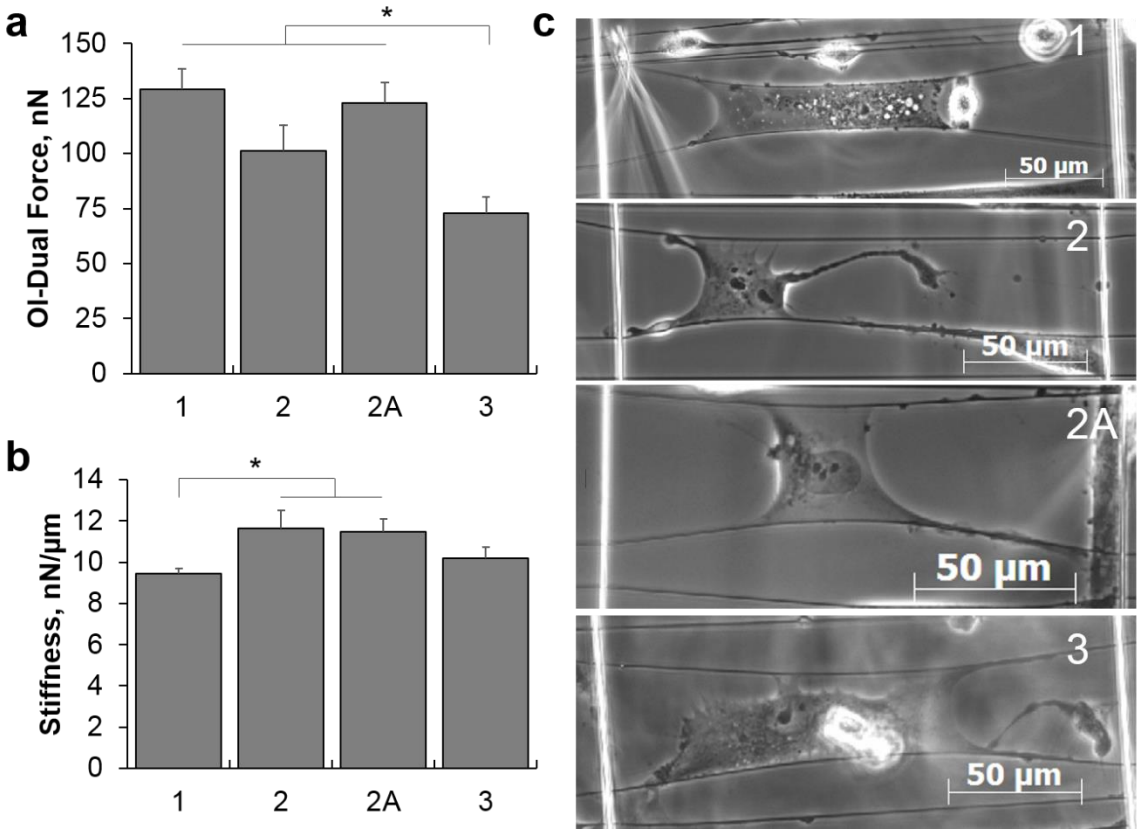

Figure 5-5. OI-Dual (*a*) force and (*b*) stiffness for aortic smooth muscle cells of patients with varying disease states. Optical images from the groups are shown in (*c*). ($p<0.05$, n = 54)

As before, outside-in adhesion forces were significantly higher than inside-out forces for each cell type (**Figure 5-5**). Forces from groups 1, 2, and 2A were statistically similar, but the aneurysmal cells from group 3 exhibited reduced adhesion force, in agreement with our previous findings. Structural stiffness was not responsible for the decrease in force as the fibers in group 3 were statistically similar to the other groups. Non-aneurysmal cells were also observed to elongate (and strain) more than other groups, albeit with lower magnitudes than the previous single probe study (**Figure 5-6**).

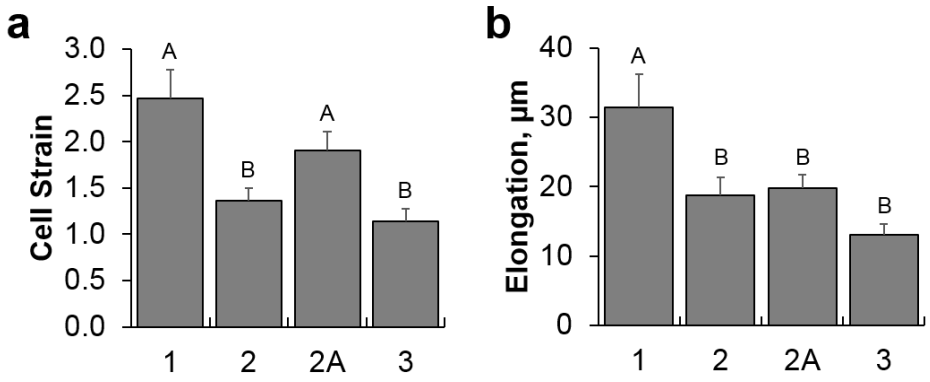

Figure 5-6. (*a*) Cell strain and (*b*) elongation for each disease state. Non-aneurysmal cells are able to accommodate loads by elongating further prior to failing ($p<0.05$, $n = 54$).

Collectively, the outside-in study demonstrates that non-aneurysmal aortic smooth muscle cells exhibit the highest adhesion force, strain, and elongation of the four groups tested. Both BAV groups exhibited similar adhesion force but were not able to elongate to the extent of non-aneurysmal cells. Aneurysmal BAV cells exhibited a higher average force and strain than non-aneurysmal BAV cells, a pattern which is conserved from inside-out data.

5.3.3 Contribution of Strength from α-Actinin

The cytoskeleton is partly comprised of actin stress fiber bundles which are anchored by FACs at each end. Adhesion dynamics are dependent on the cell's ability to probe the mechanics of its substrate through tensional loading[187]. To apply this tensional force, myosin motor proteins contract against the actin network, and as contractile forces grow stronger, scaffolding proteins are recruited to help stabilize the adhesion[188]. One of these bundling proteins called α-actinin binds multiple actin filaments together near the adhesion site to help form stress fibers which enable the cell to apply greater forces[114,188]. α-Actinin is found prominently in muscle cells, perhaps due to their role in generating forces for contraction, and is considered a phenotypic marker in differentiation studies[189]. Interestingly, it has been found that α-actinin expression is significantly

reduced (~85% compared to normal) in aneurysm tissue[190]. This reduction may partially explain the supposed weakened contractile state of aneurysmal cells.

To further investigate this behavior and its contribution to single-cell mechanics, transiently GFP-transfected α-actinin positive and dominant negative mutant cells were tested with the STEP probe system. We first carried out the transfections and verified GFP fluorescence on flat glass substrates (**Figure 5-7**).

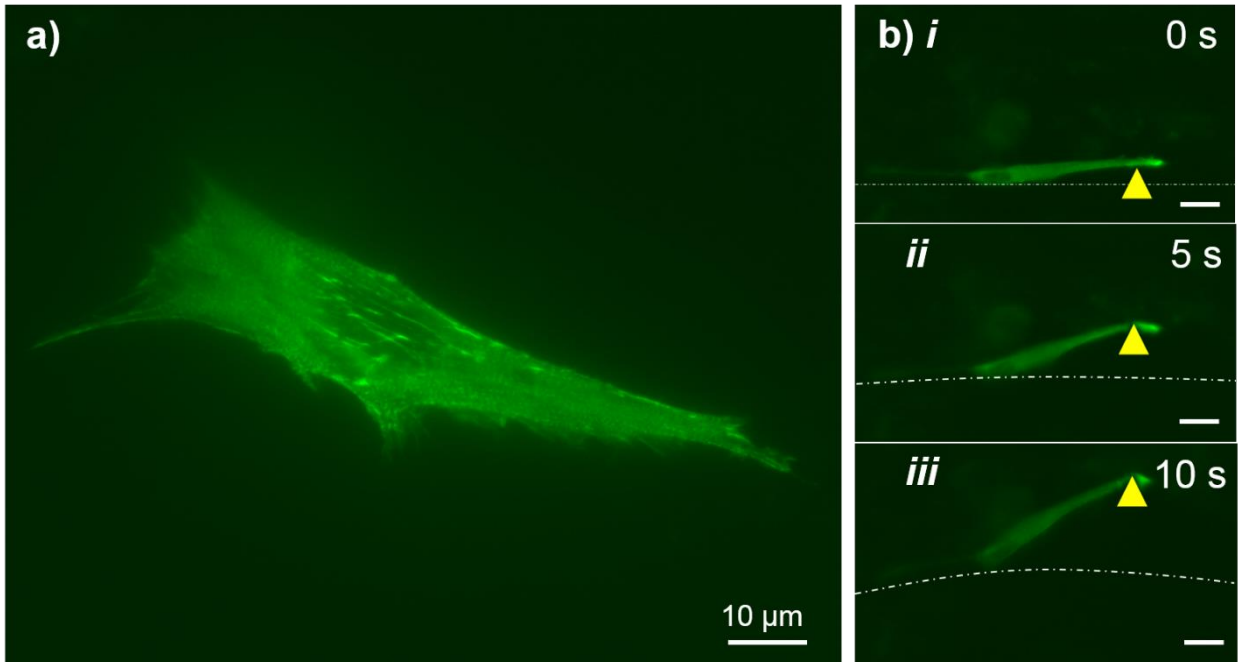

Figure 5-7. GFP transfection experiments on aneurysmal cells. (*a*) Flat glass substrate, with prominent α-actinin presence at expected locations. (*b*) A transfected cell on a STEP nanonet substrate (*estimated fiber curvature shown in white*) being pulled by the probe (*yellow arrow*).

Transfection in aneurysmal cells was confirmed by detection of GFP fluorescence at known α-actinin locations. On flat glass, this fluorescence was quite bright, as the stiff glass substrate is known to induce cytoskeletal development and associated α-actinin bundling. Unfortunately, transfection efficiency was relatively low. On flat glass this did not present a problem, but this made experiments on nanonets quite inefficient. First, cells are seeded onto nanonets from the top down, and not every cell attaches to the fibers. In the group of cells that do

attach, not every cell forms a parallel shape required for probe-based testing. While we have not directly measured this specific behavior, cells are seeded in a 35 µL droplet at a concentration of 100,000 cells/mL, which amounts to 3,500 cells per scaffold. An excellent scaffold would yield upwards of 50 parallel-shaped cells, with 3-5 times that amount attached in other configurations. We can therefore estimate that 50/3,500 cells seeded (1.4%) end up in a testable morphology. Again, in previous experiments this was a non-issue, as we essentially had a limitless supply of immortalized cells and were not interested in obtaining a specific subset of those cells. However, in the case of GFP-transfected cells where efficiency was relatively poor, the odds of getting a GFP-expressing cell to attach in the desired configuration decreased by a factor of the transfection efficiency, which if we estimate at 10% of the cell population, would be 0.14% of all seeded cells. Therefore, while not impossible, experimental throughput significantly decreases if the same protocol from C2C12 experiments is used. In the future, transfection and seeding efficiencies may be investigated to improve the number of testable cells on nanonets.

Cells transfected with dominant negative α-actinin mutants were still found and tested despite the low experimental throughput. Mutant α-actinin affected cell morphology, characterized by long filamentous protrusions surrounding a highly circular cell body (**Figure 5-8**). This cell shape resembles that of cells which have had contractile elements knocked down with cytoskeletal drugs blebbistatin (targets and depolymerizes myosin-II) or Y27632 (inhibits ROCK pathway).

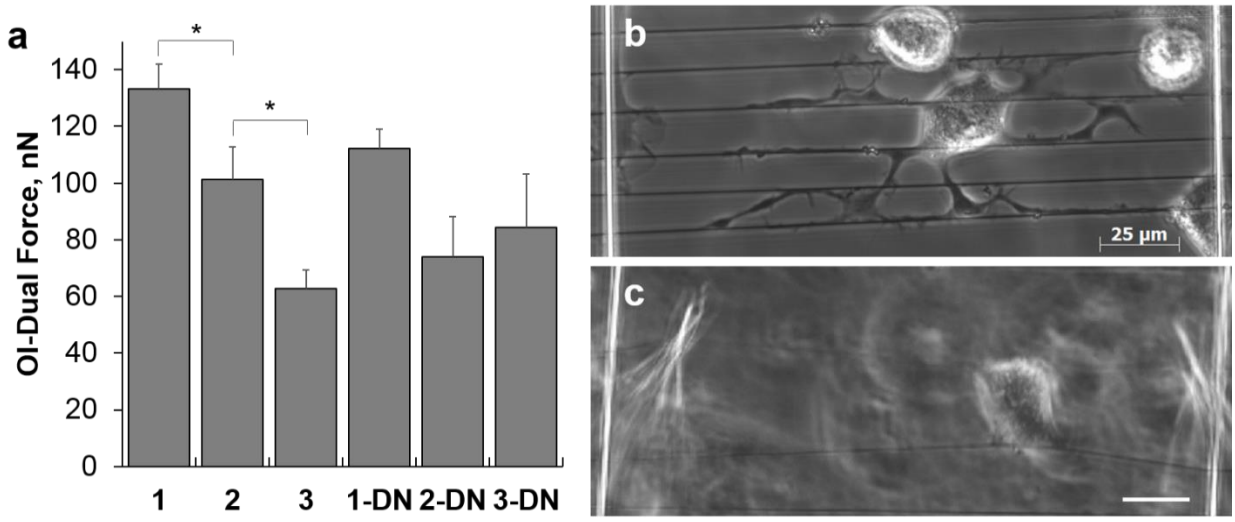

Figure 5-8. Outside-in forces for dominant negative (DN) α-actinin cells. (*a*). Non-aneurysmal cells displayed the highest adhesion force, followed by BAV non-aneurysmal and lastly aneurysmal. Mutant α-actinin decreased forces for categories 1 and 2, but increased forces in 3. Due to the low number of mutant cells tested (n = 3 for 3-DN group), we were unable to establish statistical significance of these findings.

Compared to non-transfected cells, dominant negative α-actinin cells showed reduced forces in groups 1 and 2 and a small increase in group 3. However, due to the low number of testable samples obtained (1-DN: n = 9; 2-DN: n = 7, 3-DN: n = 3), none of these changes from wild-type cells was statistically significant. It is possible that statistical significance could be established with an increased number of samples.

5.3.4 Effect of Hydrogen Peroxide Treatment

Since experimental difficulties were encountered with the transfection-based experiments, we decided to examine the effect of oxidative stress on cell forces via hydrogen peroxide treatment (H_20_2). Peroxide is added directly to culture media in a manner similar to previously-examined cytoskeletal drugs, allowing us to study a larger sample size for each patient. The motivation for studying peroxide's effect on cell forces is rooted in preliminary work from the Phillippi group at UPMC that has reported decreased ability of BAV patients to combat oxidative free radicals[191,192].

We hypothesized that this compromised mechanism may contribute to an altered force response in these cells as well.

Peroxide-treated media was first mixed by adding 5.6 µL hydrogen peroxide to 10 mL culture media, creating a 500 µM solution. After cells had been seeded onto nanonets, media was replaced with peroxide-containing media, and the cells were incubated for 30-minutes to allow oxidative stress to set in. Cells were then briefly imaged for inside-out forces and then pulled using the dual probe system for outside-in forces.

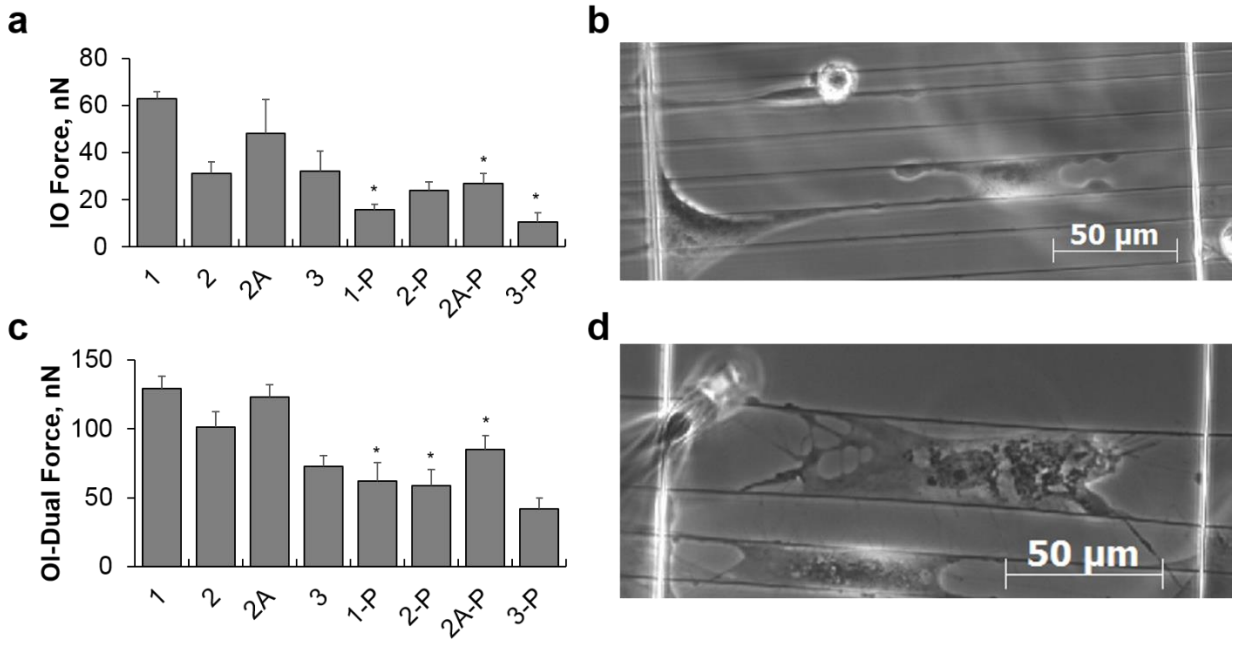

Figure 5-9. Effect of 500 µm hydrogen peroxide (-P) treatment on cells. (*a*) IO forces. (*b*) IO morphology. (*c*) OI forces. (*d*) OI morphology at failure. * indicates statistical significance from non-treated counterpart ($p<0.05$, N = 166).

Peroxide treatment affected cell morphology as evidenced by bleb-like cell protrusions at the cell periphery. Inside-out forces were significantly decreased in all groups except non-aneurysmal BAV patients (group 2) (**Figure 5-9**). This translated to percentage decreases of 1: 75%, 2: 23%, 2A: 43%, and 3: 67%. Therefore, inside-out forces do not appear to be selectively affected in the BAV group of cells. On the other hand, outside-in forces were significantly

decreased in all groups except aneurysmal patients (group 3). Percentage decreases of 1: 52%, 2: 42%, 2A: 31% and 3: 42% indicate that peroxide did not selectively decrease adhesion strength within patient groups.

5.3.5 Effect of Cyclic Perturbations

Since aortic smooth muscle cells are subject to cyclic externally-applied stretch *in vivo*, we wanted to determine if cells of different disease states responded differently to cyclic perturbations. Several adaptations were made to the cyclic test performed on C2C12's to more closely mimic *in vivo* forces. First, instead of only cycling the cell once or twice per 2-minute window, cells were continuously cycled. Second, strain rate was increased from 3 µm/s to 10 µm/s to increase cycle frequency (hardware limitations prevented further increases in frequency even if linear strain rate was further increased). Cells from groups 1, 2, 2A, and 3 were tested in this manner (n = 1 patient per group) (**Figure 5-10**).

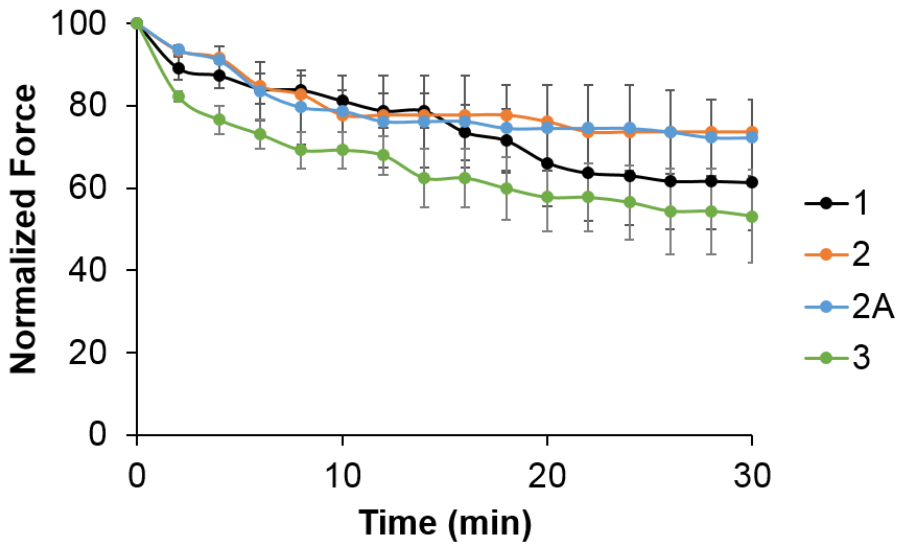

Figure 5-10. Force response of aortic smooth muscle cells to continuous cyclic sub-failure perturbation. (1: n = 4, 2: n = 2, 2A: n = 3, 3: n = 4).

Similar to C2C12 behavior, cells exhibited a reduced force over time during experimentation. Non-aneurysmal cells appeared to display two separate zones of response, in which a 20% reduction in force within the first 15 minutes of experimentation was followed by another 20% reduction in the next 15 minutes. We speculate that the initial response may be due to localized regions of adhesions failing, whereas the delayed response may be due to cytoskeletal remodeling to reduce the magnitude of the load that is transmitted through the cell body. In other words, higher reduction in force may indicate greater adaptation to outside-in manipulation. The BAV cell groups both show reductions in force values but to a lesser extent than the non-aneurysmal cells and appear to lack the delayed response altogether. An example of the amount of remodeling that is seen within this 30-minute window for both a non-aneurysmal cell and a BAV cell is shown in **Figure 5-11**. Lastly, the aneurysmal group displayed the greatest reduction in force throughout time compared to the other cells.

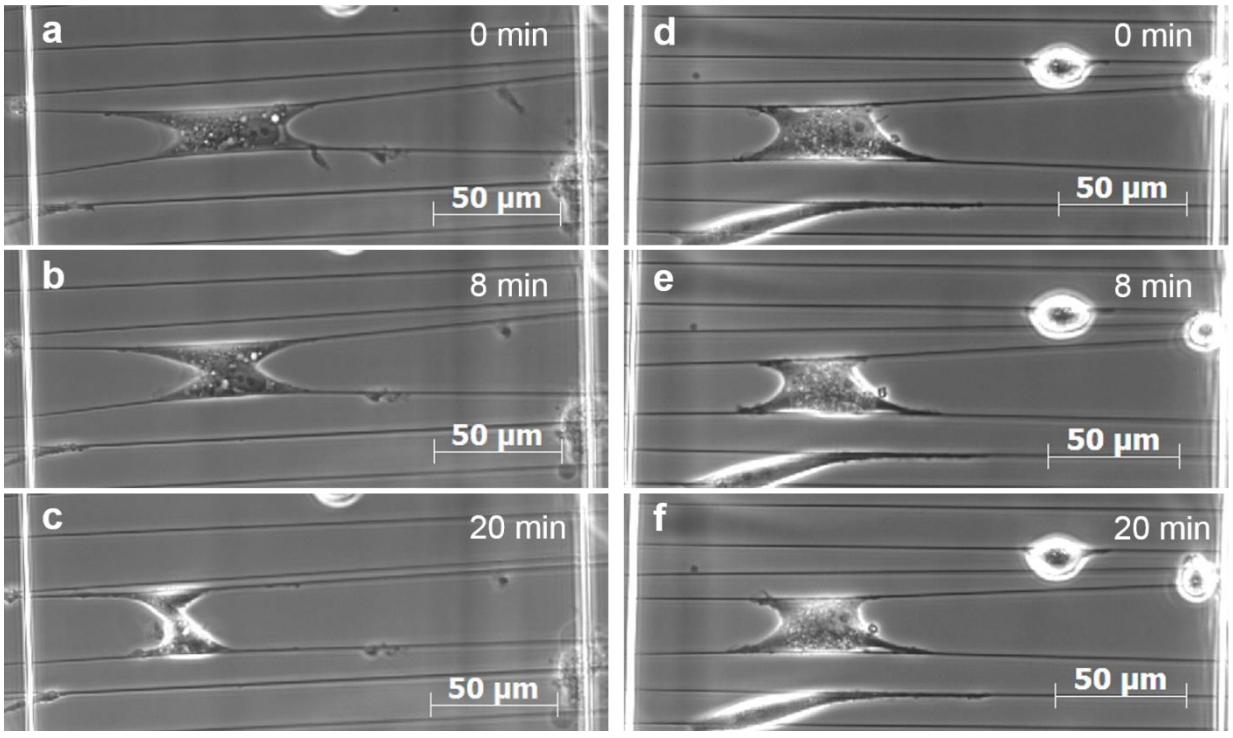

Figure 5-11. Remodeling of (*a-c*) a non-aneurysmal cell and (*d-f*) a non-aneurysmal BAV cell in response to cyclic loading at the same time points of experimentation.

5.4 Summary and Conclusions

Changes in single aortic smooth muscle cell mechanics as a result of aneurysm progression were detected using the STEP-based nanonet probe system. In the absence of perturbation, inside-out testing shows that non-aneurysmal cells exhibit the highest forces and each disease condition exhibits significantly lower forces. When pulled, adhesion forces for non-aneurysmal cells remain high, but are not statistically higher than BAV patients. Aneurysmal cells display both reduced inside-out and outside-in forces. Due to experimental difficulties, we were unable to determine whether α-actinin plays a role in force response, although mutant α-actinin could induce a visible change in cell morphology. Lastly, hydrogen peroxide reduced both inside-out and outside-in forces, but showed the greatest percentage reduction in the non-aneurysmal group.

To the best of our knowledge, this study represents the first effort to characterize and detect cardiovascular disease via changes in single-cell mechanical signatures. There are two main types of aneurysm: aortic aneurysm as investigated here, and cerebral aneurysm. While there are differences between the two types, it is imagined that knowledge gained from aortic experiments may be adapted to cerebral instances. In any case, results obtained through probe-based experimentation validate the importance of considering single-cell contributions to tissue-level abnormalities.

6. CONCLUDING REMARKS

6.1 Project Summary and Conclusions

The study of cell-fiber interactions has previously been limited by difficulties in fabrication of controlled fibrous hierarchical assemblies and micro/nanoscale characterization of the cell-fiber interface. STEP fiber manufacturing has enabled us to find that cells attach, arrange, migrate, and produce forces on fibers differently than on flat substrates. Such interactions stem from fiber suspension, structural stiffness, and substrate curvature. Cells cluster their adhesions at the periphery, which on fibers necessitates that they appear in predictable locations. This leads to the ability to use fiber arrangement as a means of inducing repeatable cellular shapes. One of these shapes, the parallel configuration, lends itself to outside-in manipulation by ensuring proper maintenance of boundary conditions when seeded on fused force scaffolds. By introducing an external probe-based perturbation system, the cell's adhesion strength, viscoelastic response, affinity for mismatched diameters, cytoskeletal rearrangement during cyclic loading, and cell-cell junction strength can all be examined while interacting with suspended nanofibers. We have demonstrated in this work the ability of this technology to investigate disease manifestation at the single-cell level for aortic smooth muscle cells. It is envisioned that the techniques investigated here will apply to other disease conditions as well, ultimately serving as an enabling technology that will enhance understanding of a multitude of single cell mechanical behaviors.

Extensive research in cell-fiber interactions have shown promising results for the future of tissue engineering, stem cell research, and oncology. Knowledge of these fundamental interactions may be used in the future to control cell behavior and produce desired clinical outcomes such as directing cell motion with increased migration speed in wound healing models, slowing or thwarting migration in cancerous cells, or optimizing scaffold conditions to ensure proper

colonization of tissue engineered scaffolds. When coupled with computational and mathematical modeling, drug-eluting fibers can someday be used as powerful diagnostic platforms for drug efficacy prediction and testing. The onset and progression of phenomena like cancer metastasis, nerve regeneration, and stem cell differentiation can all be better understood as details surrounding cell-fiber interactions continue to be revealed. Overall, the development of fiber-based scaffolds has made significant contributions to the field of biotechnology, and promises to advance studies in population level tissue engineering and single cell disease models.

6.2 Future Work

6.2.1 Cancer Cell Blebbing

One of the hallmarks of cancer is the ability of cancerous cells to evade apoptosis[193]. Plasma membrane blebbing, typically associated with apoptosis in normal cells, is a mechanism that cancerous cells use to remain alive. Cells have been observed to exhibit reversible membrane blebbing, a phenomenon in which increased hydrostatic pressure drives cytoplasm through local ruptures in the actin cortex[194]. Blebbing cells are thought to exist in a state of simultaneous hyper-contractility and reduced actin polymerization, but when corrected through the use of various cytoskeletal drugs, these same cells can revert back to lamellipodial protrusions[195]. Although blebbing is known to routinely occur during mitosis[196], the blebbing that we see in Denver Brain Tumor Research Group (DBTRG-05MG) cells consistently occurs throughout long durations of time. Furthermore, previous work in our group has shown a reversible blebbing/non-blebbing condition when the cell spreads/balls up past a critical spread area of 1400 μm^2, respectively[15]. Taken together, these works suggest that the non-mitotic blebbing that we see in cancer cells could be stopped via prolonged sub-failure stretch without the use of cytoskeletal drugs.

Sub-failure step stretch was applied to DBTRG-05MG cells that were blebbing. The step stretch was then held constant while cells transitioned from blebbing to lamellipodia (**Figure 6-1**). Forces were recorded as cells went through this transition.

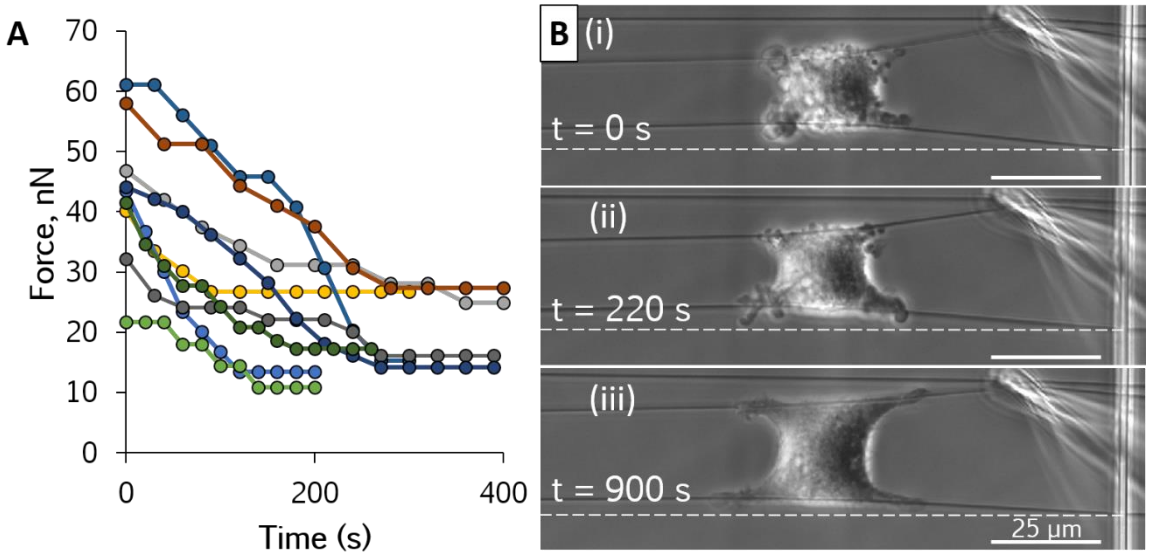

Figure 6-1. Forces involved in cancer cell blebbing reduction.

Onset of transition, evidenced by the first observed force decrease, required approximately 5-10 minutes to take place. Upon initializing transition, blebbing ceased and lamellipodia were observed after another 200-400 seconds. This transition was marked by decreased cell contractility wherein the average force reduced by 25 $\pm$ 11 nN (44% of blebbing force, n =9). These tests confirm that hyper-contractility is partially responsible for producing blebs, and for the first time demonstrates the forces involved in this reversal, which is induced mechanically in the absence of cytoskeletal drugs.

6.2.2 Calcium Wave Propagation

Live fluorescence markers enable real-time detection of biological events within the cell and are important for the probe system to detect. Future studies investigating live-marker response include studying forces associated with calcium wave initiation and propagation as well as forces associated with apoptosis. Demonstration of the ability of the probe system to simultaneously manipulate cells while capturing movement of biomolecules in short time spans can lead to detailed studies of such phenomenon in the future.

Calcium wave markers such as Fluo-4 (Invitrogen) fluoresce upon binding of calcium ions. Brightness of the fluorescent signal corresponds to calcium flux. Therefore, time-lapse fluorescence images are taken and presented as intensity-based color maps. In the example shown in **Figure 6-2**, a calcium wave is triggered when the probe breaks a fiber-fiber intersection on the left of the image. The fiber's sudden movement initiates calcium wave propagation from left to right. Cells which initially are cooler colors (low intensity signal) become hotter (high intensity signal) and then dissipate back to cooler colors. The STEP Lab may use this type of approach to investigate forces associated with calcium wave initiation and propagation.

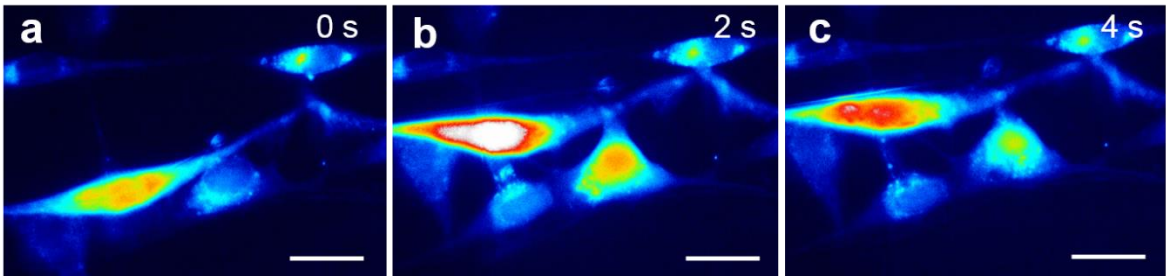

Figure 6-2. *(a-c)* Calcium wave propagation as a result of probe perturbation.

6.2.3 Custom Cell-Cell Junctions

Cell-cell junction studies reported in this work were all performed on cell-cell pairs that formed naturally on the scaffolds. When cell-cell contacts are desired for experimental purposes but cannot be located, the probe system can place two cells in proximity to one another to manually create this interface (**Figure 6-3**).

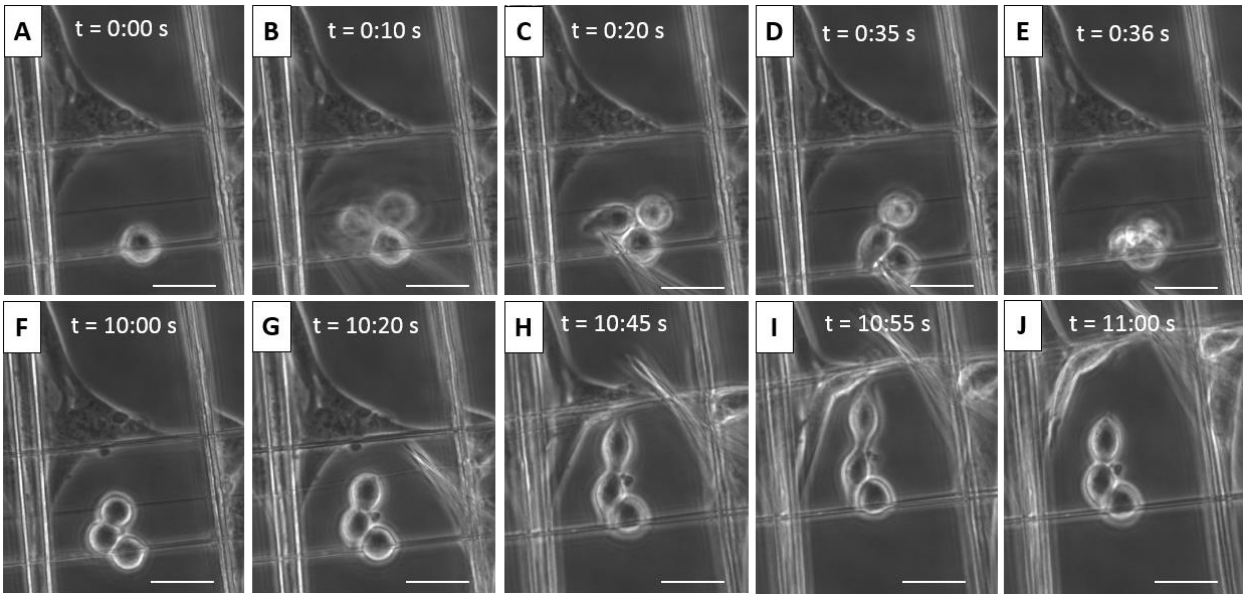

Figure 6-3. Manual creation of cell-cell junctions using the probe system. A) Single cell on single fiber. B) The probe selects a cell-cell pair from a neighboring fiber and moves it near the single cell. C) The pair is lowered into contact with the other cell. D) The cells are removed from the probe by dragging across the fiber. E) The three cells are now in contact. F) Ten minutes later, the cells have formed adhesions with the fiber. G) The probe pulls the cells apart. H) Adhesions remain intact. I) Failure begins to occur. J) Cell-fiber bonds break.

As shown in Figure 6-3, a single cell is initially attached to a single fiber. The probe removes a cell-cell pair from a neighboring fiber and lowers them into position in contact with the single cell. The probe is then dragged across a fiber to remove the cells from the probe. After 10 minutes of allowing the cells to attach, the probe is then used to pull the cells apart, demonstrating that adhesions have formed both at the cell-fiber and cell-cell interfaces.

It is imagined that this approach may be used in the future to test cell-cell adhesions of different types of cells, for instance cancerous and non-cancerous, and that multiple cell-cell

contacts may be tested as an initial attempt to scale up single-cell level forces into monolayer and tissue-level forces. To demonstrate the feasibility of such experiments, we created and tested a cell-cell junction composed of two different cell lines. This may be useful in the future when modeling, as an example, cancerous leader cells breaking away from non-cancerous counterpart tissue. Two cell lines had to be simultaneously cultured to accomplish this. Therefore, C2C12 cells were seeded onto nanonets as before, but instead of performing experiments in that same dish, the nanonet was transferred out of its original dish and into a second dish with NIH-3T3 fibroblasts expressing GFP-tagged tubulin attached to the bottom glass layer. The probe system then removed a GFP-tagged 3T3 cell from the bottom surface and placed it in contact with a C2C12 already attached to the fibers (**Figure 6-4**). As before, given enough time these cells were able to form contacts with one another, although the junction was not as prominent as those seen in cell-cell pairs of the same cell line. We envision that this experimental setup may be improved by either using cells of the same type (in this example C2C12's are not from the same tissue as NIH-3T3) or mechanically pre-conditioning the junction to induce growth prior to testing. In the future we may also consider attempting to test three or four cells in series as opposed to just two cells shown here. Doing so will enable us to study cells that are only adhered to other cells (and not nanofibers), perhaps mimicking *in vivo* environments of cells that are not attached to any fiber-based basement membrane.

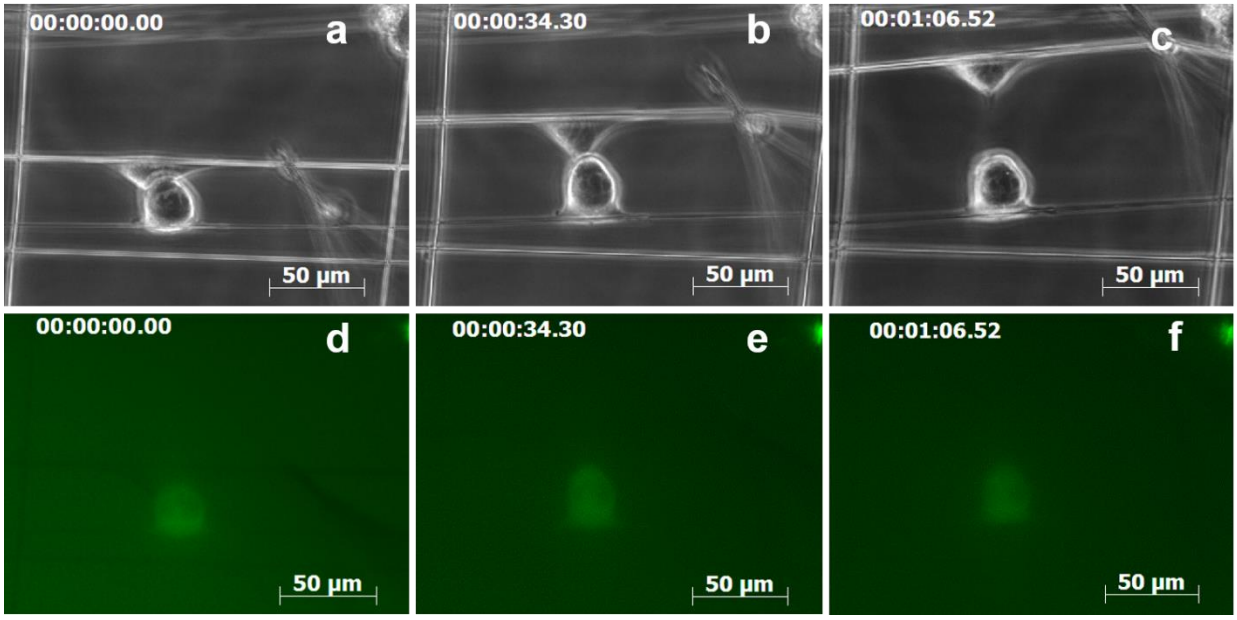

Figure 6-4. Manual cell-cell junction creation with two cell lines. (a-c) Phase images of C2C12 (top cell) separating from the GFP-tubulin expressing NIH-3T3 cell (bottom cell). (d-f) GFP signal only emanates from the 3T3 cell.

6.2.4 Single-Cell Forces for Stem Cell Differentiation

Mechanisms by which forces affect differentiation on nanonets remain largely unknown. It is known, however, that the nucleus is physically and mechanically linked to the ECM/substrate, such that forces initiated at adhesion sites are transmitted to the nucleus along F-actin stress fibers, nesprins, and LINC (linker of nulceoskeleton and cytoskeleton) proteins[197]. Therefore, substrate mechanics and topography affect not only cytoskeletal development but also activation of transcription factors and genes responsible for stem cell lineage commitment[26,30,198]. In the future, we envision creating force measurement scaffolds composed of fibers of different stiffnesses that will be used to drive mesenchymal stem cells (MSCs) towards different lineages, all while simultaneously measuring the forces which were required to initiate this differentiation process.

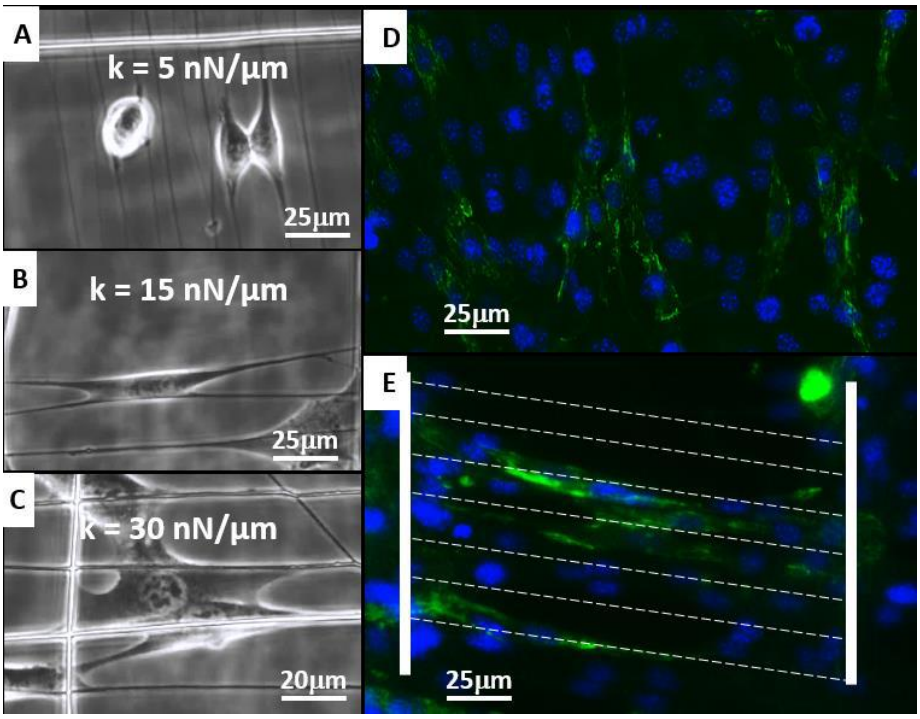

Figure 6-5. MSC differentiation on nanonets. A-C) Cell spreading is affected by fiber stiffness. D-E) Presence of MYOD1 myogenic marker (green) on MSCs attached to flat (top) and fibers (bottom, fibers marked in white).

Preliminary work in this regard has found that cell spreading and cell shape are dependent on nanonet stiffness and hierarchical assembly. When structural stiffness is very low (~ 5 nN/µm), we have observed cells to have difficulty fully spreading (**Figure 6-5** (A)). Instead, MSCs remain rounded while forming small adhesions and presumably less-developed cytoskeletons. We expect these types of cells to become adipocytes. As stiffness is increased to ~15 nN/µm, and given that two parallel fibers remain close (<20 µm) together, cells are able to spread between the fiber gap and form elongated structures (**Figure 6-5** (B)). In this configuration, cells use topography to preferentially migrate towards regions of higher stiffness (towards the fiber intersections). However, cells that are unable to reach these regions or those that begin to spread between stiffer regions have shown increased myogenic MyoD1 marker presence, indicating an increased muscle differentiation potential on a) softer and b) more elongated geometries (**Figure 6-5** (D,E)). Lastly, when the stiffness of the scaffold is increased to upwards of 30 nN/µm by increasing fiber diameter

and decreasing segment length, the cell will spread to great extents over multiple fibers (**Figure 6-5** (C)). We expect this type of cell to develop a mature cytoskeleton with large FACs, and to eventually differentiate into bone cell lineages.

In addition to our experiments performed examining MyoD1 presence on medium stiffness fibers, our preliminary results can be extended to show MSC behavior on significantly softer (<10 nN/μm) and stiffer (>30 nN/μm) nanonets. We believe adjustments to mechanical stiffness of the scaffolds will drive cell differentiation towards adipogenic and osteogenic lineages. We hypothesize that the scaffolds that result in more defined stress fibers (stiff substrates) will have an increased tendency to induce differentiation towards an osteoblastic lineage whereas those that result in less-defined stress fibers (soft substrates) will promote differentiation to muscle or fat. Cultured cells could be fixed and stained weekly for known markers of differentiation (Alkaline Phosphatase (ALP) – bone; MyoD1 – muscle; Oil Red O – fat). Particular attention can be given to avoid cell-cell contact. Forces exerted by the cells can be monitored over time and tracked for significant changes during which differentiation may take place (**Figure 6-6**).

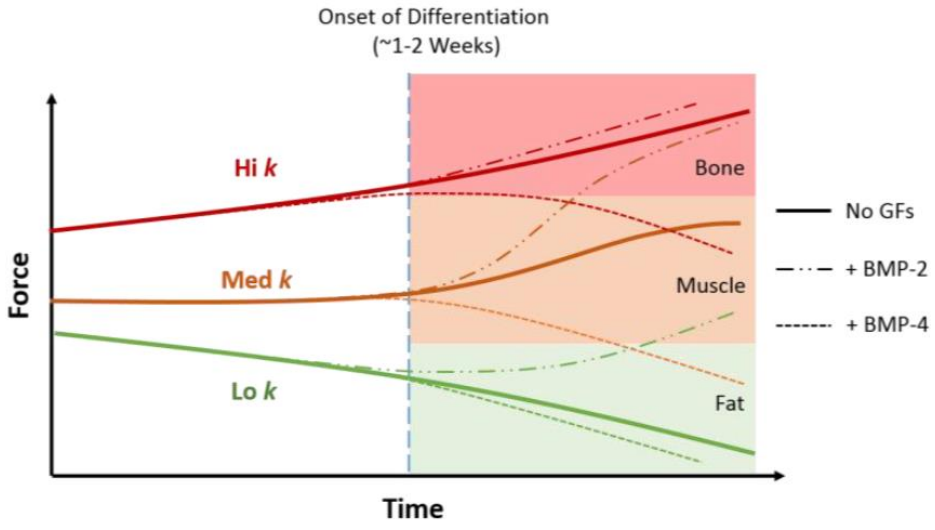

Figure 6-6. Schematic F-D master curves depicting single-cell force evolution over time. Initially, cells are seeded on nanonets of varying stiffnesses (hi, med, lo *k*). Forces are expected to noticeably change upon onset of differentiation, and the incorporation of growth factors is expected to affect the trajectory of each stiffness' line, with BMP-2

decreasing forces and BMP-4 increasing them. This growth factor (GF)-induced change may or may not be enough to push the cell to a different lineage, depending on mechanical influence.

It is expected that during the first 1-2 weeks of culture, cell forces will remain relatively constant and magnitudes will reflect the stiffness (*k*) of the nanonet that the cells are seeded on. However, upon the onset of differentiation, we expect the forces that the cell exerts to change according to lineage specification. For instance, myocyte differentiation should be accompanied by an increased force magnitude vs. the mesenchymal stem cell, whereas adipogenesis might show the opposite. We believe the mechanical cues present enough of a signal to cause each lineage, however, the effects of growth factors (GFs) may also be examined in this same manner. BMP-4, which triggers adipogenesis, should decrease the forces seen in each instance. On the other hand, BMP-2, which induces osteogenesis, should increase the forces for each stiffness nanonet. We hypothesize that whether or not this behavior is enough to change lineage depends on the relative influence of each cue (stiffness vs. concentration).

STEP scaffolds can be created with four zones of curvature and stiffnesses via diameter adjustment: small-small (~200 nm), small-large, large-small, and large-large (~1200 nm). In this configuration and in the absence of chemical cues, cells will experience physical cues that may direct three different lineages: adipogenic (on softest region with small-small diameter fibers), myogenic (medium regions with small-large fibers), and osteogenic (stiffest region with large-large fibers). We can then introduce chemical effectors in varying concentrations (10, 50, 100 ng/ml) to the cells to determine the relative contribution of chemical vs. physical effects, while simultaneously measuring the forces (**Figure 6-7**).

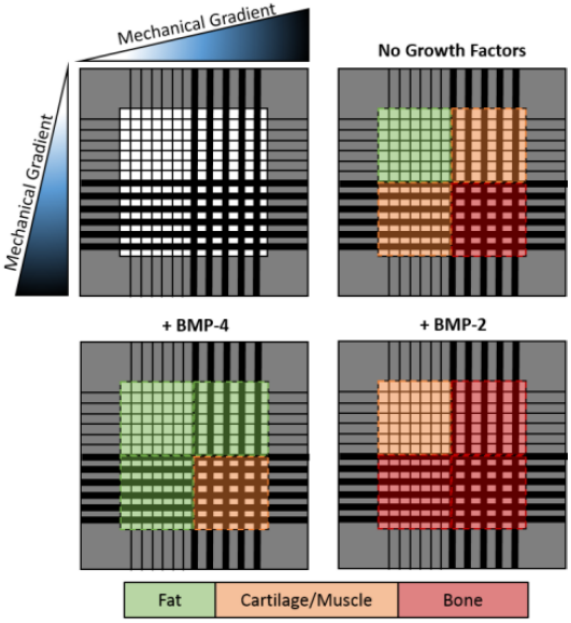

Figure 6-7. MSC differentiation in response to combined physical and chemical cues.

For instance, upon the addition of adipogenic BMP-4, softer sections of the scaffold may produce adipocytes while the stiffer regions may interpret the conflicting physical cue to prevent adipogenesis, instead becoming muscle or retaining stemness. Likewise, addition of BMP-2 may cause the majority of the scaffold to differentiate into bone, yet the softness of the small diameter region may override the chemical cue and prevent osteogenesis in this region. In such a scenario, the ability to tune the scaffold stiffness via fiber diameter and length adjustment will allow us to characterize the concentrations/stiffnesses required to cause these transitional zones, while also providing key insights in cell force modulation.

6.2.5 Future Outlook

The above items represent preliminary investigations into specific applications of the probe system which may be pursued more in-depth in the future. Having laid the groundwork for quantifying single-cell forces on nanofibers, it is envisioned that this platform may be improved

upon so that more advanced single-cell, cell-cell contact, and perhaps even monolayer studies may be performed. Furthermore, using this system in the presence of both biophysical and biochemical cues will ultimately advance both our understanding of the factors that affect cell behavior and our ability to manipulate those environments to elicit a desired cell response for clinical applications.

REFERENCES

1. Harris, A. K., Wild, P. & Stopak, D. Silicone rubber substrata: a new wrinkle in the study of cell locomotion. *Science* **208 ,** 177–179 (1980).

2. Lo, C. M., Wang, H. B., Dembo, M. & Wang, Y. L. Cell movement is guided by the rigidity of the substrate. *Biophys. J.* **79,** 144–152 (2000).

3. Engler, A. J., Sen, S., Sweeney, H. L. & Discher, D. E. Matrix elasticity directs stem cell lineage specification. *Cell* **126,** 677–689 (2006).

4. Martin, L. Effect of extracellular function , matrix hepatocytes topology cultured on cell in a sandwich configuration and physiological responsiveness : *FASEB J.* **10,** 1471–1484 (1996).

5. Sheets, K., Wunsch, S., Ng, C. & Nain, A. S. Shape-dependent cell migration and focal adhesion organization on suspended and aligned nanofiber scaffolds. *Acta Biomater.* **9,** 7169–7177 (2013).

6. Califano, J. P. & Reinhart-King, C. A. Substrate stiffness and cell area predict cellular traction stresses in single cells and cells in contact. *Cell. Mol. Bioeng.* **3,** 68–75 (2010).

7. Pathak, A. & Kumar, S. Independent regulation of tumor cell migration by matrix stiffness and confinement. *Proc. Natl. Acad. Sci. USA* **2012,** (2012).

8. Tee, S., Fu, J., Chen, C. S. & Janmey, P. A. Cell shape and substrate rigidity both regulate cell stiffness. *Biophys. J.* **100,** L25–L27 (2011).

9. Yeung, T. *et al.* Effects of substrate stiffness on cell morphology, cytoskeletal structure, and adhesion. *Cell Motil. Cytoskeleton* **60,** 24–34 (2005).

10. Discher, D. E., Janmey, P. & Wang, Y. L. Tissue cells feel and respond to the stiffness of their substrate. *Science* **310,** 1139–1143 (2005).

11. Kong, H. J. *et al.* Non-viral gene delivery regulated by stiffness of cell adhesion substrates. *Nat. Mater.* **4,** 460–464 (2005).

12. Isenberg, B. C., DiMilla, P. A., Walker, M., Kim, S. & Wong, J. Y. Vascular smooth muscle cell durotaxis depends on substrate stiffness gradient strength. *Biophys. J.* **97,** 1313–1322 (2009).

13. Pelham, R. J. & Wang, Y. Cell locomotion and focal adhesions are regulated by substrate flexibility. *Proc. Natl. Acad. Sci. USA* **94 ,** 13661–13665 (1997).

14. Willits, R. K. & Skornia, S. L. Effect of collagen gel stiffness on neurite extension. *J. Biomater. Sci. Polym. Ed.* **15,** 1521–1531 (2004).

15. Sharma, P., Sheets, K., Subbiah, E. & Nain, A. S. The mechanistic influence of aligned nanofibers on cell shape, migration and blebbing dynamics of glioma cells. *Integr. Biol.* **5,** 1036–44 (2013).

16. Meehan, S. Structural stiffness gradient along a single nanofiber and associated single cell response. *Virginia Tech, Blacksburg, VA.* (2013).

17. Ottani, V. *et al.* Collagen fibril arrangement and size distribution in monkey oral mucosa. *J. Anat.* **192,** 321–328 (1998).

18. Buehler, M. J. Nature designs tough collagen: explaining the nanostructure of collagen fibrils. *Proc. Natl. Acad. Sci. USA* **103,** 12285–12290 (2006).

19. Du, Y. *et al.* Synthetic sandwich culture of 3D hepatocyte monolayer. *Biomaterials* **29,** 290–301 (2008).

20. Rozario, T. & DeSimone, D. W. The extracellular matrix in development and morphogenesis: a dynamic view. *Dev. Biol.* **341,** 126–140 (2010).

21. Lazopoulos, K. A & Stamenović, D. Durotaxis as an elastic stability phenomenon. *J. Biomech.* **41,** 1289–1294 (2008).

22. Trappmann, B. *et al.* Extracellular-matrix tethering regulates stem-cell fate. *Nat. Mater.* **11,** 1–8 (2012).

23. Shin, M., Ishii, O., Sueda, T. & Vacanti, J. P. Contractile cardiac grafts using a novel nanofibrous mesh. *Biomaterials* **25,** 3717–3723 (2004).

24. Bader, A. *et al.* Tissue engineering of heart valves – human endothelial cell seeding of detergent acellularized porcine valves. *Eur. J. Cardio-Thoracic Surg.* **14 ,** 279–284 (1998).

25. Lutolf, M. P. & Hubbell, J. A. Synthetic biomaterials as instructive extracellular microenvironments for morphogenesis in tissue engineering. *Nat. Biotech.* **23,** 47–55 (2005).

26. DuFort, C. C., Paszek, M. J. & Weaver, V. M. Balancing forces: architectural control of mechanotransduction. *Nat. Rev. Mol. Cell Biol.* **12,** 308–19 (2011).

27. Chen, C. S. Mechanotransduction - a field pulling together? *J. Cell Sci.* **121,** 3285–3292 (2008).

28. Schwartz, M. A. Integrins and extracellular matrix in mechanotransduction. *Cold Spring Harb. Perspect. Biol.* **2,** a005066 (2010).

29. Wozniak, M. A. & Chen, C. S. Mechanotransduction in development: a growing role for contractility. *Nat. Rev. Mol. Cell Biol.* **10,** 34–43 (2009).

30. Jaalouk, D. E. & Lammerding, J. Mechanotransduction gone awry. **10,** 63–73 (2009).

31. Nikkhah, M., Edalat, F., Manoucheri, S. & Khademhosseini, A. Engineering microscale topographies to control the cell-substrate interface. *Biomaterials* **33,** 5230–5246 (2012).

32. Vogel, V. & Sheetz, M. Local force and geometry sensing regulate cell functions. *Nat. Rev. Mol. Cell Biol.* **7,** 265–75 (2006).

33. Talbot, L. J., Bhattacharya, S. D. & Kuo, P. C. Epithelial-mesenchymal transition, the tumor microenvironment, and metastatic behavior of epithelial malignancies. *Int. J. Biochem. Mol. Biol.* **3,** 117–136 (2012).

34. Jagielska, A. *et al.* Mechanical environment modulates biological properties of oligodendrocyte progenitor cells. *Stem Cells Dev*. **21,** 2905–2914 (2012).

35. Goldfinger, L. E. Integrin Signaling. *Encycl. Biol. Chem.* **2,** 608–612 (Elsevier Inc., 2013).

36. Holle, A. W. & Engler, A. J. More than a feeling: discovering, understanding, and influencing mechanosensing pathways. *Curr. Opin. Biotechnol.* **22,** 648–654 (2011).

37. Eyckmans, J., Boudou, T., Yu, X. & Chen, C. S. A hitchhiker's guide to mechanobiology. *Dev. Cell* **21,** 35–47 (2011).

38. Chen, J.-H., Liu, C., You, L. & Simmons, C. A. Boning up on Wolff's Law: Mechanical regulation of the cells that make and maintain bone. *J. Biomech.* **43,** 108–118 (2010).

39. Huang, C. & Ogawa, R. Mechanotransduction in bone repair and regeneration. *FASEB J.* **24 ,** 3625–3632 (2010).

40. Lele, T. P. *et al.* Mechanical forces alter zyxin unbinding kinetics within focal adhesions of living cells. *J. Cell. Physiol.* **207,** 187–194 (2006).

41. Chien, S. Mechanotransduction and endothelial cell homeostasis: the wisdom of the cell. *Am. J. Physiol. Heart Circ. Physiol.* **292,** H1209–H1224 (2007).

42. Agarwal, S., Greiner, A. & Wendorff, J. H. Functional materials by electrospinning of polymers. *Prog. Polym. Sci.* **38,** 963–991 (2013).

43. Doshi, J. & Reneker, D. H. Electrospinning process and applications of electrospun fibers. *J. Electrostat.* **35,** 151–160 (1995).

44. Huang, Z.-M., Zhang, Y. Z., Kotaki, M. & Ramakrishna, S. A review on polymer nanofibers by electrospinning and their applications in nanocomposites. *Compos. Sci. Technol.* **63,** 2223–2253 (2003).

45. Matthews, J. A., Wnek, G. E., Simpson, D. G. & Bowlin, G. L. Electrospinning of collagen nanofibers. *Biomacromolecules* **3,** 232–238 (2002).

46. Orlova, Y., Magome, N., Liu, L., Chen, Y. & Agladze, K. Electrospun nanofibers as a tool for architecture control in engineered cardiac tissue. *Biomaterials* **32,** 5615–24 (2011).

47. Formhals, A. Process and apparatus for preparing artificial threads. *U.S. Patent 1,975,504* (Oct. 2, 1934).

48. Formhals, A. Method and apparatus for spinning. *U.S. Patent 2,349,950* (May 30, 1939).

49. Formhals, A. Artificial thread and method of producing same. *U.S. Patent 2,187,306* (Jan. 16, 1940).

50. Taylor, G. Electrically driven jets. *Proc. R. Soc. London. A. Math. Phys. Sci.* **313 ,** 453–475 (1969).

51. Li, W.-J., Laurencin, C. T., Caterson, E. J., Tuan, R. S. & Ko, F. K. Electrospun nanofibrous structure: a novel scaffold for tissue engineering. *J. Biomed. Mater. Res.* **60,** 613–621 (2002).

52. Baker, B. M. & Mauck, R. L. The effect of nanofiber alignment on the maturation of engineered meniscus constructs. *Biomaterials* **28,** 1967–1977 (2007).

53. Li, D., Wang, Y. & Xia, Y. Electrospinning of polymeric and ceramic nanofibers as uniaxially aligned arrays. *Nano Lett.* **3,** 1167–1171 (2003).

54. Li, D. & Xia, Y. Fabrication of titania nanofibers by electrospinning. *Nano Lett.* **3,** 555–560 (2003).

55. Larsen, G., Velarde-Ortiz, R., Minchow, K., Barrero, A. & Loscertales, I. G. A method for making inorganic and hybrid (organic/inorganic) fibers and vesicles with diameters in the submicrometer and micrometer range via sol−gel chemistry and electrically forced liquid jets. *J. Am. Chem. Soc.* **125,** 1154–1155 (2003).

56. Viswanathamurthi, P. *et al.* Preparation and morphology of niobium oxide fibres by electrospinning. *Chem. Phys. Lett.* **374,** 79–84 (2003).

57. Dai, H., Gong, J., Kim, H. & Lee, D. A novel method for preparing ultra-fine alumina-borate oxide fibres via an electrospinning technique. *Nanotechnology* **13,** 674–677 (2002).

58. Katta, P., Alessandro, M., Ramsier, R. D. & Chase, G. G. Continuous electrospinning of aligned polymer nanofibers onto a wire drum collector. *Nano Lett.* **4,** 2215–2218 (2004).

59. Badrossamay, M. R., McIlwee, H. A., Goss, J. A & Parker, K. K. Nanofiber assembly by rotary jet-spinning. *Nano Lett.* **10,** 2257–2261 (2010).

60. Li, D., Ouyang, G., McCann, J. T. & Xia, Y. Collecting electrospun nanofibers with patterned electrodes. *Nano Lett.* **5,** 913–916 (2005).

61. Zussman, E., Theron, A. & Yarin, A. L. Formation of nanofiber crossbars in electrospinning. *Appl. Phys. Lett.* **82,** 973–975 (2003).

62. Theron, A., Zussman, E. & Yarin, A. Electrostatic field-assisted alignment of electrospun nanofibres. *Nanotechnology* **12,** 384–390 (2001).

63. Sarkar, S., Deevi, S. & Tepper, G. Biased AC electrospinning of aligned polymer nanofibers. *Macromol. Rapid Commun.* **28,** 1034–1039 (2007).

64. Carnell, L. S. *et al.* Aligned mats from electrospun single fibers. *Macromolecules* **41,** 5345–5349 (2008).

65. Sun, D., Chang, C., Li, S. & Lin, L. Near-field electrospinning. *Nano Lett.* **6,** 839–842 (2006).

66. Tutak, W. *et al.* The support of bone marrow stromal cell differentiation by airbrushed nanofiber scaffolds. *Biomaterials* **34,** 2389–2398 (2013).

67. Harfenist, S. A. *et al.* Direct drawing of suspended filamentary micro- and nanostructures from liquid polymers. *Nano Lett.* **4,** 1931–1937 (2004).

68. Nain, A. S., Wong, J. C., Amon, C. H., Sitti, M. & Nain Wong, J.C., Amon, C., Sitti, M., A. S. Drawing suspended polymer micro-/nanofibers using glass micropipettes. *Appl. Phys. Lett* **89,** 183105 (2006).

69. Sundaray, B. *et al.* Electrospinning of continuous aligned polymer fibers. *Appl. Phys. Lett.* **84,** 1222–1224 (2004).

70. Nain, A. S. *et al.* Dry spinning based spinneret based tunable engineered parameters (step) technique for controlled and aligned deposition of polymeric nanofibers. *Macromol. Rapid Commun.* **30,** 1406–1412 (2009).

71. Nain, A. S. & Wang, J. Polymeric nanofibers: isodiametric design space and methodology for depositing aligned nanofiber arrays in single and multiple layers. *Polym. J.* 695–700 (2013).

72. Nain, A. S. *et al.* Control of cell behavior by aligned micro/nanofibrous biomaterial scaffolds fabricated by spinneret-based tunable engineered parameters (STEP) technique. *Small* **4,** 1153–1159 (2008).

73. Hong, J. K. & Madihally, S. V. Three-dimensional scaffold of electrosprayed fibers with large pore size for tissue regeneration. *Acta Biomater.* **6,** 4734–4742 (2010).

74. Pabba, S. *et al.* Biopolymerization-driven self-assembly of nanofiber air-bridges. *Soft Matter* **5,** 1378 (2009).

75. Rathfon, J. M., Grolman, J. M., Crosby, A. J. & Tew, G. N. Formation of oriented, suspended fibers by melting free standing polystyrene thin films. *Macromolecules* **42,** 6716–6722 (2009).

76. Nain Amon, C., Sitti, M., A. S., Nain, A. S., Amon, C. & Sitti, M. Proximal probes based nanorobotic drawing of polymer micro/nanofibers. *Nanotechnology, IEEE Trans.* **5,** 499–510 (2006).

77. Su, B. *et al.* Elaborate positioning of nanowire arrays contributed by highly adhesive superhydrophobic pillar-structured substrates. *Adv. Mater.* **24,** 559–564 (2012).

78. Ricart, B. G., Yang, M. T., Hunter, C. A, Chen, C. S. & Hammer, D. a. Measuring traction forces of motile dendritic cells on micropost arrays. *Biophys. J.* **101,** 2620–2628 (2011).

79. Sabass, B., Gardel, M. L., Waterman, C. M. & Schwarz, U. S. High resolution traction force microscopy based on experimental and computational advances. *Biophys. J.* **94,** 207–220 (2008).

80. Rape, A. D., Guo, W.-H. & Wang, Y.-L. The regulation of traction force in relation to cell shape and focal adhesions. *Biomaterials* **32,** 2043–2051 (2011).

81. Fukuda, Y. S. and M. N. and S. K. and M. H. and M. K. and T. Single cell adhesion force measurement for cell viability identification using an AFM cantilever-based micro putter. *Meas. Sci. Technol.* **22,** 115802 (2011).

82. Yang, M. T., Sniadecki, N. J. & Chen, C. S. Geometric considerations of micro- to nanoscale elastomeric post arrays to study cellular traction forces. *Adv. Mater.* **19,** 3119–3123 (2007).

83. Raman, P. S., Paul, C. D., Stroka, K. M. & Konstantopoulos, K. Probing cell traction forces in confined microenvironments. *Lab Chip* **23,** 4599–4607 (2013).

84. Pelham, R. J. & Wang, Y. L. High resolution detection of mechanical forces exerted by locomoting fibroblasts on the substrate. *Mol. Biol. Cell* **10,** 935–945 (1999).

85. Maruthamuthu, V., Sabass, B., Schwarz, U. S. & Gardel, M. L. Cell-ECM traction force modulates endogenous tension at cell – cell contacts. *Proc. Natl. Acad. Sci. USA* **12,** 4708–4713 (2011).

86. Krishnan, R. *et al.* Reinforcement versus fluidization in cytoskeletal mechanoresponsiveness. *PLoS One* **4,** e5486 (2009).

87. Fu, J. *et al.* Mechanical regulation of cell function with geometrically modulated elastomeric substrates. *Nat. Methods* **7,** 733–736 (2010).

88. Lam, R. H. W., Weng, S., Lu, W. & Fu, J. Live-cell subcellular measurement of cell stiffness using a microengineered stretchable micropost array membrane. *Integr. Biol.* **4,** 1289–1298 (2012).

89. Kajzar, A., Cesa, C. M., Kirchgessner, N., Hoffmann, B. & Merkel, R. Toward physiological conditions for cell analyses: forces of heart muscle cells suspended between elastic micropillars. *Biophys. J.* **94,** 1854–1866 (2008).

90. Han, S. J., Bielawski, K. S., Ting, L. H., Rodriguez, M. L. & Sniadecki, N. J. Decoupling substrate stiffness, spread area, and micropost density: a close spatial relationship between traction forces and focal adhesions. *Biophys. J.* **103,** 640–648 (2012).

91. Nagayama, K., Adachi, A. & Matsumoto, T. Heterogeneous response of traction force at focal adhesions of vascular smooth muscle cells subjected to macroscopic stretch on a micropillar substrate. *J. Biomech.* **44,** 2699–2705 (2011).

92. Ferrell, N., Woodard, J. & Hansford, D. J. Measurement of cell forces using a microfabricated polymer cantilever sensor. *Sensors Actuators A Phys.* **170,** 84–89 (2011).

93. Desmaële, D., Boukallel, M. & Régnier, S. Actuation means for the mechanical stimulation of living cells via microelectromechanical systems: A critical review. *J. Biomech.* **44,** 1433–1446 (2011).

94. Nagayama, K., Yanagihara, S. & Matsumoto, T. A novel micro tensile tester with feed-back control for viscoelastic analysis of single isolated smooth muscle cells. *Med. Eng. Phys.* **29,** 620–628 (2007).

95. Miyazaki, H., Hasegawa, Y. & Hayashi, K. A newly designed tensile tester for cells and its application to fibroblasts. *J. Biomech.* **33,** 97–104 (2000).

96. Christ, K. V, Williamson, K. B., Masters, K. S. & Turner, K. T. Measurement of single-cell adhesion strength using a microfluidic assay. *Biomed. Microdevices* **12,** 443–55 (2010).

97. Das, T., Maiti, T. K. & Chakraborty, S. Traction force microscopy on-chip: shear deformation of fibroblast cells. *Lab Chip* **8,** 1308–1318 (2008).

98. Simon, A. & Durrieu, M.-C. Strategies and results of atomic force microscopy in the study of cellular adhesion. *Micron* **37,** 1–13 (2006).

99. Puech, P.-H., Poole, K., Knebel, D. & Muller, D. J. A new technical approach to quantify cell-cell adhesion forces by AFM. *Ultramicroscopy* **106,** 637–644 (2006).

100. Selhuber-Unkel, C. *et al.* Cell adhesion strength is controlled by intermolecular spacing of adhesion receptors. *Biophys. J.* **98,** 543–551 (2010).

101. García, a J., Ducheyne, P. & Boettiger, D. Quantification of cell adhesion using a spinning disc device and application to surface-reactive materials. *Biomaterials* **18,** 1091–1098 (1997).

102. Lu, H. *et al.* Microfluidic shear devices for quantitative analysis of cell adhesion. *Anal. Chem.* **76,** 5257–5264 (2004).

103. Ashok, P. C. & Dholakia, K. Optical trapping for analytical biotechnology. *Curr. Opin. Biotechnol.* **23,** 16–21 (2011).

104. Kamm, R., Lammerding, J. & Mofrad, M. Cellular nanomechanics. In: *Springer Handb. Nanotechnol.* (Bhushan, B.) 1171–1200 (Springer, 2010).

105. Van Vliet, K., Bao, G. & Suresh, S. The biomechanics toolbox: experimental approaches for living cells and biomolecules. *Acta Mater.* **51,** 5881–5905 (2003).

106. Wang, N. & Ingber, D. E. Probing transmembrane mechanical coupling and cytomechanics using magnetic twisting cytometry. *Biochem Cell Biol* **73,** 327–335 (1995).

107. Shen, Y., Nakajima, M., Kojima, S., Homma, M. & Fukuda, T. Study of the time effect on the strength of cell-cell adhesion force by a novel nano-picker. *Biochem. Biophys. Res. Commun.* **409,** 160–165 (2011).

108. Thoumine, O., Ott, A., Cardoso, O. & Meister, J. J. Microplates: a new tool for manipulation and mechanical perturbation of individual cells. *J. Biochem. Biophys. Methods* **39,** 47–62 (1999).

109. Doyle, A. D., Wang, F. W., Matsumoto, K. & Yamada, K. M. One-dimensional topography underlies three-dimensional fibrillar cell migration. *J. Cell Biol.* **184,** 481–490 (2009).

110. Sheets, K., Sharma, P., Koons, B. & Nain, A. S. Cell interactions in wire (fiber)-based structures and scaffolds. In *CRC Handb. Imaging* (Genin. G, Neu, C) (Taylor and Francis, 2014).

111. Li, F., Redick, S. D., Erickson, H. P. & Moy, V. T. Force measurements of the alpha5beta1 integrin-fibronectin interaction. *Biophys. J.* **84,** 1252–1262 (2003).

112. Vidal, G. *et al.* The effect of surface energy, adsorbed RGD peptides and fibronectin on the attachment and spreading of cells on multiwalled carbon nanotube papers. *Carbon N. Y.* **49,** 2318–2333 (2011).

113. Kraning-Rush, C. M., Carey, S. P., Califano, J. P., Smith, B. N. & Reinhart-King, C. A. The role of the cytoskeleton in cellular force generation in 2D and 3D environments. *Phys. Biol.* **8,** 015009 (2011).

114. Choi, C. K. *et al.* Actin and alpha-actinin orchestrate the assembly and maturation of nascent adhesions in a myosin II motor-independent manner. *Nat. Cell Biol.* **10,** 1039–1050 (2008).

115. Schliwa, M. Action of cytochalasin D on cytoskeletal networks. *J. Cell Biol.* **92,** 79–91 (1982).

116. Dou, Y., Arlock, P. & Arner, A. Blebbistatin specifically inhibits actin-myosin interaction in mouse cardiac muscle. *Am. J. Physiol. Cell Physiol.* **293,** C1148–C1153 (2007).

117. Takesono, A., Heasman, S. J., Wojciak-Stothard, B., Garg, R. & Ridley, A. J. Microtubules regulate migratory polarity through Rho/ROCK signaling in T cells. *PLoS One* **5,** e8774 (2010).

118. Dahl, K. N., Kahn, S. M., Wilson, K. L. & Discher, D. E. The nuclear envelope lamina network has elasticity and a compressibility limit suggestive of a molecular shock absorber. *J. Cell Sci.* **117,** 4779–4786 (2004).

119. Panorchan, P., Schafer, B. W., Wirtz, D. & Tseng, Y. Nuclear envelope breakdown requires overcoming the mechanical integrity of the nuclear lamina. *J. Biol. Chem.* **279,** 43462–43467 (2004).

120. Shivashankar, G. V. Mechanosignaling to the cell nucleus and gene regulation. *Annu. Rev. Biophys.* **40,** 361–378 (2011).

121. Bella, J. & Berman, H. M. Integrin–collagen complex: a metal–glutamate handshake. *Structure* **8,** R121–R126 (2000).

122. Gardel, M. L., Schneider, I. C., Aratyn-Schaus, Y. & Waterman, C. M. Mechanical integration of actin and adhesion dynamics in cell migration. *Annu. Rev. Cell Dev. Biol.* **26,** 315–333 (2010).

123. Galbraith, C. G., Yamada, K. M. & Sheetz, M. P. The relationship between force and focal complex development. *J. Cell Biol.* **159 ,** 695–705 (2002).

124. Nagano, M., Hoshino, D., Koshikawa, N., Akizawa, T. & Seiki, M. Turnover of focal adhesions and cancer cell migration. *Int. J. Cell Biol.* **2012,** 310616 (2012).

125. Kim, M.-C. *et al.* Integrating focal adhesion dynamics, cytoskeleton remodeling, and actin motor activity for predicting cell migration on 3D curved surfaces of the extracellular matrix. *Integr. Biol.* **4,** 1386–1397 (2012).

126. Kim, D.-H. & Wirtz, D. Focal adhesion size uniquely predicts cell migration. *FASEB J.* **27,** 1351–1361 (2013).

127. Andalib, M. N., Lee, J. S., Ha, L., Dzenis, Y. & Lim, J. Y. The role of RhoA kinase (ROCK) in cell alignment on nanofibers. *Acta Biomater.* **8,** 7737–7745 (2013).

128. Fuh, Y. K., Chen, S. Z. & He, Z. Y. Direct-write, highly aligned chitosan-poly(ethylene oxide) nanofiber patterns for cell morphology and spreading control. *Nanoscale Res. Lett.* **8,** 97 (2013).

129. Stricker, J., Aratyn-Schaus, Y., Oakes, P. W. & Gardel, M. L. Spatiotemporal constraints on the force-dependent growth of focal adhesions. *Biophys. J.* **100,** 2883–2893 (2011).

130. Berginski, M. E., Vitriol, E. A., Hahn, K. M. & Gomez, S. M. High-resolution quantification of focal adhesion spatiotemporal dynamics in living cells. *PLoS One* **6,** e22025 (2011).

131. Kovács, M., Tóth, J., Hetényi, C., Málnási-Csizmadia, A. & Sellers, J. R. Mechanism of blebbistatin inhibition of myosin II. *J. Biol. Chem.* **279,** 35557–35563 (2004).

132. Crow, A. *et al.* Contractile equilibration of single cells to step changes in extracellular stiffness. *Biophys. J.* **102,** 443–451 (2012).

133. Marceiller, J., Drechou, A., Durand, G., Perez, F. & Poüs, C. Kinesin is involved in protecting nascent microtubules from disassembly after recovery from nocodazole treatment. *Exp. Cell Res.* **304,** 483–492 (2005).

134. Attia, S. M., Badary, O. A., Hamada, F. M., Hrabé de Angelis, M. & Adler, I.-D. The chemotherapeutic agents nocodazole and amsacrine cause meiotic delay and non-disjunction in spermatocytes of mice. *Mutat. Res.* **651,** 105–113 (2008).

135. Schulze, C., Müller, K., Käs, J. A. & Gerdelmann, J. C. Compaction of cell shape occurs before decrease of elasticity in CHO-K1 cells treated with actin cytoskeleton disrupting drug cytochalasin D. *Cell Motil. Cytoskeleton* **66,** 193–201 (2009).

136. Yarrow, J. C., Perlman, Z. E., Westwood, N. J. & Mitchison, T. J. A high-throughput cell migration assay using scratch wound healing, a comparison of image-based readout methods. *BMC Biotechnol.* **4,** 21 (2004).

137. Diener, A. *et al.* Control of focal adhesion dynamics by material surface characteristics. *Biomaterials* **26,** 383–392 (2005).

138. Ulrich, T. A, Pardo, E. M. de J., Kumar, S. & de Juan Pardo, E. M. The mechanical rigidity of the extracellular matrix regulates the structure, motility, and proliferation of glioma cells. *Cancer Res.* **69,** 4167–4174 (2009).

139. Senju, Y. & Miyata, H. The role of actomyosin contractility in the formation and dynamics of actin bundles during fibroblast spreading. *J. Biochem.* **145,** 137–150 (2009).

140. Carlisle, C. R., Coulais, C. & Guthold, M. The mechanical stress–strain properties of single electrospun collagen type I nanofibers. *Acta Biomater.* **6,** 2997–3003 (2010).

141. Gestos, A., Whitten, P. G., Spinks, G. M. & Wallace, G. G. Tensile testing of individual glassy, rubbery and hydrogel electrospun polymer nanofibres to high strain using the atomic force microscope. *Polym. Test.* **32,** 655–664 (2013).

142. Somà, A. & Ballestra, A. Residual stress measurement method in MEMS microbeams using frequency shift data. *J. Micromechanics Microengineering* **19,** 095023 (2009).

143. Yu, S. *et al.* Osteogenic differentiation of C2C12 myogenic progenitor cells requires the Fos-related antigen Fra-1 - a novel target of Runx2. *Biochem. Biophys. Res. Commun.* **430,** 173–178 (2013).

144. Murphy, W. L., Mcdevitt, T. C. & Engler, A. J. Materials as stem cell regulators. *Nat. Mater.* **13,** 547–557 (2014).

145. Mathur, A., Moore, S. W., Sheetz, M. P. & Hone, J. The role of feature curvature in contact guidance. *Acta Biomater.* **8,** 2595–2601 (2012).

146. Elineni, K. K. & Gallant, N. D. Regulation of cell adhesion strength by peripheral focal adhesion distribution. *Biophys. J.* **101,** 2903–2911 (2011).

147. Gautrot, J. E. *et al.* The nanoscale geometrical maturation of focal adhesions controls stem cell differentiation and mechano-transduction. *Nano Lett.* **14,** 3945–3952 (2014).

148. Leerberg, J. M. & Yap, A. S. Vinculin, cadherin mechanotransduction and homeostasis of cell-cell junctions. *Protoplasma* **250,** 817–829 (2013).

149. Liu, Z. *et al.* Mechanical tugging force regulates the size of cell-cell junctions. *Proc. Natl. Acad. Sci. USA* **107,** 9944–9949 (2010).

150. Cavey, M. & Lecuit, T. Molecular bases of cell-cell junctions stability and dynamics. *Cold Spring Harb. Perspect. Biol.* **1,** a002998–a002998 (2009).

151. Chun, J. T., Santella, L., Zoologica, S., Dohrn, A. & Comunale, V. Intracellular Calcium Waves. *Encycl. Biol. Chem.* 640–647 (Elsevier Inc., 2013).

152. Ku, S. H., Lee, S. H. & Park, C. B. Synergic effects of nanofiber alignment and electroactivity on myoblast differentiation. *Biomaterials* **33,** 6098–6104 (2012).

153. Xie, H., Yin, M., Rong, W. & Sun, L. In situ quantification of living cell adhesion forces: single cell force spectroscopy with a nanotweezer. *Langmuir*. **30,** 2952–2959 (2014).

154. Hoelzle, M. K. & Svitkina, T. The cytoskeletal mechanisms of cell-cell junction formation in endothelial cells. *Mol. Biol. Cell* **23,** 310–323 (2012).

155. Brevier, J., Montero, D., Svitkina, T. & Riveline, D. The asymmetric self-assembly mechanism of adherens junctions: a cellular push-pull unit. *Phys. Biol.* **5,** 016005 (2008).

156. Chu, Y.-S. *et al.* Force measurements in E-cadherin-mediated cell doublets reveal rapid adhesion strengthened by actin cytoskeleton remodeling through Rac and Cdc42. *J. Cell Biol.* **167,** 1183–1194 (2004).

157. Ratheesh, A. & Yap, A. S. A bigger picture: classical cadherins and the dynamic actin cytoskeleton. *Nat. Rev. Mol. Cell Biol.* **13,** 673–679 (2012).

158. Hoffman, L. M., Jensen, C. C., Chaturvedi, A., Yoshigi, M. & Beckerle, M. C. Stretch-induced actin remodeling requires targeting of zyxin to stress fibers and recruitment of actin regulators. *Mol. Biol. Cell* **23,** 1846–1859 (2012).

159. Huang, L., Mathieu, P. S. & Helmke, B. P. A stretching device for high-resolution live-cell imaging. *Ann. Biomed. Eng.* **38,** 1728–1740 (2010).

160. Jungbauer, S., Gao, H., Spatz, J. P. & Kemkemer, R. Two characteristic regimes in frequency-dependent dynamic reorientation of fibroblasts on cyclically stretched substrates. *Biophys. J.* **95,** 3470–3478 (2008).

161. Chen, B., Kemkemer, R., Deibler, M., Spatz, J. & Gao, H. Cyclic stretch induces cell reorientation on substrates by destabilizing catch bonds in focal adhesions. *PLoS One* **7,** e48346 (2012).

162. Colombelli, J. *et al.* Mechanosensing in actin stress fibers revealed by a close correlation between force and protein localization. *J. Cell Sci.* **122,** 1928–1928 (2009).

163. Amano, M., Nakayama, M. & Kaibuchi, K. Rho-kinase/ROCK: A key regulator of the cytoskeleton and cell polarity. *Cytoskeleton.* **67,** 545–554 (2010).

164. Ishizaki, T. *et al.* Pharmacological properties of Y-27632, a specific inhibitor of rho-associated kinases. *Mol. Pharmacol.* **57,** 976–983 (2000).

165. Matthews, B. D., Overby, D. R., Mannix, R. & Ingber, D. E. Cellular adaptation to mechanical stress: role of integrins, Rho, cytoskeletal tension and mechanosensitive ion channels. *J. Cell Sci.* **119,** 508–18 (2006).

166. McGraw, K. L. *et al.* Erythropoietin receptor signaling is membrane raft dependent. *PLoS One* **7,** e34477 (2012).

167. Gadhari, N., Charnley, M., Marelli, M., Brugger, J. & Chiquet, M. Cell shape-dependent early responses of fibroblasts to cyclic strain. *Biochim. Biophys. Acta*. **1833,** 3415–3425 (2013).

168. Janmey, P. a *et al.* The mechanical properties of actin gels. Elastic modulus and filament motions. *J. Biol. Chem.* **269,** 32503–32513 (1994).

169. Darling, E. M., Zauscher, S., Block, J. A & Guilak, F. A thin-layer model for viscoelastic, stress-relaxation testing of cells using atomic force microscopy: do cell properties reflect metastatic potential? *Biophys. J.* **92,** 1784–1791 (2007).

170. Leipzig, N. D. & Athanasiou, K. A. Unconfined creep compression of chondrocytes. *J. Biomech.* **38,** 77–85 (2005).

171. Moreo, P., García-Aznar, J. M. & Doblaré, M. Modeling mechanosensing and its effect on the migration and proliferation of adherent cells. *Acta Biomater.* **4,** 613–621 (2008).

172. Ingber, D. E. *et al.* Opposing views on tensegrity as a structural framework. 1663–1678 (2012).

173. Ezratty, E. J., Partridge, M. A. & Gundersen, G. G. Microtubule-induced focal adhesion disassembly is mediated by dynamin and focal adhesion kinase. *Nat. Cell Biol.* **7,** 581–590 (2005).

174. Fournier, M. F., Sauser, R., Ambrosi, D., Meister, J.-J. & Verkhovsky, A. B. Force transmission in migrating cells. *J. Cell Biol.* **188,** 287–297 (2010).

175. Gleason, T. G. Contemporary management of aortic dissection: introduction. *Semin. Thorac. Cardiovasc. Surg.* **17,** 213 (2005).

176. Larson, E. W. & Edwards, W. D. Risk factors for aortic dissection: a necropsy study of 161 cases. *Am. J. Cardiol.* **53,** 849–855 (1984).

177. Sheets, C. A. & Janz, T. G. Ruptured thoracic aneurysm presenting as dyspnea and hypotension. *Ann. Emerg. Med.* **17,** 718–721 (1988).

178. Vorp, D. A. & Vande Geest, J. P. Biomechanical determinants of abdominal aortic aneurysm rupture. *Arterioscler. Thromb. Vasc. Biol.* **25,** 1558–1566 (2005).

179. Kauffmann, C. *et al.* Measurements and detection of abdominal aortic aneurysm growth: Accuracy and reproducibility of a segmentation software. *Eur. J. Radiol.* **81,** 1688–1694 (2012).

180. Darwood, R. *et al.* Twenty-year review of abdominal aortic aneurysm screening in men in the county of Gloucestershire, United Kingdom. *J. Vasc. Surg.* **56,** 8–13 (2012).

181. Pacini, D. *et al.* Acute aortic dissection: Epidemiology and outcomes. *Int. J. Cardiol.* **167,** 2806–2812 (2012).

182. Greenhalgh, R. M. *et al.* Endovascular versus open repair of abdominal aortic aneurysm. *N. Engl. J. Med.* **362,** 1863–1871 (2010).

183. Vorp, D. A. *et al.* Effect of aneurysm on the tensile strength and biomechanical behavior of the ascending thoracic aorta. *Ann. Thorac. Surg.* **75,** 1210–1214 (2003).

184. Fillinger, M. F., Marra, S. P., Raghavan, M. L. & Kennedy, F. E. Prediction of rupture risk in abdominal aortic aneurysm during observation: wall stress versus diameter. *J. Vasc. Surg.* **37,** 724–732 (2003).

185. Xiong, W., Knispel, R. A., Dietz, H. C., Ramirez, F. & Baxter, B. T. Doxycycline delays aneurysm rupture in a mouse model of Marfan syndrome. *J. Vasc. Surg.* **47,** 166–172 (2008).

186. Milewicz, D. M. *et al.* Genetic basis of thoracic aortic aneurysms and dissections: focus on smooth muscle cell contractile dysfunction. *Annu. Rev. Genomics Hum. Genet.* **9,** 283–302 (2008).

187. Burridge, K. & Wittchen, E. S. The tension mounts: Stress fibers as force-generating mechanotransducers. *J. Cell Biol.* **200 ,** 9–19 (2013).

188. Roca-Cusachs, P. *et al.* Integrin-dependent force transmission to the extracellular matrix by α-actinin triggers adhesion maturation. *Proc. Natl. Acad. Sci. USA* **110,** E1361–E1370 (2013).

189. Mummery, C. *et al.* Cardiomyocyte differentiation of mouse and human embryonic stem cells. *J. Anat.* **200,** 233–242 (2002).

190. Ailawadi, G. *et al.* Smooth muscle phenotypic modulation is an early event in aortic aneurysms. *J. Thorac. Cardiovasc. Surg.* **138,** 1392–1399 (2009).

191. Phillippi, J. A., Eskay, M. A., Kubala, A. A., Pitt, B. R. & Gleason, T. G. Altered oxidative stress responses and increased type I collagen expression in bicuspid aortic valve patients. *Ann. Thorac. Surg.* **90,** 1893–1898 (2010).

192. Phillippi, J. A. *et al.* Basal and oxidative stress-induced expression of metallothionein is decreased in ascending aortic aneurysms of bicuspid aortic valve patients. *Circulation* **119,** 2498–2506 (2009).

193. Hanahan, D. & Weinberg, R. A. Hallmarks of cancer: the next generation. *Cell* **144,** 646–674 (2011).

194. Ridley, A. J. Life at the leading edge. *Cell* **145,** 1012–1022 (2011).

195. Bergert, M., Chandradoss, S. D., Desai, R. a & Paluch, E. Cell mechanics control rapid transitions between blebs and lamellipodia during migration. *Proc. Natl. Acad. Sci. USA* **109,** 14434–14439 (2012).

196. Laster, S. M. & Mackenzie, J. M. Bleb formation and F-actin distribution during mitosis and tumor necrosis factor-induced apoptosis. *Microsc. Res. Tech.* **34,** 272–280 (1996).

197. Wang, N., Tytell, J. D. & Ingber, D. E. Mechanotransduction at a distance: mechanically coupling the extracellular matrix with the nucleus. *Nat. Rev. Mol. Cell Biol.* **10,** 75–82 (2009).

198. Huang, X. *et al.* Matrix stiffness-induced myofibroblast differentiation is mediated by intrinsic mechanotransduction. *Am. J. Respir. Cell Mol. Biol.* **47,** 340–348 (2012).

199. Cuenot, S., Frétigny, C., Demoustier-Champagne, S. & Nysten, B. Surface tension effect on the mechanical properties of nanomaterials measured by atomic force microscopy. *Phys. Rev. B* **69,** 165410 (2004).

8. APPENDIX

8.1 Derivation of Force Equation

Equations used to calculate forces based on fiber deflection are derived from Timoshenko's tie rod with lateral loading. After deriving equations for a beam under compressive load 'S', a negative sign is included to convert to a beam under tension. A summary/excerpt of the relevant derivation from Timoshenko's "Strength of Materials" book is provided below.

Assuming a hinged tie rod is held under compression and loaded perpendicularly to the fiber axis with a single point load, the differential equations describing the deflection curve up to the location of the point load and following the point load are:

$$EI\frac{d^2y}{dx^2} = -Sy - \frac{Pc}{l}x \qquad \text{(a)}$$

$$EI\frac{d^2y}{dx^2} = -Sy - \frac{P(l-c)}{l}(l-x) \qquad \text{(b)}$$

We then define:

$$\frac{S}{EI} = p^2$$

The solutions to (a) and (b) are then:

$$y = C_1\cos px + C_2\sin px - \frac{Pc}{Sl}x \qquad \text{(c)}$$

$$y = C_3\cos px + C_4\sin px - \frac{P(l-c)}{Sl}(l-x) \qquad \text{(d)}$$

Boundary conditions are then applied considering there are no fiber deflections at the pinned ends of the strut:

$$C_1 = 0$$

$$C_3 = -C_4\tan pl$$

The other two integration constants are achieved by recognizing deflection and slope continuity at the point of load application:

$$C_2 \sin p(l-c) = C_4[\sin p(l-c) - \tan pl \cos p(l-c)]$$

$$C_2 p \cos p(l-c) = C_4 p[\cos p(l-c) + \tan pl \sin p(l-c)] + \frac{P}{S}$$

From which

$$C_2 = \frac{P \sin pc}{Sp \sin pl}$$

$$C_4 = -\frac{P \sin p(l-c)}{Sp \tan pl}$$

Substituting the integration constants into (c) gives the equation for fiber position as a result of compressive loading:

$$y = \frac{P \sin pc}{Sp \sin pl} \sin px - \frac{Pc}{Sl} x$$

The above equation can easily be modified to describe a fiber under tension by changing the sign of S. Doing so changes p^2 to $-p^2$ as well, making $p\sqrt{-1} = pi$. Therefore, by substituting $-S$ and pi in place of S and p in the formulas obtained earlier, the formula for a beam under tension may be obtained. Recalling that:

$$\sin pi = i \sinh p, \qquad \cos pi = \cosh p, \qquad \tan pi = \tanh p$$

The left-hand side of the tie rod can be solved for:

$$y = -\frac{P \sinh pc}{Sp \sinh pl} \sinh px + \frac{Pc}{Sl} x$$

And the right-hand side:

$$y = -\frac{P \sinh p(l-c)}{Sp \sinh pl} \sinh p(l-x) + \frac{P(l-c)}{Sl} (l-x)$$

Having defined the equation for a single point load, the two point load formula (as used to calculate forces on nanonets) may be obtained by superimposing a second load. Furthermore, we substitute λ in for p to disambiguate from the applied load P:

$$\delta_a = -\frac{P_a sinh[\lambda(L-a)]}{S\lambda sinh[\lambda L]} sinh[\lambda L] + \frac{P_a(L-a)}{SL} a - \frac{P_b sinh[\lambda(L-b)]}{S\lambda sinh[\lambda L]} sinh[\lambda a] + \frac{P_b(L-b)}{SL} a$$

$$\delta_b = -\frac{P_a sinh[\lambda a]}{S\lambda sinh[\lambda L]} sinh[\lambda(L-b)] + \frac{P_a(L-b)}{SL} a - \frac{P_b sinh[\lambda(L-b)]}{S\lambda sinh[\lambda L]} sinh[\lambda b] + \frac{P_b(L-b)}{SL} b$$

8.2 Determination of Fiber Tension/Stress

Tension that exists in the fibers as a result of the STEP manufacturing process plays a dominant role in fiber stiffness. Following a procedure outlined by Cuenot et al., fiber residual stress (tension) and elastic modulus were simultaneously measured (experimental and intellectual credit: Ji Wang).[199] Fibers were spun over TEM grids, resulting in span lengths of about 60 µm, and then AFM was used as before to quantify apparent fiber stiffness, k_{app}, which consists of both a bending term k_b and a tensional term k_T as follows:

$$k_{app} = k_b + k_T = \frac{192EI}{L^3} + \frac{24T}{5L}$$

Assuming that the tensional term consists of a uniformly distributed stress σ_R throughout the fiber:

$$T = \sigma_R \frac{\pi}{4} d^2$$

Substituting and rearranging:

$$k_{app} = \frac{192EI}{L^3} + \frac{6\pi\sigma_R d^2}{5L}$$

$$\frac{k_{app}L}{d^2} = 3\pi E\left(\frac{d}{L}\right)^2 + \frac{6\pi\sigma_R}{5}$$

A linear plot of $\frac{k_{app}L}{d^2}$ as a function of $\left(\frac{d}{L}\right)^2$ will therefore yield a line with a slope from which the elastic modulus and an intercept from which residual stress may be extracted. By testing an array of fiber diameters from 100-700 nm, a common residual stress of 4.1 MPa was calculated.

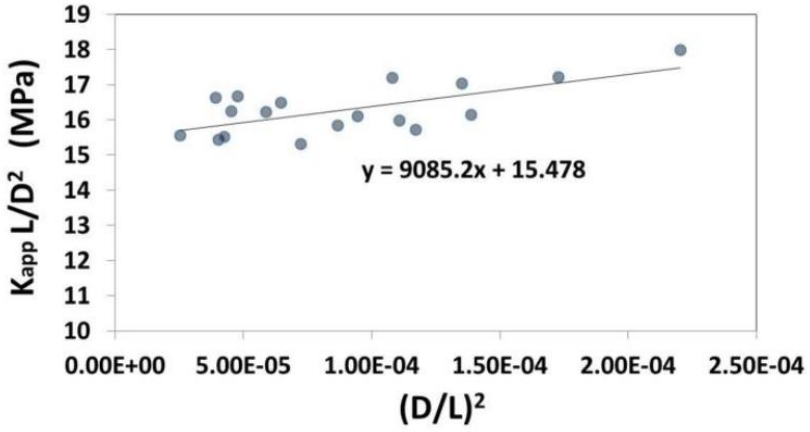

8.3 MATLAB Codes

8.3.1 Matlab Code for SLS Viscoelasticity Model

```
% Solved equation for relaxation test of SLS model
% Created 4/2/2013 by Kevin Sheets
% ---------------------------------
clc;
% Run probeforece.m with raw data first
% Plot Experimental Data
F = F;
F = F./max(F); F = F(2:10);
tF = t;
tF = tF - tF(2); tF = tF(2:10)';
duration = tF(end)-tF(1);
plot(tF,F,'ro')

% Initial Conditions:
s0 = 1;
```

```
t = 0:0.01:duration; %time, seconds

% Fit and Plot Model to Experimental Data
fitfunc = @(x,t)(s0/(x(1)+x(2)))*(x(2)+(x(1)*exp((x(1).*t)./x(3))));
x0 = [.2 1 .4];

[x, resnorm,~,exitflag,output] = lsqcurvefit(fitfunc,x0,tF,F);
hold on
plot(t,fitfunc(x,t))
xlabel('Time, s')
ylabel('Normalized Stress')
hold off

% Output Normalized Data
k1 = x(1)/(max(x))
k2 = x(2)/(max(x))
u = x(3)/(max(x))
```

8.3.2 Matlab Code for AFM Raw Data Conversion to Stiffness Values

```
% AFM Raw Data Converter
% Created 1/30/2012 by Kevin Sheets
%----------------------------------
% Converts raw AFM data output to stiffness value using data
straight from
% the BIOAFM output. First click File->import data and select
the AFM .txt file
% *Need to include cantilever stiffness value in this code*
%----------------------------------
clc;
% *First click File -> Import Data and select appropriate file*
probetip = 0.3459; %[N/m stiffness of AFM probe tip]

% Make data in table usable
um = data(:,1);
nm = data(:,2);
%um = data([300:310],1);
%nm = data([300:310],2);
x = length(um);

% Create Z, Cantilever Deflection, Fiber Deflection, and Force
values
Z = um*1000;
cantilever = nm-min(nm);
fiber = Z-cantilever;
force = cantilever.*probetip;
```

```
% Plot fiber deflection - force curve
plot(fiber,force)
xlabel('Fiber Deflection, [nm]')
ylabel('Force, [nN]')
hold on

% Slope of this curve is fiber stiffness in [N/m]
fiberstiffness = polyfit(fiber,force,1);
y = fiberstiffness(1)*fiber+fiberstiffness(2);
plot(fiber,y,'g--')
fiberstiff = fiberstiffness(1);
mnmstiff = fiberstiff*1000;

%Output Fiber Stiffness
fprintf('Fiber Stiffness: %2.5f N/m \n  %22.2f nN/um
\n\n',fiberstiff,mnmstiff)
```

8.3.3 Matlab Code for Probe Pull Force Calculations: ProbeForce.m

```
%ProbeForce.m
%Calculates force of adhesion given probe pulling data in xls
format
%Created by Kevin Sheets 1/17/2013
%Modified 3/28/2013 KS, Optimized 6/28/2013 KS
%Updated to include residual stress tension model 2/26/2014 KS
%Changed to 2-point load model (Ji) on 7/14/20214 KS
%-----------------------------------------------------------------
------
clear all; clc;
global I p ca cb x xa xb S c A B Ap Bp final11 final12 final13
final14 final21 final22 final23 final24 sinh1top ll11 sinh1bot
lla11 lambda la11 P1 P2 k1 k2 b defl1 defl2 d L t a cell_length
load_width fac_length cell_width kbend F...
    Fad deflpercent cell_strain fgraph sgraph lengthgraph
sheetname centeredness...
    stressstraingraph kloc kmax maxforce thickness
cell_elongation volume stress truestress toughness k1 k2 n v t1
t0 maxstress yout tout kleading ktrailing maxstrain cycle_period
T; %#ok<NUSED>

% Input Data
sheetname = 'IO10-N-4';
importdata_dist(sheetname);
```

```
% Select Parameters
forcecalculator_dist;
truestress = 1; % 0 = engineering, 1 = true;

% Print Results (1 = on, 0 = off)
fgraph = 0;
sgraph = 0;
lengthgraph = 0;
stressstraingraph = 0;
printresults_dist(fgraph, sgraph, lengthgraph,
stressstraingraph);

%elasticity_KPa = ((stress(2)-stress(1))/(cell_strain(2)-
cell_strain(1)))/1000;
%centeredness;
```

DEPENDENT FUNCTION FILE 1 of 3: IMPORTDATA_DIST.M

```
function [d, L, t, a, defl cell_length load_width fac_length
cell_width cell_elongation centeredness] = importdata(sheetname)
%IMPORTDATA imports excel file information to make usable in
probeforce.m
  global d L t a b defl1 defl2 cell_length load_width fac_length
cell_width deflpercent cell_strain thickness cell_elongation
centeredness;
  %data = xlsread('C:\Users\sheetsk\SkyDrive\Documents\Lab
Work\Probe Pull Data - Aneurism',sheetname);
  data = xlsread('C:\Users\sheetsk\Documents\Research\Lab Work
and Experiments\Probe Pull Data - Aneurysm
Dist.xlsx',sheetname);

  % Assign fiber constants (from spreadsheet)
  d = data(7,1).*10^-3; %fiber dia
  L = data(4,1); %original fiber length

  % Assign time-dependent variables (from spreadsheet)
  t = data(:,3); %time
  a = data(:,4); %location of applied force
  defl1 = data(:,5); %deflection
  b = data(:,6);
  defl2 = data(:,7);
  cell_length = data(:,8); %length of the cell from fiber to
probe
  load_width = data(:,9); %outermost width of cell attached to
fiber
```

```
  if size(data,2) == 10
    cell_width = data(:,10); %total fac length presence along
the load width
    fac_length = load_width/2; %total fac length presence along
the load width
  elseif size(data,2) == 9
    cell_width = data(:,11); %total fac length presence along
the load width
    fac_length = data(:,10); %total fac length presence along
the load width
  end

  % Truncate all accidentally-imported 'NaN' entries (blank
excel spaces)
  nan_test = isnan(defl1);
  if any(nan_test) == 1;
    nan_location = (min(find(nan_test)))-1;
    t = t(1:nan_location);
    a = a(1:nan_location);
    defl1 = defl1(1:nan_location);
    defl2 = defl2(1:nan_location);
    b = b(1:nan_location);
    cell_length = cell_length(1:nan_location);
    load_width = load_width(1:nan_location);
    cell_width = cell_width(1:nan_location);
    fac_length = fac_length(1:nan_location);
  end

  % Make basic calculations using this data
  deflhi1 = ((max(defl1))/L)*100;
  deflhi2 = ((max(defl2))/L)*100;
  deflpercent = max(deflhi1,deflhi2);
  cell_strain = ((cell_length - cell_length(1))/cell_length(1));
  cell_elongation = cell_length(end)-cell_length(1);
  centeredness = (((a(end)+b(end))/2)/L)*100;
end
```

DEPENDENT FUNCTION FILE 2 of 3: FORCECALCULATOR_DIST.M

```
function [kbend F Fad] = forcecalculator_dist()
%FORCECALCULATOR takes given condition and calculates beam force
  global sigma E I A B Ap Bp final12 final13 final14 final21
final22 final23 final24 d L t a b mn defl1 defl2 fac_length S
kbend F Fad T lambda k1 k2 P1 P2 lambda sinh1top final11 la11
ll11 sinh1bot lla11;
```

```
  % Material Inputs
  sigma = 4.108;
  S =(pi*(d/2)^2)*sigma; % Pretension, N
  E = 0.97; %Fiber Material Elastic Modulus [GPa]
  I = (pi*(d)^4)/64; %Moment of Inertia [nm^4]
  mn = (S/(10*E*I));
  mnrt = sqrt(mn);
  lambda = mnrt*100000;

%Compute Forces
  for i=1:length(t)
  %Equation 1 Term 1
  la11(i) = lambda.*a(i)./1000000;
  lla11(i) = lambda.*(L-a(i))./1000000;
  ll11 = lambda*L/1000000;
  sinh1bot(i) = sinh(la11(i)).*sinh(lla11(i))./sinh(ll11);
  sinh1top = 1/(S*lambda/1000000);
  final11(i) = -sinh1top.*sinh1bot(i);

  %Equation 1 Term 2
  laal(i) = ((L-a(i)).*(a(i)./L))./1000000;
  final12(i) = laal(i)./(S/1000000);

  %Equation 1 Term 3
  llb13(i) = lambda*(L-b(i))./1000000;
  sinh3bot(i) = sinh(llb13(i)).*sinh(la11(i))./sinh(ll11);
  sinh3top = 1/(S*lambda/1000000);
  final13(i) = -sinh3top.*sinh3bot(i);

  %Equation 1 Term 4
  lbal(i) = ((L-b(i)).*(a(i)./L))./1000000;
  final14(i) = lbal(i)./(S/1000000);

  %Equation 2 Term 1
  llb21(i) = lambda*(L-b(i))./1000000;
  sinh21bot(i) = sinh(llb21(i)).*sinh(la11(i))./sinh(ll11);
  final21(i) = final13(i);

  %Equation 2 Term 2
  final22(i) = final14(i);

  %Equation 2 Term 3
  lb23(i) = lambda.*b(i)./1000000;
  llb23(i) = lambda.*(L-b(i))./1000000;
  sinh23top(i) = sinh(llb23(i)).*sinh(lb23(i))./sinh(ll11);
  sinh23bot = 1/(S*lambda/1000000);
  final23(i) = -sinh23top(i).*sinh23bot;
```

```
  %Equation 2 Term 4
  lbbl(i) = ((L-b(i))*(b(i)/L))/1000000;
  final24(i) = lbbl(i)/(S/1000000);

  %Rearranging and Solving
  A(i) = final11(i)+final12(i);
  B(i) = final13(i)+final14(i);
  Ap(i) = final21(i)+final22(i);
  Bp(i) = final23(i)+final24(i);

  %P1
  ABAB(i) = A(i).*Bp(i)-Ap(i).*B(i);
  Y1Bp(i) = defl1(i).*Bp(i);
  Y2B(i) = defl2(i).*B(i);
  P1(i) = ((Y1Bp(i)-Y2B(i))./ABAB(i)).*1000;
  k1(i) = P1(i)./defl1(i);

  %P2
  BABA(i) = B(i).*Ap(i)-Bp(i).*A(i);
  Y1Ap(i) = defl1(i).*Ap(i);
  Y2A(i) = defl2(i).*A(i);
  P2(i) = ((Y1Ap(i)-Y2A(i))./BABA(i)).*1000;
  k2(i) = P2(i)./defl2(i);
  F(i) = P1(i)+P2(i);
  end
end
```

DEPENDENT FUNCTION FILE 3 of 3: PRINTRESULTS_DIST.M

```
function [kmax, kloc] = printresults(fgraph, sgraph,
lengthgraph, stressstraingraph)
%PRINTRESULTS prints results of the calculation to probeforce.m
  global x p ca cb xa xb c d E sigma I L S k1 k2 defl1 defl2 a b
P1 P2 T t F Fad kbend deflpercent cell_length kmax thickness
cell_strain cell_width cell_elongation sheetname centeredness
volume stress truestress;

  volume = 2.250*10^3; %cubic microns,
http://bionumbers.hms.harvard.edu/bionumber.aspx?&id=100434&ver=
15&trm=human cell volume
  thickness = volume./(cell_length.*cell_width); %um
  stress = (F'./(thickness.*cell_width(end)))*10^3; %Pa
  if truestress == 1;
    stress = (F'./(thickness.*cell_width))*10^3; %Pa
  end
```

```
  % Print Table Header
  fprintf('Force Generation and Fiber Stiffness Values: %s
\n\n',sheetname)
  fprintf(' P1[nN]  k1[mN/m] P2[nN]  k2[mN/m] F[nN]  \n')
  fprintf('-------------------------------------------------\n')

  % Print Table Result Lines
  for i=1:length(t)
  fprintf(' %5.2f   %5.2f  %5.2f  %5.2f | %6.2f
\n',P1(i),k1(i),P2(i),k2(i),F(i))
  end

  % Make Graph(s)
  if fgraph == 1;
    figure(1);
    subplot(2,2,1);
    plot(t,F,'ro-')
    xlabel('Time [s]')
    ylabel('Force [nN]')
    hold on
    for j=2:length(t)
     % if F(j-1)>F(j) && F(j-1)>F(j-2)
     %   text(t(j-1),F(j-1)+(max(F)*.06),['x'])
      % end
    end
    hold off
  end

  if sgraph == 1;
    figure(1);
    subplot(2,2,2);
    plot(t,stress,'ko-')
    xlabel('Time [s]')
    ylabel('Stress [Pa]')
  end

  if lengthgraph == 1;
    figure(1);
    subplot(2,2,3);
    plot(t,cell_length,'bo-')
    xlabel('Time [s]')
    ylabel('Cell Length [um]')
  end

  if stressstraingraph == 1;
    figure(1);
```

```
    subplot(2,2,4);
    plot(cell_strain,stress,'go-')
    xlabel('Strain')
    ylabel('Stress (Pa)')
  end
  T = T*10^6;
  toughness = 0; %trapz(cell_strain,stress); %J/m^2 = N/m
  maxP1 = max(P1);
  maxP2 = max(P2);
  [Fmax,Fmaxloc] = max(F);

  cellstrain = (cell_length(end)-cell_length(1))/cell_length(1);
  if cellstrain == -1;
    cellstrain = (cell_length(end-1)-
cell_length(1))/cell_length(1);
  end

  %Calculate Stiffness:
  area = (pi/4)*((d*10^-6)^2);
  Inew = (1/64)*pi*(d*10^-6)^4;
  Enew = 0.97;
  S = S*10^-6;
  p = ((S/(Inew*E*10^9))^.5);
  c = ((a(Fmaxloc)+b(Fmaxloc))/2)*10^-6;
  ca = a(Fmaxloc)*10^-6;
  cb = b(Fmaxloc)*10^-6;
  x = (L*10^-6)-c;
  xa = (L*10^-6)-ca;
  xb = (L*10^-6)-cb;

  kint1 = (-sinh(p*c)*sinh(p*x))/(S*p*sinh(p*L));
  kint2 = (c*x)/(S*L);
  kint = 1/(kint1+kint2)/1000;

  ka1 = (-sinh(p*ca)*sinh(p*xa))/(S*p*sinh(p*L));
  ka2 = (ca*xa)/(S*L);
  ka = 1/(ka1+ka2)/1000;

  kb1 = (-sinh(p*cb)*sinh(p*xb))/(S*p*sinh(p*L));
  kb2 = (cb*xb)/(S*L);
  kb = 1/(kb1+kb2)/1000;

  fprintf('\n Fmax   k    ka   kb   %%Defl  Strain  Elong  \n')
  fprintf('-----------------------------------------------------
--\n')
  fprintf(' %5.2f  %5.2f  %5.2f  %5.2f  %5.2f  %5.2f  %5.2f
%.2f \n',Fmax,kint,ka,kb,deflpercent,cellstrain,cell_elongation)
```

```
  fprintf('\n\n')

  fprintf('Start Height: %.2f \n', cell_length(1))
  fprintf(' End Height: %.2f \n', cell_length(end))
end
```

OPTIONAL DEPENDENT FILE: SPRINGDASH.SLX

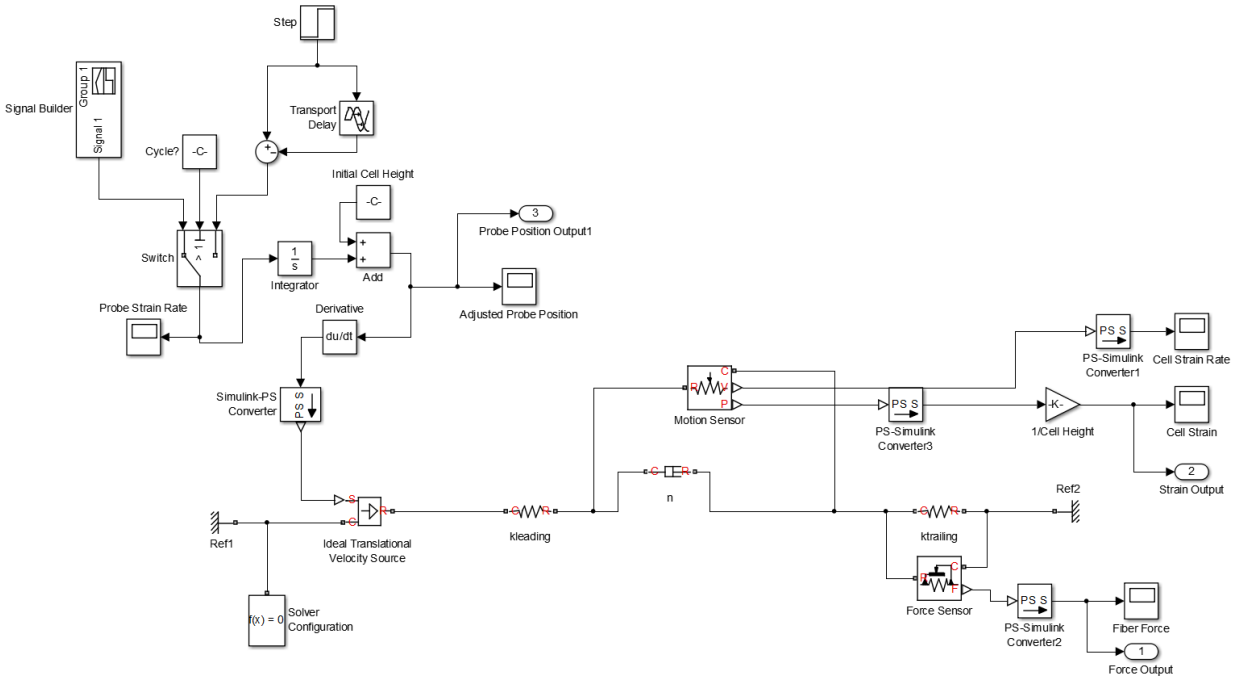

The above Simulink model uses physical elements (springs and dashpots) to simulate the viscoelastic response of the cell body to an external perturbation.